

### **3. DYNAMIC LOAD ANALYSIS FOR NEW FUEL RACKS IN THE BUFFER POOL**

#### **3.1 INTRODUCTION**

##### ***3.1.1 Purpose***

The purpose of this section is to present the structural analysis of New Fuel Storage Racks (FSR) for the Buffer Pool located in the Reactor Building (RB) of the ESBWR.

The FSR are structures fabricated from stainless steel plates, forming 7x2 cells to house the new fuel assemblies. Each two FSR are joined and installed together forming a 14x2 cell assembly (ID 6). Therefore the calculation presented in this report is based on a 14x2 configuration. The FSR are anchored to the floor of the Buffer Pool at elevation 27000.

##### ***3.1.2 Scope***

The scope of this analysis covers the design principles, load analysis and justification of the structural configuration of the FSR.

The boundaries of the analysis include all the sections of the structure, including plate and weld stress evaluations. Maximum displacements at the top of the FSR are checked. Reactions at the bottom of FSR are obtained to validate the anchor bolt section.

The maximum lateral forces between the fuel assemblies and the top of the FSR cell, along with the maximum vertical forces between fuel assemblies and the FSR base plate are determined.

The calculation of the embedment for the anchor bolts is not within the scope of this document analysis. The structural evaluation of the new fuel assemblies enclosed in the FSR is not covered in this analysis, but their masses have been taken into account. The structural evaluation of the FSR against accidental equipment drop, the fatigue analysis, and the functionality of the mechanical components are not within the scope of this analysis.

3.2 INPUT DATA

**Table 3-1**  
**List of Document Input Data (ID)**

No.	Source Document			Requirement/Data	Status
	No.	Issue	Title		
1	5926.D500	01	New Fuel Rack Assembly Drawing	Geometry. Materials.	V
2	5926.D510	01	New Fuel Rack Base Plate	Geometry	V
3	5926.D520	01	New Fuel Rack Miscellaneous Detail	Geometry	V
4	26A7032	3	Fuel Storage Rack Design Specification	Design Codes. Design Requirements. Fuel assembly weight. Fuel handling loads. Applicable Response Spectra . Loading Combinations. Spent Fuel Pool Water Temperatures	V
5	26A6558	4	General Civil Design Criteria	Stress free temperature	V
6	5926.D110	01	Rack Layout at Reactor Building	Rack layout. Distance between racks and distance to the walls.	V
7	105E3908	03	General Arrangement, ESBWR Nuclear Island	Plant axes	V
8	55926ATN04	00	ESBWR Reactor Pool Bottom (elevation +27m) Synthesized SSE Acceleration Time Histories	SSE acceleration time histories	V <sup>+</sup>

### 3.3 SUMMARY OF RESULTS

Table 3-2 summarizes the most critical results obtained from the analysis of the FSR and the comparison with the allowable values in accordance with the design code (Reference 3).

**Table 3-2**  
**FSR Main Analysis Results**

Steel Plates	Calculated Stress (MPa)	Stress Limit (MPa)	Ratio
8 mm thick channel plate	267	292.8	0.91
Channel to support-base welds	182	198.6	0.92
12 mm thick door plates	123	195.2	0.63
Assembly grid plate	52.5	195.2	0.27
Axis and hinge	130	195.2	0.67
15 mm thick support-base stiffeners	138	195.2	0.71
15 mm thick folded base plate	266	292.8	0.91
30 mm thick bolted support plates	124	292.8	0.42
M24x2 anchor bolts	0.91 (*)	1 (*)	0.91

(\*) This is a stress ratio, not a stress value (see Sections 3.4.9 and 3.5.3).

### 3.4 ANALYSIS SUMMARY

Section 3.4.1 presents a brief description of the FSR.

Section 3.4.2 presents the properties of the FSR materials.

Section 3.4.3 indicates the applicable design code for analysis of the FSR.

Section 3.4.4 presents the assumptions used in the analysis of the FSR.

Section 3.4.5 gives a detailed description of the FSR model. A detail Finite Element Model (FEM) is developed for the FSR in order to analyze stresses, reactions and displacements.

Section 3.4.6 describes the different load cases which apply to the FSR analysis.

Section 3.4.7 presents the load combinations applied for the FSR analysis.

Section 3.4.8 presents the analysis procedure description for the FSR.

Section 3.4.9 gives the allowable stress limits used in the FSR analysis.

### **3.4.1 New Fuel Storage Rack Description**

The FSR support and protect stored new fuel assemblies. The FSR are structures made of stainless steel plates, forming a 14x2 array of storage cells. The FSR are located in the Buffer Pool within the Reactor Building and are anchored to the pool floor at elevation 27000.

A detailed description of FSR is shown in the assembly and detail drawings of the FSR (ID 1, 2, 3 and 6). As described in ID 6 each pair of 7x2 FSR are laterally joined forming a 14x2 FSR. The rest of the document describes and analyzes the behavior of the 14x2 FSR.

The rack is formed by the assembly of a matrix of cells. The typical cell is a U-section of plain SS 8 mm thick (see ID 3, section "D-D").

The assembly of individual cells to conform a stiff structure is accomplished by the joining the grids to the base plate. The grids are formed from plain SS plates jointed by slot insertion that later, are welded to increase the strength (see the typical 6 mm x 50-100 vertical corner weld in ID 1, view "A"). The individual cells are then welded to the grids (see ID 1).

Each channel is welded to the support-base plate, which is stiffened underneath with plates. The base plate is anchored to the pool with sixteen (16) M24x2 anchor bolts embedded in the pool floor.

The main dimensions of the FSR are 3672x650 mm and 3697 mm in height. Different thicknesses of plates are used in the FSR: 8 mm for the main plates that form each channel, 12 mm for the two (2) plates per channel that form the doors, 10 mm for the plates of the two (2) grid assemblies that stiffen the channels at two different elevations, and 15 mm for the support-base plate that supports the 28 channels, including the stiffener plates.

Each channel has two doors that remain open at the lateral entrance for the fuel assembly. When the fuel assembly is positioned within the channel and rests on the support-base plate hole, the doors close remain blocked. The axis is a cylinder of 48 mm outside diameter and 33 mm inside diameter. The axis is guided by three hinges and a hole located in the support plate. Each hinge is a cylinder of 70 mm outside diameter and 50 mm inside diameter welded to the corresponding channel.

### **3.4.2 Materials**

The FSR are manufactured using stainless steel SA-240 Type 304L. Material SA-564 Type 630 H1075 is used for anchor bolts.

The mechanical properties of type 304L stainless steel are greater than those of type 304, so the mechanical properties of the latter are used.

Table 3-3 shows the material properties in accordance with Section II, Part D of the ASME Code (Reference 2). Material properties at 121.1°C (250°F) are assumed based on ID 4.

**Table 3-3**  
**Material Properties at 250°F (121.1°C)**

<b>Material</b>	<b>E</b> (MPa)	<b>ρ</b> (kg/m <sup>3</sup> )	<b>α</b> (1/°C)	<b>S<sub>y</sub></b> (MPa)	<b>S<sub>u</sub></b> (MPa)	<b>S</b> (MPa)
SA-240 Type 304L (*)	1.90·10 <sup>5</sup>	7850	16.4·10 <sup>-6</sup>	162.7	472.9	134.1
SA-564 Type 630 H1075	1.91·10 <sup>5</sup>	7850	11.3·10 <sup>-6</sup>	797.0	999.7	285.4

(\*) Properties shown are those corresponding to type 304 stainless steel

- ρ ≡ Density (Reference 1)
- E ≡ Modulus of elasticity (Reference 2, Table TM-1)
- α ≡ Coefficient of thermal expansion (Reference 2, Table TE-1)
- S<sub>y</sub> ≡ Yield strength (Reference 2, Table Y-1)
- S<sub>u</sub> ≡ Ultimate strength (Reference 2, Table U)
- S ≡ Maximum – allowable Stress (Reference 2, Table 1A)

### 3.4.3 Design Code

Stresses in the structural components of the FSR shall not exceed the allowable stress levels given in the ASME B&PV Code, Section III, Division I, Subsection NF (Reference 3).

### 3.4.4 Assumptions

The calculation procedure used for the analysis has been performed based on the following assumptions of FSR behavior:

- It is assumed that the material of the structure (stainless steel) has a linear elastic behavior within the field of the small displacement/deformations.
- An assumption of FSRs with a 100% fuel load shall be considered. Since the FSRs are anchored to the pool floor and the fuel elements have a large mass but do not provide any stiffness to the assembly, it is reasonable to expect that this case will present the maximum deformations and stresses.
- For the fuel assembly the dry weight is assumed to be 540 lbs (245 kg) and the net immersed weight to be 474 lbs (215 kg) (ID 4).
- The fuel assembly shall be conservatively rigid enough that it is only supported on the top part of the upper doors, in addition to the support-base plate.

- The water mass acting in the vertical direction is not considered because the water could flow inside each one of the cells in the vertical direction.
- Prior experience in the study of the dynamic behavior of the freestanding FSRs shows a significant reduction in the lateral displacements of the FSR when the hydrodynamic coupling between the FSRs and between the FSRs and the walls through the water around them is considered. It is reasonable to assume that the coupling effect shall be lower for FSRs anchored to the bottom of the pool, as in the case under study. Therefore, in order to simplify the calculations, a conservative assumption has been made to disregard the positive effect of the hydrodynamic coupling towards the FSR design. Another conservative assumption shall take into account the added mass to be included in the models, without considering neighboring FSRs or walls.

### **3.4.5 FSR Analysis Model**

A finite element model (FEM) for the analysis of the FSR is built with ANSYS 10.0 (Reference 7). A description of the FEM (see Figures E1 and E2 in Appendix E) follows:

- The channel plates of the FSR (see Figure E3) are modeled with an 8 mm thick stainless steel plate (Reference 7, SHELL 63 ANSYS elements). These channel plates are welded in their entire bottom end to the support plate and are connected by the grid assemblies at two elevations.
- The channel plates in contact with the grid assembly plates (see Figure E4) are modeled with (8+10) mm thick stainless steel plate (Reference 7, SHELL 63 ANSYS elements). The grid assembly plates not in contact with the channels are modeled with 10 mm stainless steel plates (Reference 7, SHELL 63 ANSYS elements).
- The door plates (see Figure E5) are modeled with 12 mm thick stainless steel plates (Reference 7, SHELL 63 ANSYS elements). These plates are welded to the rotation axis, which is modeled with 7.5 mm thick stainless steel plates (Reference 7, SHELL 63 ANSYS elements). The hinges are modeled with 10 mm thick stainless steel plates (Reference 7, SHELL 63 ANSYS elements). The connections between the axis and the hinges and between the axis and the support-base plate are represented by coupling in the radial direction between nodes of the two connected plates. The nodes located at the bottom elevation of the middle hinge are also coupled in the tangential direction to represent the lock-out device. The bottom end axis nodes are also coupled in vertical direction with the corresponding nodes on the support-base plate.
- The support-base plate (see Figure E6) of the FSR is modeled with stainless steel plates (Reference 7, SHELL 63 ANSYS elements). This support includes the 15 mm thick folded plate with 98 mm diameter holes for each one of the 28 channels and with 68 mm diameter holes for each one of the 28 axes, the 15 mm thick rectangular stiffeners welded under the folded plate, the 15 mm thick triangular stiffeners welded on the folded plate near the bolt holes, and the (15+15) mm thick reinforced anchor plates. The 30 mm diameter hole centered in the plate is not modeled. Due to this fact and in order to achieve a more realistic boundary condition, as well as fixing the three displacements at the central point, the two horizontal rotations are also fixed.

- 50% of the fuel mass ( $245 \times 28 \times 0.5 = 3430$  kg) acting in the horizontal X direction is distributed in the central top node of the upper doors. The same 3430 kg acting in the horizontal Y direction is distributed in the channels upper end, and the other 50% (3430 kg) is distributed in the nodes of the model located in the support-base plate holes in both horizontal directions. 100% of the mass (6860 kg) shall apply vertically in the nodes of the model located in the support-base plate. These fuel assembly masses are included as lumped masses (Reference 7, MASS 21 ANSYS elements) in the model.
- The internal water mass acting in the two horizontal directions is distributed in the inner nodes of the model. The node mass distribution is proportional to the volume associated with each inner node. The internal water mass is obtained from the total FSR internal volume where the fuel volume and metal volume is subtracted. Metal mass is ANSYS calculated. Each fuel assembly has a volume of  $0.03 \text{ m}^3$ . The internal water masses are included as lumped masses (MASS 21 ANSYS (Reference 7) elements) in the model.
- The external water added mass has been obtained from Reference 6, where the added mass of a rigid rectangular plate is calculated using the equation  $m_w = (\pi \cdot a^2 \cdot b \cdot \rho) / 4$  (where (a) and (b) are the short and long lengths, respectively, of the FSR channel plate, and ( $\rho$ ) is the water density). The added mass of the FSR is approximately 2420 kg. This added mass corresponds to the following assumptions: (a) infinitely stiff plate, (b) moving as a stiff solid body (c) in an infinite mass of water. The FSR (a) is elastically deformable, (b) is anchored to the ground, i.e. it moves like a cantilever and (c) has a finite layer of water around it, so the motion of each FSR shall be coupled through water to the motion of neighboring FSRs. Therefore, the actual added mass and the actual horizontal displacements of the top part of the FSR shall be lower than those obtained in the analysis. Introducing 2420 kg of added mass is a conservative estimate but it is verified that this added mass does not significantly impact in the final results of the FSR analysis (stresses and bolt reactions). The external water added masses are included in the model multiplying the internal water masses by a factor.
- The mass of the SS plates is accounted for by means of its density.
- The coordinate system adopted in the FEM is the right hand Cartesian coordinate system. The X-direction represents the North-South direction, the Y-direction represents the East-West direction, and the Z-direction is vertical (ID 7).
- The units used in the FSR FEM are kilograms for mass, meters for length, and seconds for time.

The FSR mass considered in the analysis model is presented in Table 3-4:

**Table 3-4  
Mass Breakdown**

<b>Component</b>	<b>Horizontal mass (kg)</b>	<b>Vertical mass (kg)</b>
Stainless Steel	5863	5863
Fuel Assemblies (28 elements)	6860	6860
Internal Water	4110	-
External Added Water	2420	-
<b>Total Mass</b>	<b>19253</b>	<b>12723</b>

### 3.4.6 Analysis Loads

The following loads are considered in the analysis of the FSR:

D	Dead Weight + Buoyancy
P <sub>f</sub>	Upward force by postulated stuck fuel assembly
T <sub>o</sub>	Differential temperature induced loads (normal or upset conditions)
T <sub>a</sub>	Differential temperature induced loads (abnormal design condition)
SSE	Safe Shutdown Earthquake
SRVD	Safety Relief Valve Discharge
LOCA	Loss of Coolant Accident
L <sub>R</sub>	Lifting FSR during installation

#### 3.4.6.1 Dead Weight + Buoyancy (D)

In addition to the dead weight of the FSR and fuel assemblies, it is necessary to consider the buoyancy, that is, the thrust that the water applies on the FSR and the immersed fuel. This effect is taken into account in the analysis by reducing the gravity acceleration by a reducing factor calculated as follows:

FSR steel mass:	$M_s = 5830 \text{ kg}$ (see Table 3-4)
Steel volume:	$V_s = M_s / \rho = 5830/7850 = 0.743 \text{ m}^3$
Fuel assemblies mass:	$M_f = 245*28 = 6860 \text{ kg}$
Fuel assemblies volume:	$V_f = 0.03*28 = 0.84 \text{ m}^3$
Total mass:	$M_T = 5830+6860 = 12690 \text{ kg}$

Total volume:  $V_T = 0.743 + 0.84 = 1.583 \text{ m}^3$

That means 1583 kg of water mass moved. Then, the reducing factor is:

$$F = (12690 - 1583) / 12690 = 0.876$$

And the reduced gravity acceleration is obtained from

$$g' = 0.876 \cdot g = 8.6 \text{ m/s}^2$$

#### 3.4.6.2 Fuel Handling Loads ( $P_f$ )

The FSR shall be designed to withstand a pull-up force of 17.79 kN, which is necessary in the event of a fuel assembly or grappling device hanging up during removal and a horizontal force of 4.45 kN being applied at the top of the FSR (ID 4).

#### 3.4.6.3 Differential Temperature Induced Loads ( $T_o$ , $T_a$ )

The maximum Buffer Pool water temperatures are 48.9°C (120°F) in normal conditions and 60°C (140°F) in abnormal conditions (ID 4).

The stress-free temperature is assumed to be 15.5°C (ID.5).

The only restrictions on the FSR are the sixteen anchor bolts to the pool floor.

The maximum distance between bolts is  $((2 \cdot (1506 + 165))^2 + (2 \cdot 295)^2)^{0.5} = 3394 \text{ mm}$  (ID 2).

The maximum expansion projected between these two most separated anchor points, conservatively assuming a maximum temperature of 121.1°C (250°F)(ID 4), is calculated to be:

$$\alpha \cdot L \cdot \Delta T = 16.4 \text{ E-6} \cdot 3394 \cdot (121.1 - 15.5) = 5.9 \text{ mm}$$

The M24 anchor bolts are placed in the 30 mm diameter hole located in the 15 mm thick folded plate of the FSR. Under these conditions the tolerance between the anchor bolt diameter and the diameter of hole is enough to absorb the maximum expansion estimated. Therefore, no thermal induced stresses are calculated in this analysis. The racks are submerged in water and can expand in both the vertical and horizontal directions without significant restrictions. The temperature gradient in the vertical direction is considered negligible for structural analysis.

#### 3.4.6.4 Safe Shutdown Earthquake (SSE)

The FSR shall be designed to withstand the SSE loads specified in ID 4 Appendix A30. A structural damping value of 4% for SSE conditions is used (Reference 12). Of the two applicable response spectra (nodes 108 and 208) for each direction, the enveloping one is chosen and conservatively applied. Figures E-7a, E-7b, and E-8 in Appendix A show the spectra applied in both horizontal and vertical directions.

3.4.6.5 Safety Relief Valve Discharge (SRVD)

The FSR shall be designed to withstand the SRVD loads specified in ID 4 Appendix A30. A structural damping value of 4% for SRVD conditions is used (Reference 12). Figures E-9 and E10 in Appendix E show the spectra applied in both horizontal and vertical directions.

3.4.6.6 Loss of Coolant Accident (LOCA)

The FSR shall be designed to withstand the LOCA loads specified in ID 4 Appendix A30. A structural damping value of 4% for LOCA conditions is used (Reference 12). Figures E-11 and E12 in Appendix E show the spectra applied in both horizontal and vertical directions in.

3.4.6.7 Lifting FSR During Installation ( $L_R$ )

The FSR is verified to withstand the lifting load during installation. The FSR is supported in the four upper holes of the tow grid upper plates (ID 1 and ID 2, item 53.001).

**3.4.7 Load Combinations**

The load combinations and acceptance criteria shall be per Appendix D of SRP 3.8.4. Table 3-5 shows the envelope load combinations that will be conservatively used for the design of the FSR, based on the aforementioned load combinations.

**Table 3-5  
Load Combinations**

<b>Level A:</b>	$D + P_f$
<b>Level D:</b>	$D + SSE + SRVD + LOCA + T_a$

$D + P_f$  is a Level B load combination, but it is conservatively assumed as a Level A load combination.

**3.4.8 Analysis Methodology Description**

Static and dynamic loads are considered in the analysis. The response spectrum analysis method is used to analyze the dynamic loads.

The static load case (D) is resolved by structural static analysis applying the reduced gravity acceleration  $g'$  (see Section 3.4.6.1).

The fuel handling load case ( $P_f$ ) is analyzed by applying the forces prescribed in Section 3.4.6.2 in a central channel (see Figure E-13).

The lifting load during installation case ( $L_R$ ) is analyzed by applying the gravity acceleration,  $g$ , and supporting the FSR in the appropriate four grid points.

The dynamic load cases are resolved by response spectrum analysis. Before the response spectrum analysis is performed, a modal analysis is performed to determine the natural frequencies and mode shapes of the FSR. The subspace method is used for mode extraction in modal analysis. One hundred fifty (150) eigenfrequencies are requested in the modal analysis.

Once the eigenfrequencies of the model have been determined with the modal analysis, a response spectra analysis for each dynamic event (SSE, SRVD and LOCA) is evaluated for each of the three directions, X, Y and Z.

The input response spectra are represented by no more than twenty (20) points (ANSYS limitation), beginning at a frequency lower than the lowest obtained in the FSR modal analysis.

Once the response spectrum analysis has been performed for each direction, the modal responses are combined in accordance with the grouping method established in Regulatory Guide 1.92 (Reference 5).

That the modes used for the modal combinations are not enough to reach the required 90% of the mass in each direction (see Section 3.5). Therefore the missing mass in each direction will be computed as the difference between the total mass of the model and the sum of the effective masses of the low frequency modes taken into account in the response spectrum analysis. In short, an additional static analysis is performed for each direction with the highest response spectrum acceleration corresponding to any frequency higher than the highest one considered in the modal combination (acceleration greater than ZPA, therefore conservative). Such acceleration will be applied to the fraction of mass not included in the modal combination. The total combined response to high-frequency modes is combined by the Square-Root-Sum-of-Squares (SRSS) method with the total combined response from lower-frequency modes to determine the overall responses.

Finally, as the load combination includes multiple dynamic loads, these loads are combined by the SRSS method.

### **3.4.9 Stress Limits**

The stress limits are taken from ASME Code (3), Subsection NF an Appendix F corresponding to the Design by Analysis for Class 3 Plate and Sheet Type Supports.

#### ***Base metal SA-240 Type 304L (with mechanical characteristics of SA-240 Type 304)***

Level A Conditions (NF-3251.1 and Table NF-3552(b)-1)

$$P_m \leq S = 134.1 \text{ MPa}$$

$$P_m + P_b \leq 1.5 \cdot S = 201.1 \text{ MPa}$$

$$\tau \leq 0.6 \cdot S = 80.4 \text{ MPa}$$

Level D Conditions (Appendix F.F-1332)

$$P_m \leq \text{Minimum of } 1.2 S_y \text{ or } 0.7 S_u = 195.2 \text{ MPa}$$

$$P_m + P_b \leq 1.5 \cdot P_m \text{ (limit)} = 292.8 \text{ MPa}$$

$$\tau \leq 0.42 \cdot S_u = 198.6 \text{ MPa}$$

### ***Bolting Material SA-564 Type 630 H1075***

Level A Conditions (NF-3324.6 for austenitic steel)

$$\text{Average normal stress} = f_t \leq F_{tb} = S_u/3.33 = 300.2 \text{ Mpa}$$

$$\text{Shear stress} = f_v \leq F_{vb} = 0.62 \cdot S_u/5 = 123.9 \text{ MPa}$$

$$\text{Combined tensile and shear stress: } f_t^2 / F_{tb}^2 + f_v^2 / F_{vb}^2 \leq 1$$

Level D Conditions (Appendix F.F-1335)

$$\text{Average normal stress} = f_t \leq F_{tb} = \text{Minimum of } S_y \text{ or } 0.7 S_u = 699.8 \text{ Mpa}$$

$$\text{Shear stress} = f_v \leq F_{vb} = \text{Minimum of } 0.42 \cdot S_u \text{ or } 0.6 S_y = 419.8 \text{ MPa}$$

$$\text{Combined tensile and shear stress: } f_t^2 / F_{tb}^2 + f_v^2 / F_{vb}^2 \leq 1$$

### ***Welds***

Level A Conditions (NF-3324.5 and Table NF-3324.5(a)-1)

#### **Fillet welds:**

$$\text{Shear Stress on effective throat} \leq 0.3 \cdot S_u^{(1)} = 165.4 \text{ MPa}$$

$$\text{Shear Stress on base metal} \leq 0.4 \cdot S_y = 65.1 \text{ MPa}$$

Tension or compression parallel to axis of weld  $\leq$  Same as base metal

<sup>(1)</sup> Base metal tensile strength range between 472.9 MPa and 551.5 MPa (68.6 and 80 ksi), minimum weld metal tensile strength, 551.5 MPa (80 ksi).

Level D Conditions (Appendix F.F-1332)

$$\text{Shear Stress} \leq 0.42 S_u = 198.6 \text{ MPa}$$

Tension or compression parallel to axis of weld  $\leq$  Same as base metal

## **3.5 RESULTS OF THE ANALYSIS**

The ANSYS output for static, modal and spectrum analyses, including the modal combination, is included in Appendix F.

Table 3-6 presents the main eigenfrequencies, obtained from the modal analysis, with the associated effective mass. Additionally, some lower frequency modes (modes 2 and 5) are included as examples of typical mode shapes that do not contribute to the solution response.

Figures E-14 through E-23 in Appendix E show the deformed shapes of these eigenmodes.

**Table 3-6**  
**Main Eigenfrequencies**

Mode	Frequency (Hz)	Effective Mass (kg)	Description	Figure in Appendix E
1	7.0	11034	Y Bending	E14
2	7.2	-	Z Torsion	E15
3	9.6	-	YZ plane Bending	E16
4	14.5	-	YZ plane double Bending	E17
5	16.8	12844	X Bending	E18
31	33.2	1164(X), 17(Y)	Bending Axes	E19
61	48.5	89(X), 71(Y)	Bending Axes	E20
63	51.0	624(X), 355(Y)	Bending Axes	E21
69	54.2	254(X), 66(Y)	Bending Axes	E22
71	54.4	182(X), 41(Y)	Bending Axes	E23

Table 3-7a indicates the amount of mass considered in the modal combination and the corresponding percentage with respect to the total mass.

**Table 3-7a**  
**Combined Effective Masses**

Event	X direction		Y direction		Z direction	
	Mass (kg)	(%)	Mass (kg)	(%)	Mass (kg)	(%)
SSE	13931 (72.3%)		14415 (74.8%)		6 (0%)	
LOCA	13260 (68.8%)		15546 (80.7%)		6 (0%)	
SRVD	13260 (68.8%)		14406 (74.8%)		6 (0%)	

Table 3-7b indicates the acceleration considered to account for the high-frequency modes, with the corresponding percentage of missing mass.

**Table 3-7b  
Acceleration for Missing Masses**

Event	X direction		Y direction		Z direction	
	Acceleration (g)	(%)	Acceleration (g)	(%)	Acceleration (g)	(%)
SSE	1.27	27.7	1.25	25.2	1.74	100
LOCA	0.05	31.2	0.029	19.3	0.225	100
SRVD	0.067	31.2	0.067	25.2	0.143	100

**3.5.1 Displacements Results**

The maximum horizontal displacement obtained at the top of the FSR for the most unfavorable load combination is 18.0 mm and occurs in the X-direction (see Figure A-24, in Appendix A).

One half of the expansion due to thermal expansion (Section 3.4.6.3) is applied to each rack in opposing horizontal directions. If the abnormal pool temperature were to occur simultaneously with a seismic event, the resulting total displacement is calculated as:

$$18.0 \text{ mm} + 5.9 \text{ mm}/2 = 21.0 \text{ mm}$$

The minimum distance between adjacent FSR at the top level or between FSR and pool wall is 100 mm (ID 6). Therefore, no contact occurs between adjacent FSR or between the FSR and the pool walls.

**3.5.2 Plate Stress results**

The stress results obtained for the different load combinations are checked in the most critical sections of the different plates of the FSR. Figures E-25 to E-28 in Appendix E show the results.

**3.5.2.1 8 mm Thick Channel Plate**

The maximum stresses obtained for the 8mm thick channel plate compared with the corresponding allowable stresses are given in Table 3-8, where:

- $S_Z$  ≡ Vertical direction (Z) membrane stress
- $S_H$  ≡ Horizontal direction (X or Y) membrane stress
- $S_{HZ}$  ≡ Shear membrane stresses on the plane of the plate.

- Bending stresses across the plate thickness are negligible and are classified as secondary stresses; however, other directions of the plate contain primary bending stresses that are included in the stress analysis results.

**Table 3-8**  
**8mm Thick Channel Plate Stress Results**

Stress Category	Calculated Stress (MPa)	Allowable Stress (MPa)
Level A Conditions Maximum Membrane Stresses	$S_z = 35.8$ (Figure E-25)	134.1
	$S_H = 6.7$	134.1
	$S_{HZ} = 3.9$	80.4
Level D Conditions Maximum Membrane Stresses	$S_z = 267$ (Figure E-26)	292.8
	$S_H = 57.4$	292.8
	$S_{HZ} = 41.5$	198.6

The maximum stresses obtained for the channel to support-base, compared with the corresponding allowable stresses are given in Table 3-9.

**Table 3-9**  
**Channel to Support-Base Weld Stress Results**

Stress Category	Calculated Stress (MPa)	Allowable Stress (MPa)
6 mm double fillet welds (end channels)	$(267) \times (8/12) = 178.0$	198.6
6 mm fillet welds (all channels)	$(137) \times (8/6) = 182.6$	198.6

### 3.5.2.2 12 mm Thick Door Plates

The maximum stress obtained for the 12 mm thick door plates compared with the corresponding allowable stresses are given in Table 3-10, where:

- $S_z \equiv$  Vertical direction (Z) membrane stress

- $S_H$  ≡ Horizontal direction (X or Y) membrane stress
- $S_{HZ}$  ≡ Shear membrane stresses on the plane of the plate.
- Bending stresses across the plate thickness are negligible and are classified as secondary stresses; however, other directions of the plate contain primary bending stresses that are included in the stress analysis results.

**Table 3-10**  
**12 mm Thick Door Plates Stress Results**

Stress Category	Calculated Stress (MPa)	Allowable Stress (MPa)
Level A Conditions Maximum Membrane Stresses	$S_Z = 0.1$	134.1
	$S_H = 0.08$	134.1
	$S_{HZ} = 0.2$	80.4
Level D Conditions Maximum Membrane Stresses	$S_Z = 40.3$	195.2
	$S_H = 123$ (Figure E-27)	195.2
	$S_{HZ} = 44.2$	198.6

### 3.5.2.3 10 mm and (10+8) mm Assembly Grid Plates

The maximum stress obtained for the assembly grid plates compared with the corresponding allowable stresses are given in Table 3-11, where:

- $S_Z$  ≡ Vertical direction (Z) membrane stress
- $S_H$  ≡ Horizontal direction (X or Y) membrane stress
- $S_{HZ}$  ≡ Shear membrane stresses on the plane of the plate.
- Bending stresses across the plate thickness are negligible and are classified as secondary stresses; however, other directions of the plate contain primary bending stresses that are included in the stress analysis results.

**Table 3-11**  
**10 mm and (10+8) mm Thickness Assembly Grid Stress Results**

Stress Category	Calculated Stress (MPa)	Allowable Stress (MPa)
Level A Conditions Maximum Membrane Stresses	$S_Z = 11$	134.1
	$S_H = 14$	134.1
	$S_{HZ} = 3$	80.4
Lifting Load	$S_{HZ} = 47$ (Figure E-29)	80.4
Level D Conditions Maximum Membrane Stresses	$S_Z = 37.4$	195.2
	$S_H = 52.5$ (Figure E-28)	195.2
	$S_{HZ} = 7$	198.6

Welds in these plates are judged to have enough margin in view of the low stress results in plates.

#### 3.5.2.4 Axis and Hinge Plates

The maximum stress obtained for the axis and hinges compared with the corresponding allowable stresses are given in Table 3-12, where:

- $S_Z$  ≡ Vertical direction (Z) membrane stress
- $S_H$  ≡ Horizontal direction (X or Y) membrane stress
- $S_{HZ}$  ≡ Shear membrane stresses on the plane of the plate.
- Bending stresses across the plate thickness are negligible and are classified as secondary stresses; however, other directions of the plate contain primary bending stresses that are included in the stress analysis results.

**Table 3-12**  
**Axis and Hinge Stress Results**

Stress Category	Calculated Stress (MPa)	Allowable Stress (MPa)
Level A Conditions Maximum Membrane Stresses	$S_Z = 3.8$	134.1
	$S_H = 1.6$	134.1
	$S_{HZ} = 1.1$	80.4
Level D Conditions Maximum Membrane Stresses	$S_Z = 106$	195.2
	$S_H = 130$	195.2
	$S_{HZ} = 31.3$	198.6

3.5.2.5 15 mm Thick Support-Base Stiffener Plates

The maximum stress obtained for the 15 mm thick stiffener plates and welds compared with the corresponding allowable stresses are given in Table 3-13, where:

- $S_Z$  ≡ Vertical direction (Z) membrane stress
- $S_H$  ≡ Horizontal direction (X or Y) membrane stress
- $S_{HZ}$  ≡ Shear membrane stresses on the plane of the plate
- Bending stresses across the plate thickness are negligible and are classified as secondary stresses; however, other directions of the plate contain primary bending stresses that are included in the stress analysis results.

**Table 3-13**  
**15mm Thick Stiffener Plates Stress Results**

Stress Category	Calculated Stress (MPa)	Allowable Stress (MPa)
Level A Conditions Maximum Membrane Stresses	$S_Z = 2.6$	134.1
	$S_H = 8.9$	134.1
	$S_{HZ} = 3.2$	80.4
Level D Conditions Maximum Membrane Stresses	$S_Z = 127$	195.2
	$S_H = 138$	195.2
	$S_{HZ} = 54$	198.6

The stress results in stiffeners welds (7 mm double fillet) are enveloped by the above stress results in plates.

3.5.2.6 15 mm Thick Folded Base Plate and (15+15) mm Thick Bolted Support Plates

The maximum stress obtained for the 15 mm thick folded base plate and in (15+15) mm thick bolted support plates compared with the corresponding allowable stresses are indicated in Table 3-14. Stress values for the bolted support plates are based on the following formula from (Reference 9):

$$\sigma = 0.511 \cdot W / t^2, \text{ where } W \text{ is bolt tensile force (see next Table 5.10) and } t = 30 \text{ mm}$$

**Table 3-14**  
**15 mm Thick Folded Base Plate and (15+15) mm Thick Bolted Support Plates Stress Results**

Stress Category	Calculated Stress (MPa)	Allowable Stress (MPa)
Level A Conditions. Folded Base plate	6	201.1
Level D Conditions. Folded Base plate	266	292.8
Level A Conditions. Bolted support plate	1.3	201.1
Level D Conditions. Bolted support plate	124	292.8

**3.5.3 Bolt Stress Results**

The actual stress area available for M24x2 bolts is 374.4 mm<sup>2</sup>, based on the minor diameter of the bolt root of 21.835 mm (Reference 8). The maximum reaction forces obtained at the bolt location and the calculated stresses compared with the corresponding allowable stresses are presented in Table 3-15.

**Table 3-15**  
**Bolt Stress Results**

Stress Category	Reaction Force (N)	Calculated Stress (MPa)	Allowable Stress (MPa)
Level A Conditions. Shear	5390	14.4	123.9
Level A Conditions. Tensile	2239	6.0	300.2
Level D Conditions. Shear	93701	250.2	419.8
Level D Conditions. Tensile	218410	583.3	699.8

In addition, the condition for combined shear and tensile stress  $f_t^2 / F_{tb}^2 + f_v^2 / F_{vb}^2 \leq 1$  is met:

- For the Level A Condition using the above enveloping reactions:

$$f_t^2 / F_{tb}^2 + f_v^2 / F_{vb}^2 = 0.01 \leq 1$$

- Level the D Condition, the equation has to be checked for each bolt:

Node#	Rx (N)	Ry (N)	Rz (N)	Shear (N)	Tensile (N)	Tensile stress (MPa)	Shear Stress (MPa)	ft2/ Ftb2+ fv2/ Fvb2
1038	89212	26741	194960	93134	194960	520.7	248.7	0.90
3164	48239	21506	218390	52816	218390	583.2	141.0	0.81
5290	29986	25363	215010	39274	215010	574.2	104.9	0.74
7416	26379	24320	170220	35879	170220	454.6	95.8	0.47
8479	26785	24359	170490	36205	170490	455.3	96.7	0.48
10605	29922	25807	215190	39514	215190	574.7	105.5	0.74
12731	47734	22698	218380	52856	218380	583.2	141.2	0.81
14857	89600	27417	194450	93701	194450	519.3	250.2	0.91
15972	89230	26730	194980	93148	194980	520.7	248.8	0.90
18055	48239	21517	218410	52820	218410	583.3	141.1	0.81
20137	29986	25369	215020	39278	215020	574.2	104.9	0.74
22224	26375	24315	170220	35873	170220	454.6	95.8	0.47
23265	26786	24361	170490	36207	170490	455.3	96.7	0.48
25344	29921	25802	215180	39510	215180	574.7	105.5	0.74
27422	47733	22686	218370	52850	218370	583.2	141.1	0.81
29493	89582	27429	194430	93687	194430	519.2	250.2	0.91

and it is verified that:

$$\max (f_t^2 / F_{tb}^2 + f_v^2 / F_{vb}^2) = 0.91 \leq 1$$

### 3.5.4 Fuel Impact Forces Analysis

In order to obtain the maximum fuel impact forces, a simplified finite element model for the FSR is built with ANSYS 10.0 (Reference 7), one model for the North-South direction and one for the East-West direction.

Each simplified model is composed of 2-D elastic beam BEAM3 elements, and concentrated mass MASS21 elements.

A vertical line of beam elements represents the enveloping plate of the FSR cells, and another vertical line of beam elements represents the fuel elements assembly.

The area properties and inertias of the cell beams have been adequately adjusted so that the model will have the same eigenfrequencies as the detail model in Section 3.4.5. The structural characteristics of the fuel assembly beams are adjusted based on their first axial frequency (ID 4), their axial area, and their moment of inertia.

The coupling between FSR cell and fuel beam immersed in water, are modeled through MATRIX27 elements applied by node pairs (see Reference 10 for details).

Mass elements reproducing the mass of internal water are considered on the connection nodes of the beam elements simulating the FSR cells.

The fuel beam is coupled in the horizontal direction with the FSR beam at the bottom node. One vertical contact element is located at this same location to evaluate whether the fuel uplifts then impacts with a vertical load when it falls and strikes the base plate.

Between the FSR beam top node and fuel beam top node, two horizontal contact elements (one for each direction of movement) are located to evaluate any potential lateral impacts that may be produced against the FSR cells. The stiffness of these contacts has been estimated by a local analysis made with the detail analysis model, applying local loads at the top cell level.

Based on the acceleration time-histories corresponding to the SSE (ID 8), double integration is used to generate the displacement histories to be applied at the node of the model that represent the pool. Intervals of 0.005 s were used, which means 3200 load steps for a 16-s transient.

The dead weight and the buoyancy effects are considered during the process by application of a constant vertical downward acceleration value of 8.6 g (reduced gravity acceleration, see Section 3.4.6.1).

The maximum impact loads obtained from the this local analysis are:

$$\text{Maximum top fuel horizontal force} \Rightarrow \text{FHT} \approx 1.2 \text{ E}+4 / 28 = 429 \text{ N}$$

$$\text{Maximum bottom fuel horizontal force} \Rightarrow \text{FHB} \approx 5.3 \text{ E}+4 / 28 = 1893 \text{ N}$$

$$\text{Maximum bottom fuel vertical force} \Rightarrow \text{FHT} \approx 150 \text{ E}+4 / 28 = 53571 \text{ N}$$

The stresses produced by these impact forces are analyzed using the detailed FSR model defined in Section 3.4.5. The analysis is only focused on the stress produced for the FSR fuel base plate, since the top fuel impact forces obtained are low and therefore judged to be insignificant.

The impact forces are applied in the three directions by nodal forces on the circular holes of the fuel support base plate.

The vertical fuel impact forces have high values. For this reason a plastic material analysis is considered for the FSR fuel base plate. The plastic stress-strain material curve is obtained from Reference 11.

The stress distribution on the base plate is show in Figure E-30. The maximum stress is  $S_{\max} = 180 \text{ MPa}$ .

This maximum stress is lower than the maximum membrane plus bending admissible stress from Appendix F, F-1341.2 Reference 4,  $S_{\text{adm}} = 0.9 \times S_U = 436 \text{ MPa}$ .

### 3.6 CONCLUSIONS

The analyses performed for the FSRs with the geometry of drawings ID 1, 2, 3 and 6 demonstrate the integrity of these structures when subjected to the applicable loads and load combinations as described in the report.

The analyses presented herein demonstrate that the FSR satisfy the structural requirements of ASME B&PV Code, Section III, Subsection NF (Reference 3) for all proposed loading condition specified in FSR Design Specification (ID 4).

The geometry analyzed corresponds to a continuous 2x14 cell rack, formed by joining two 2x7 cell racks per drawing ID 6, because:

- The racks response is dependant on bending in the out of plane direction (or short, dimension), rather than the long dimension.
- Since the forces at rack junctions are assumed to be low, the joining pieces will be simple as designed.
- Additionally, the base plate is a “very rigid” structure that is bolted to the pool floor and there are no internal forces in the longitudinal direction to connect cells. In other words, the connection of racks is through the concrete at the pool floor. Therefore, it is not necessary to utilize a steel base plate connection.

Table 3.2 summarizes results obtained from the analysis of the FSR components: plate thickness, welds, and anchor bolts. Included in the table are the ratios of the actual results with their allowable values.

### 3.7 REFERENCES

1. ASME Boiler & Pressure Vessel Code, Section II Materials, Part A Ferrous Material Specifications, 2001 Edition with Add. 2003
2. ASME Boiler & Pressure Vessel Code, Section II Materials, Part D Properties (Customary), 2001 Edition with Add. 2003
3. ASME Boiler & Pressure Vessel Code, Section III Rules for Construction of Nuclear Facility Components, Division 1, Subsection NF, Supports, 2001 Edition with Add. 2003
4. ASME Boiler & Pressure Vessel Code, Section III Rules for Construction of Nuclear Facility Components, Division 1, Appendices, 2001 Edition with Add. 2003
5. Regulatory Guide 1.92, Rev. 1. Combining Modal Responses and Spatial Components in Seismic Response Analysis
6. Sarpkaya: Mechanics of Wave Forces on Off-Shore Structures
7. ANSYS 10.0 Documentation (User Manual, Theoretical Manual)
8. ASME B1.13M-2001 Metric Screw Threads: M Profile
9. ROARK'S Formulas for Stress & Strain, 6<sup>th</sup> Edition
10. 092-175-F-M-00001, Issue 2, Spent High Density Fuel Storage Racks Design Report

11. NUREG/CR-0481, "An Assessment of Stress-Strain Data Suitable for Finite-Element Elastic-Plastic Analysis of Shipping Containers", H.J. Rack y G.A. Knorovsky, Syia Laboratories, SY77-1872, September 1978
12. Regulatory Guide 1.61, Rev.1. Damping Values for Seismic Design of Nuclear Power Plants

**APPENDIX E - FIGURES**

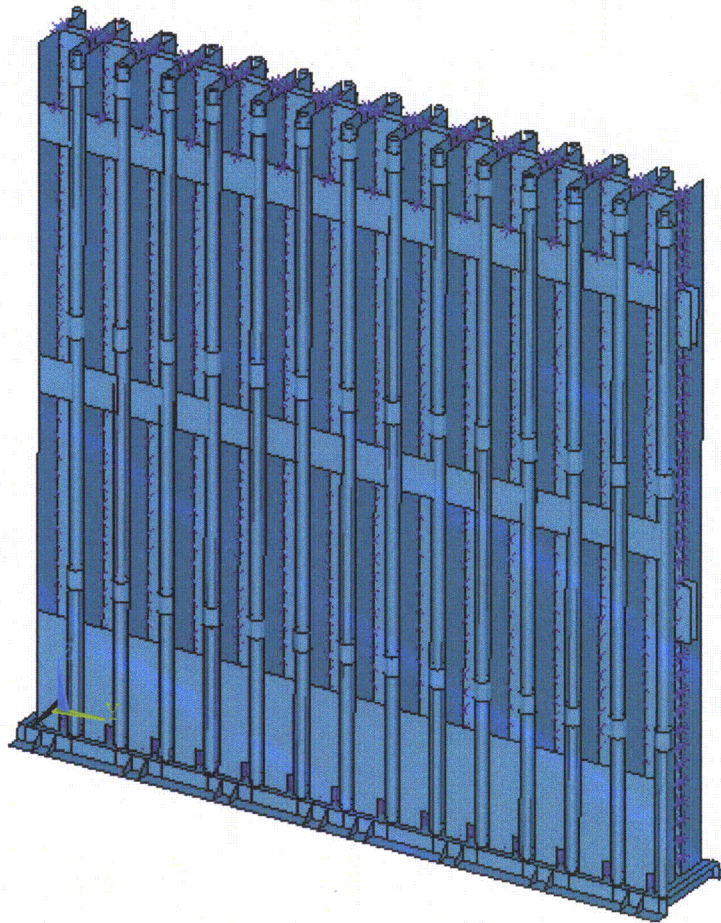


**Figure E-1. FSR FEM**

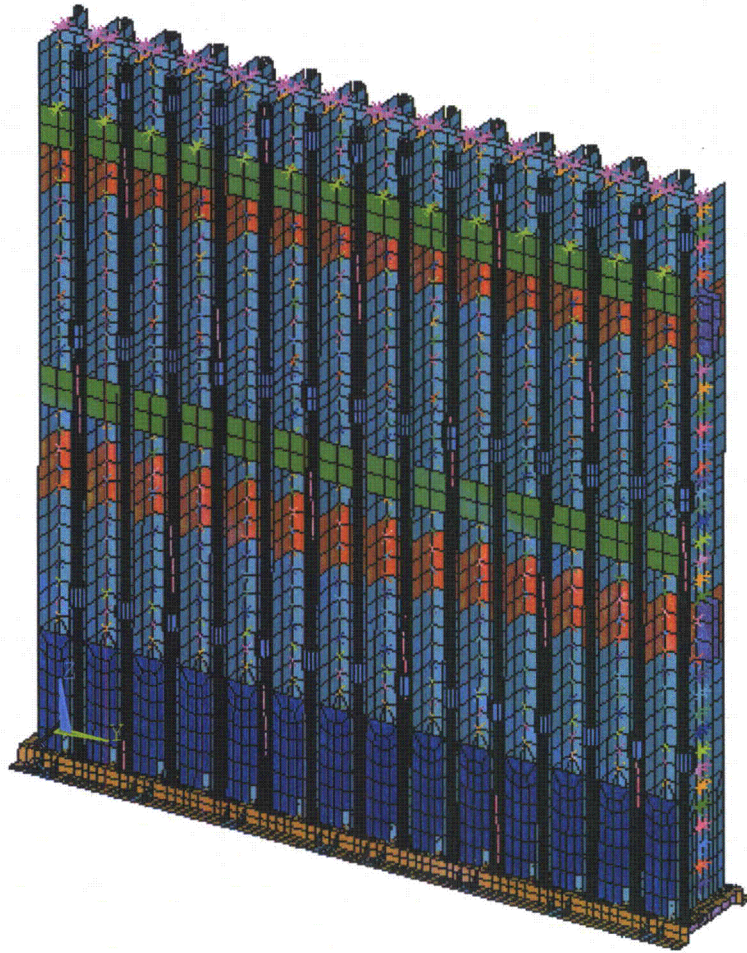


**Figure E-2. FSR FEM**

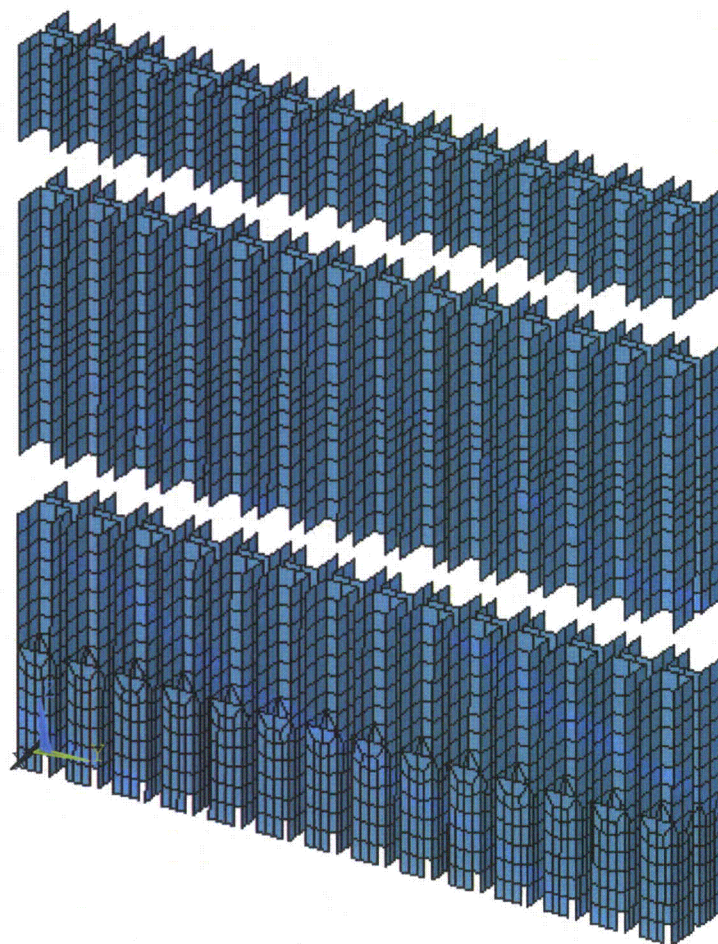


**Figure E-3. FSR FEM 8 mm Thick Channel Plates**

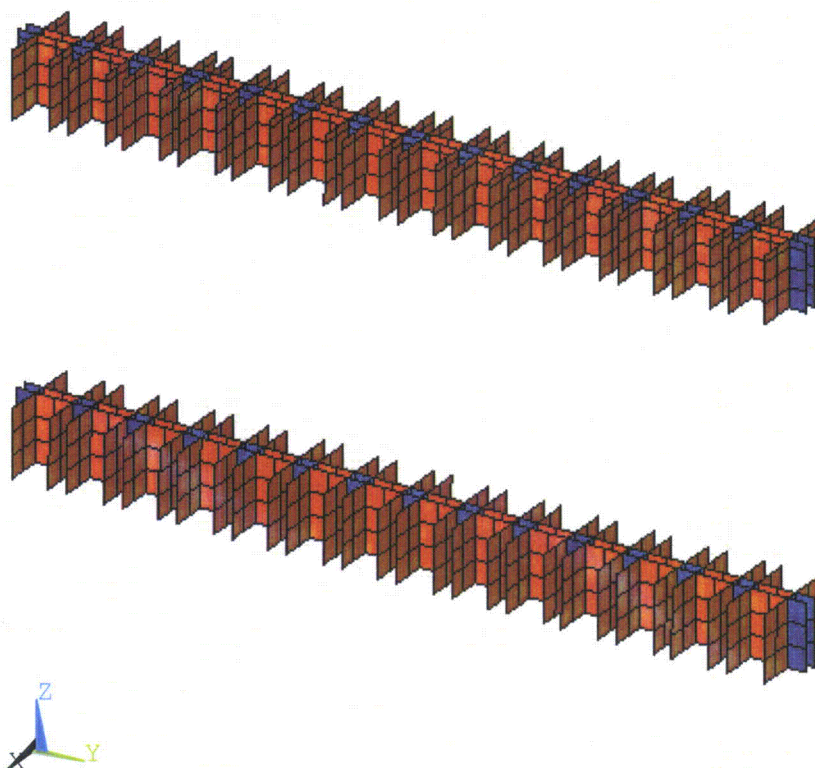


**Figure E-4. FSR FEM (10+8) mm Thick (Grid+Channel) Plates in Red, and  
10 mm Thick Grid Plates in Purple**

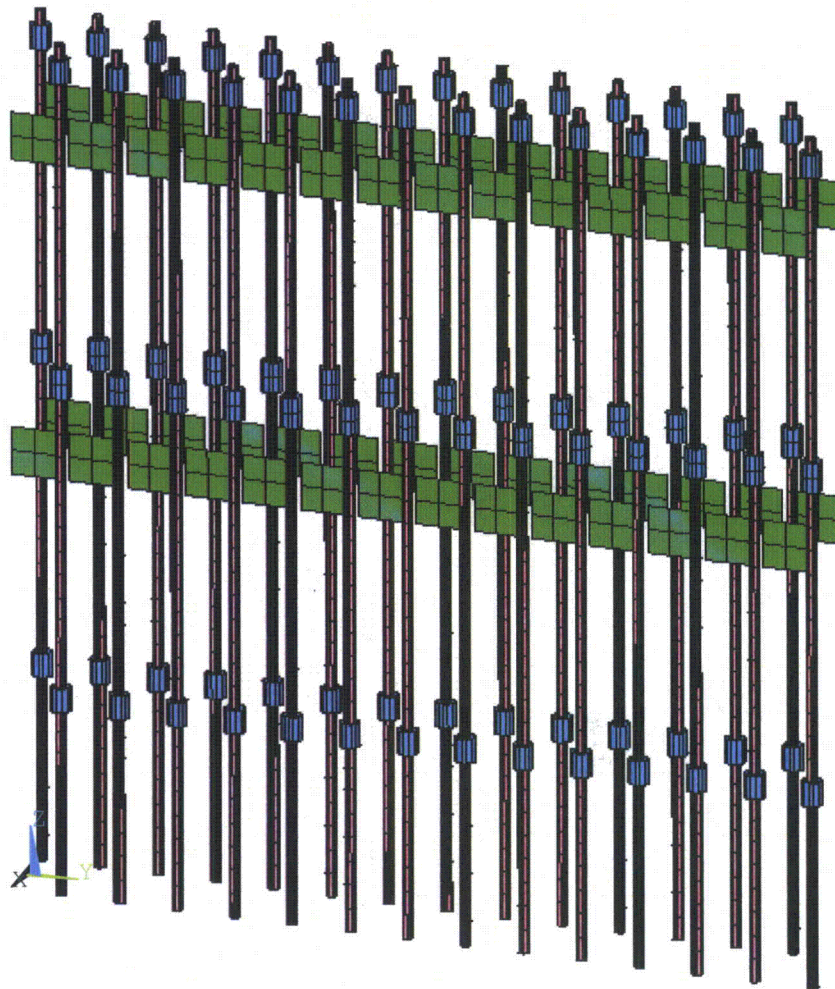


**Figure E-5. FSR FEM 12 mm Thick Door Plates, 7.5 mm Thick Door Axis Plate and 10 mm Thick Hinge Plates**

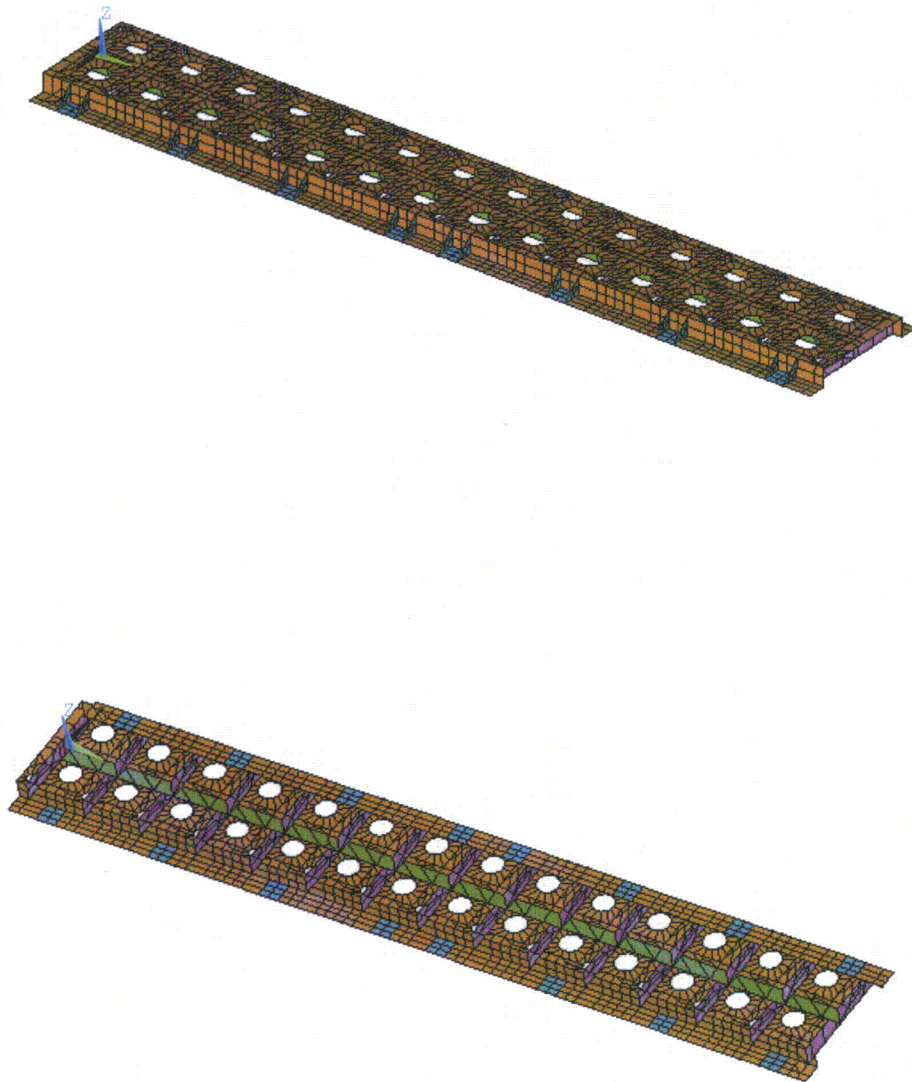


**Figure E-6. FSR FEM 15 mm Thick Support-Base Plate and Stiffener Plates, and (15+15) mm Reinforced Bolted Plate in L1ue**

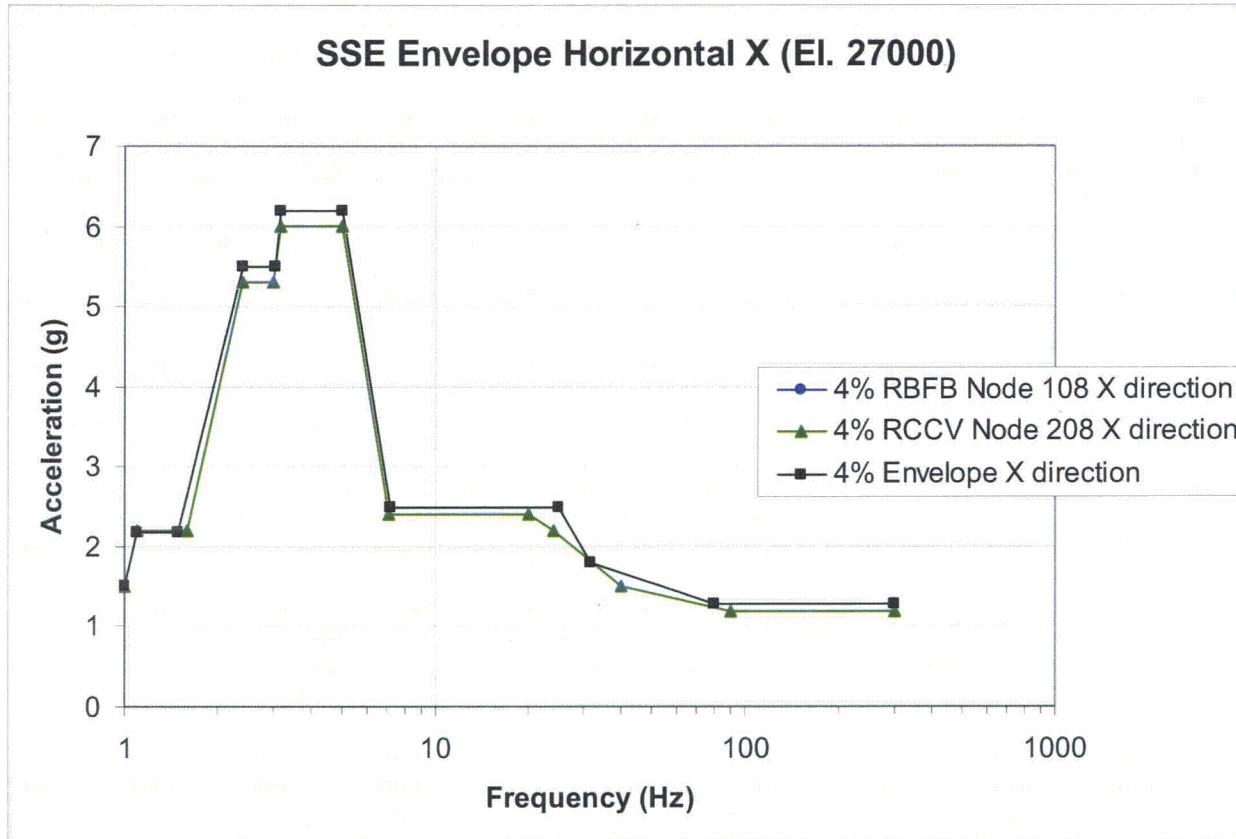


Figure E-7a. SSE Horizontal X Enveloping Floor Response Spectra

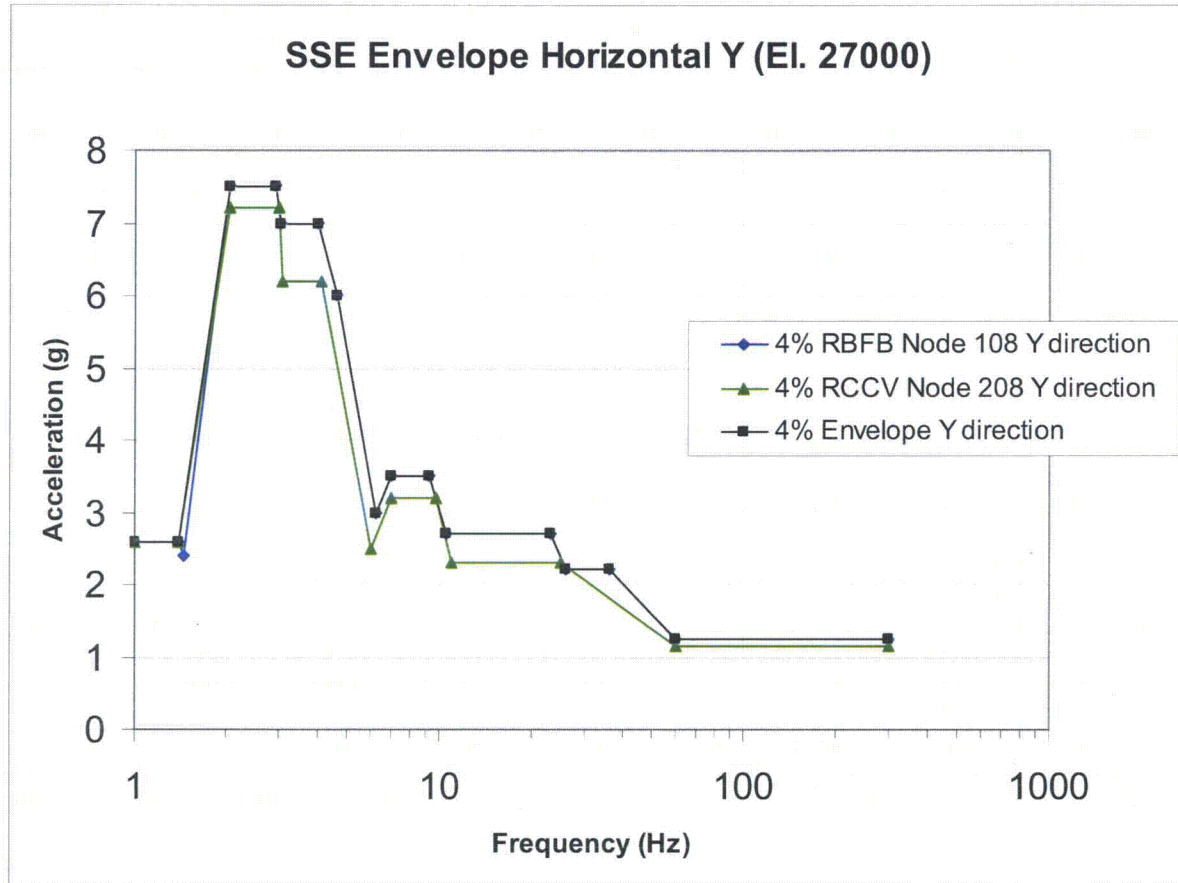


Figure E-7b. SSE Horizontal Y Enveloping Floor Response Spectra

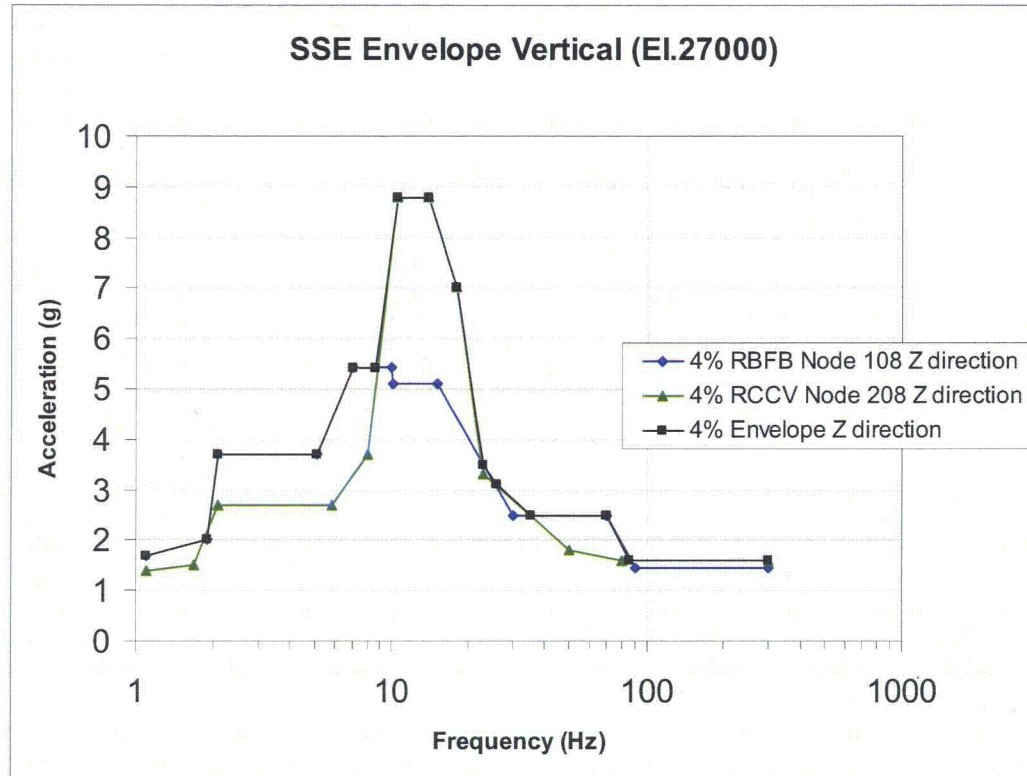


Figure E-8. SSE Vertical Enveloping Floor Response Spectra

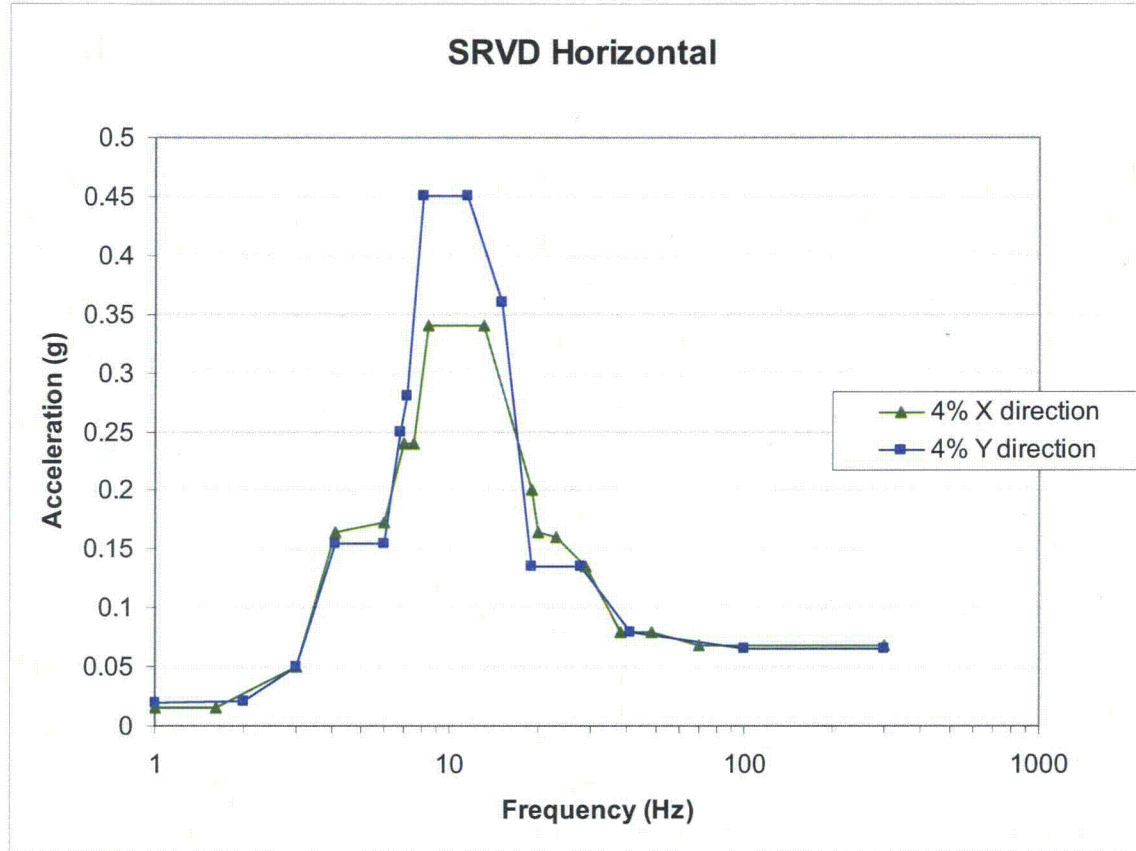


Figure E-9. SRVD Horizontal Enveloping Floor Response Spectra

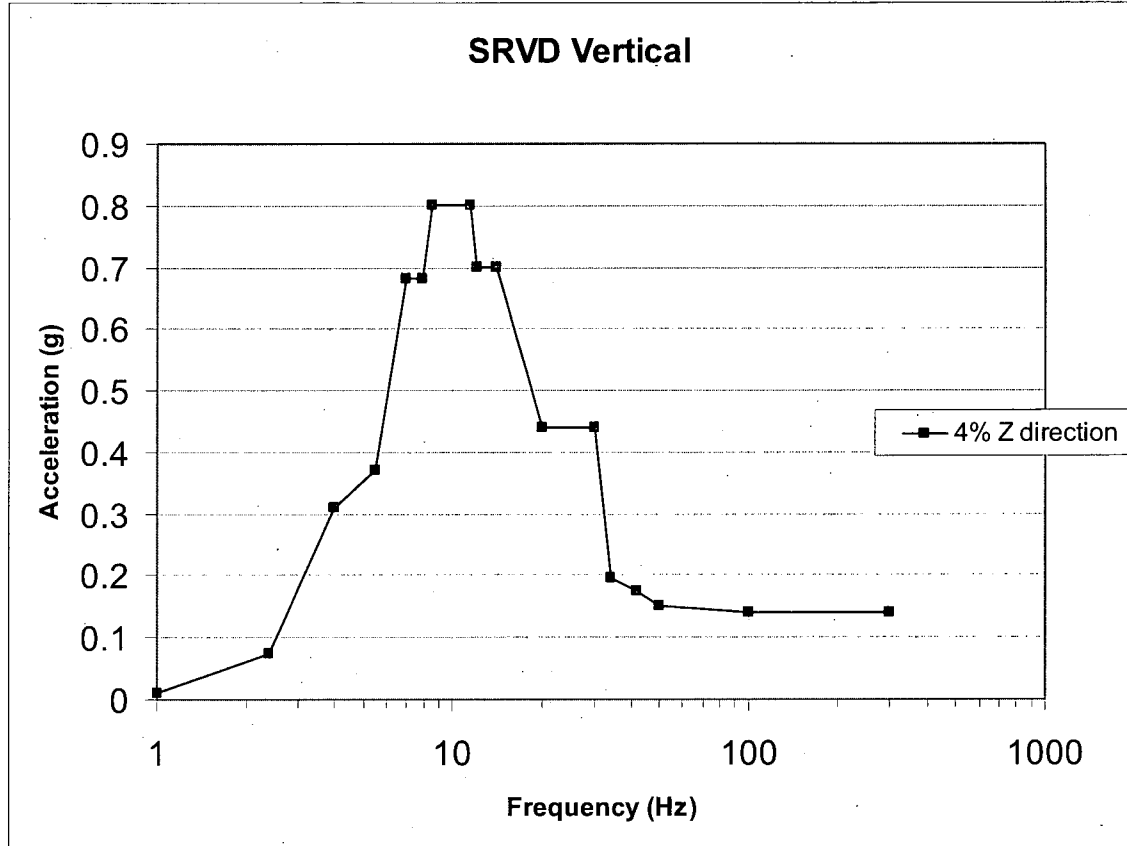


Figure E-10. SRVD Vertical Enveloping Floor Response Spectra

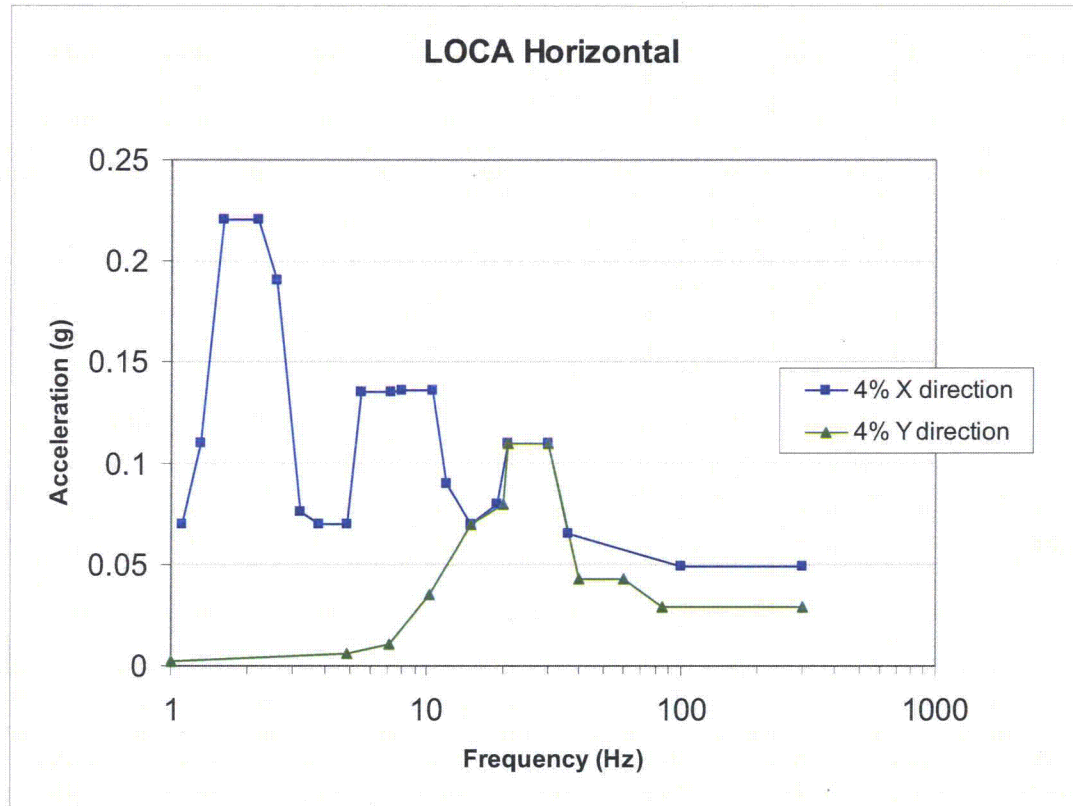


Figure E-11. LOCA Horizontal Enveloping Floor Response Spectra

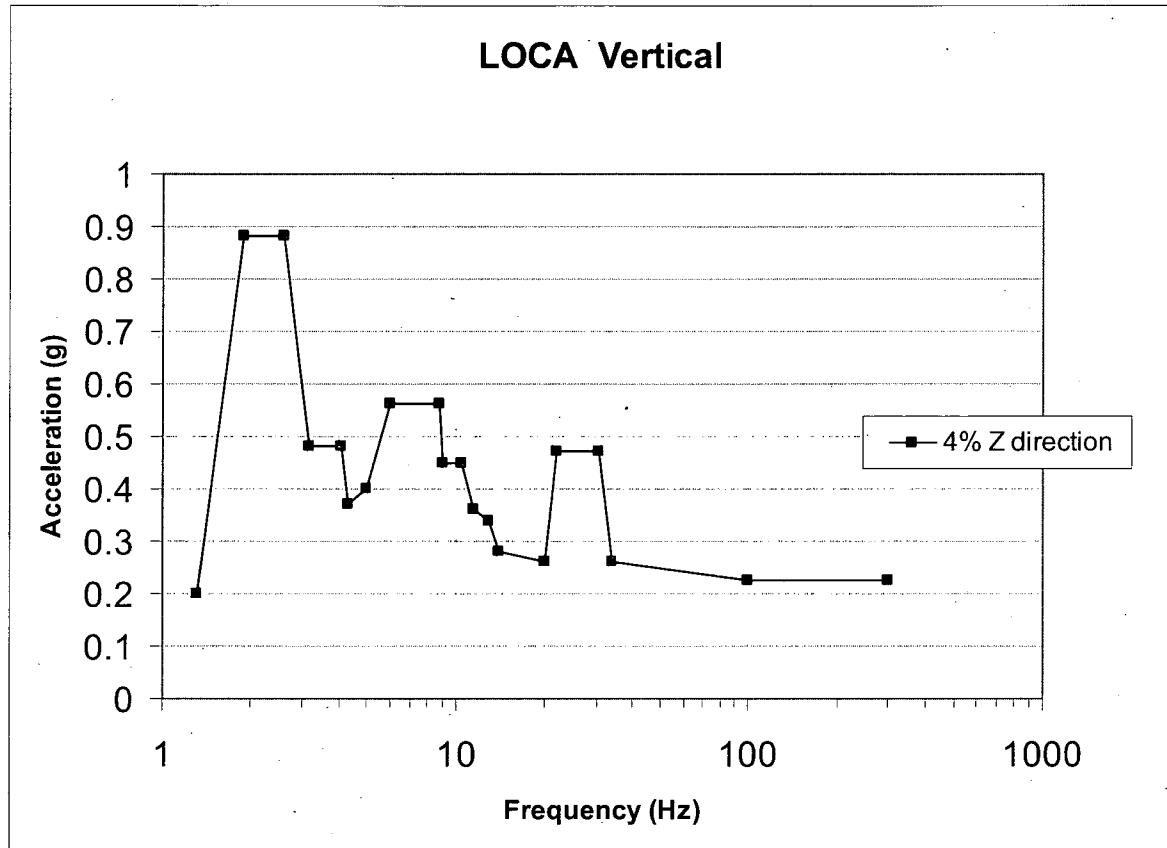


Figure E-12. LOCA Horizontal Enveloping Floor Response Spectra

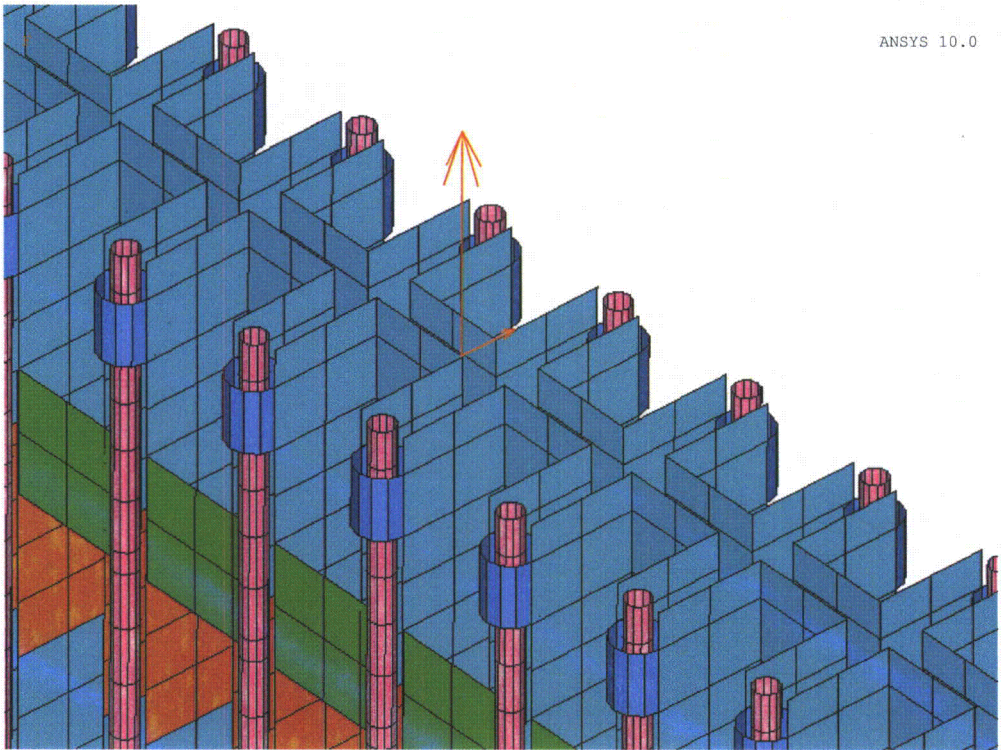
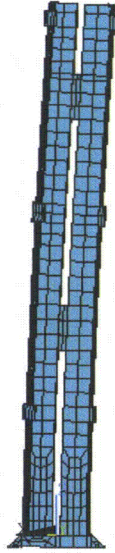


Figure E-13. FSR Fuel Handling Loads

-----  
STEP=1  
SUB =1  
FREQ=7.058  
RSYS=0  
DMX =.012838  
-----



**Figure E-14. FSR Deformed Shape Eigenmode 1**

STEP=1  
SUB =2  
FREQ=7.215  
RSYS=0  
DMX =.021728

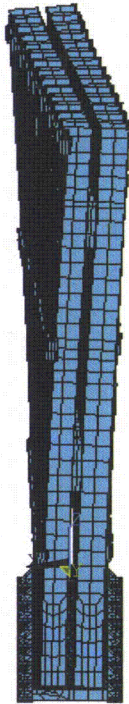


**Figure E-15. FSR Deformed Shape Eigenmode 2**

STEP=1  
SUB =3  
FREQ=9.572  
RSYS=0  
DMX =.025428

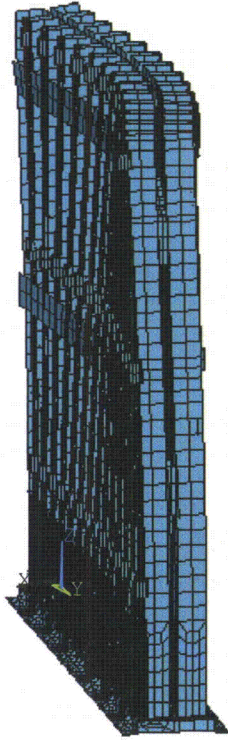


**Figure E-16. FSR Deformed Shape Eigenmode 3**

STEP=1  
SUB =4  
FREQ=14.474  
RSYS=0  
DMX =.026132

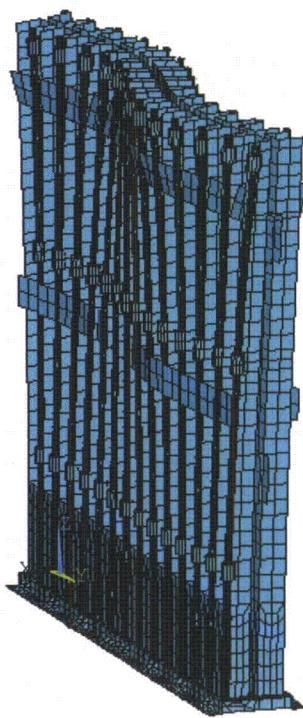


**Figure E-17. FSR Deformed Shape Eigenmode 4**

STEP=1  
SUB =5  
FREQ=16.797  
RSYS=0  
DMX =.013647

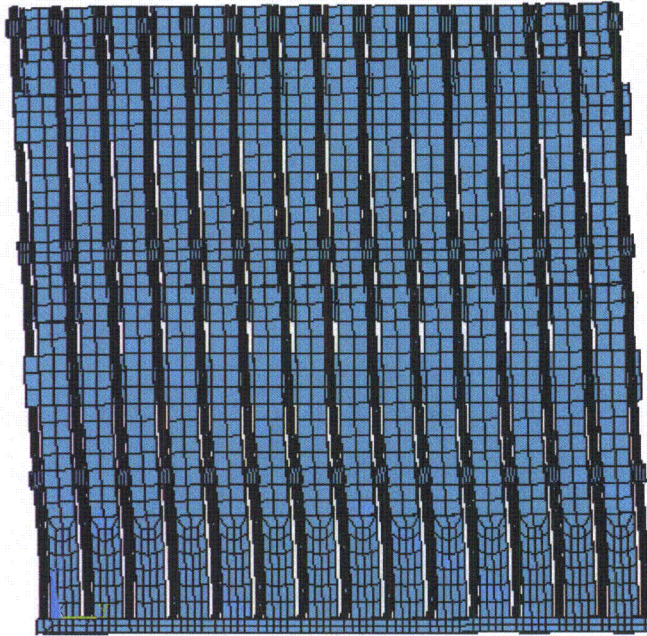


**Figure E-18. FSR Deformed Shape Eigenmode 5**

STEP=1  
SUB =31  
FREQ=33.17  
RSYS=0  
DMX =.02189

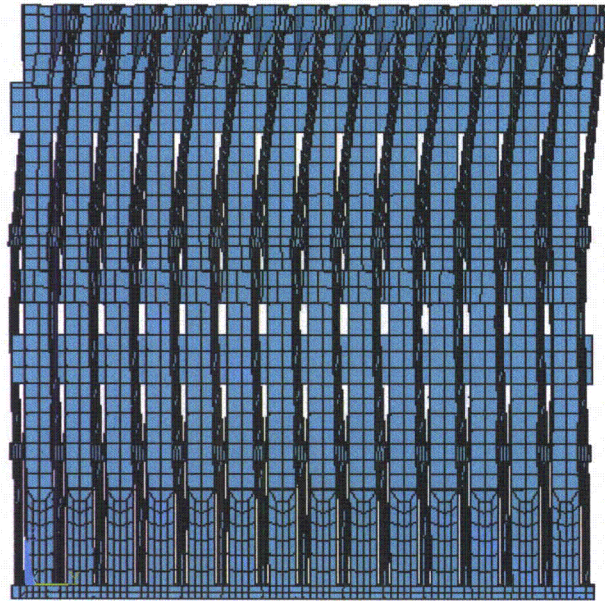


**Figure E-19. FSR Deformed Shape Eigenmode 31**

STEP=1  
SUB =31  
FREQ=33.17  
RSYS=0  
DMX =.02189

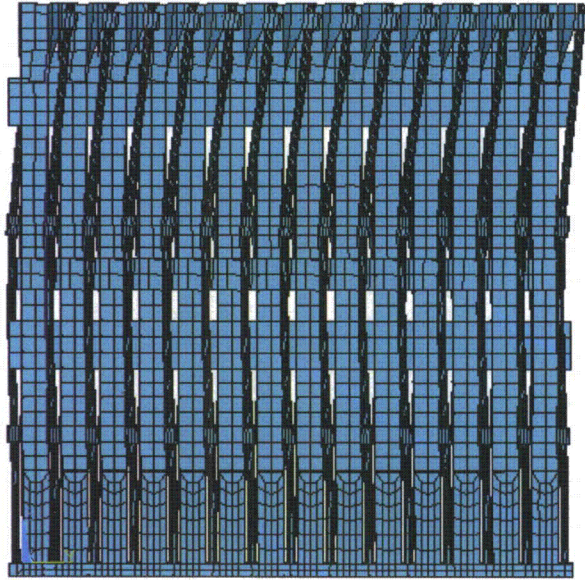


**Figure E-20. FSR Deformed Shape Eigenmode 61**

STEP=1  
SUB =63  
FREQ=51.019  
RSYS=0  
DMX =.069377

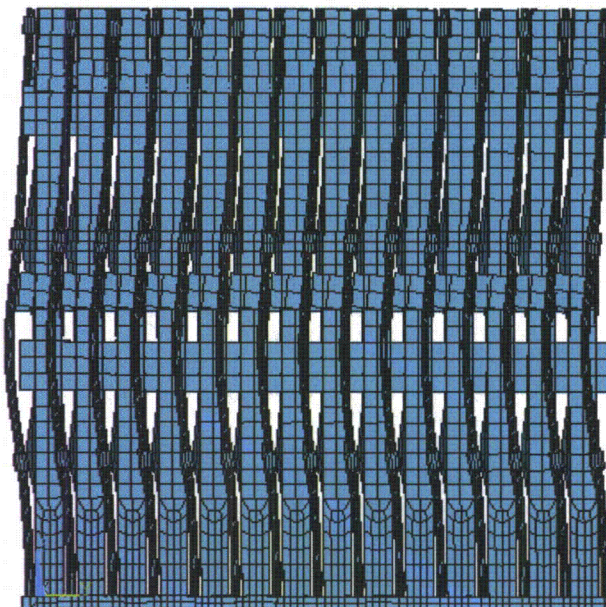


**Figure E-21. FSR Deformed Shape Eigenmode 63**

STEP=1  
SUB =69  
FREQ=54.236  
RSYS=0  
DMX =.108781



**Figure E-22. FSR Deformed Shape Eigenmode 69**

STEP=1  
SUB =71  
FREQ=54.423  
RSYS=0  
DMX =.116733



**Figure E-23. FSR Deformed Shape Eigenmode 71**

UX  
TOP  
RSYS=0  
DMX = .018213  
SMN = -.018165  
SMX = .018039

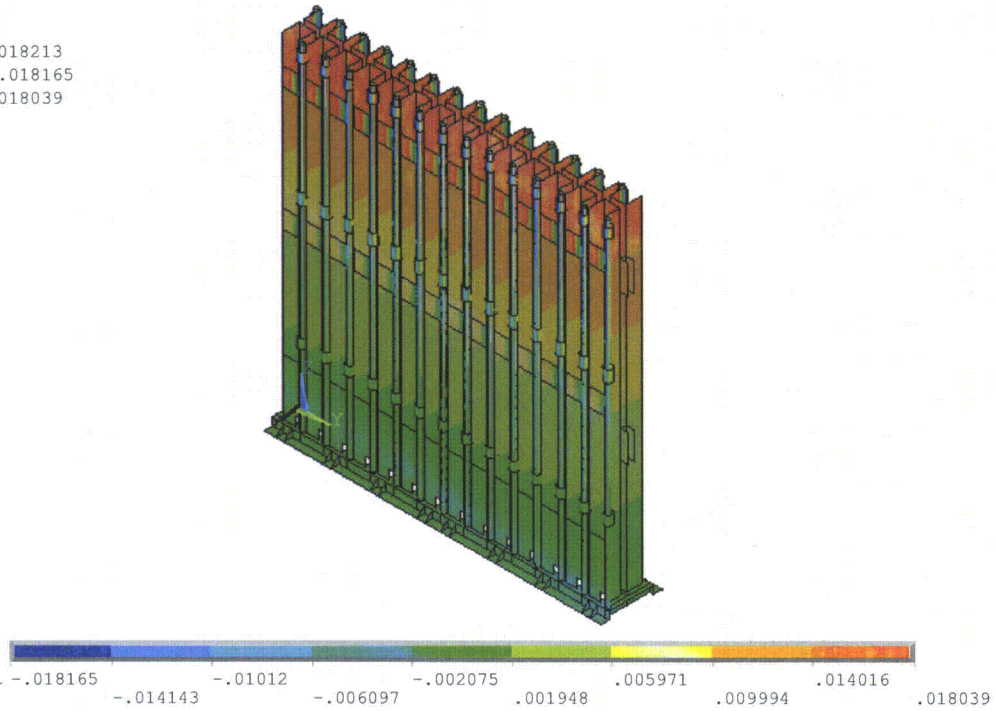


Figure E-24. FSR Horizontal Displacement X (m)

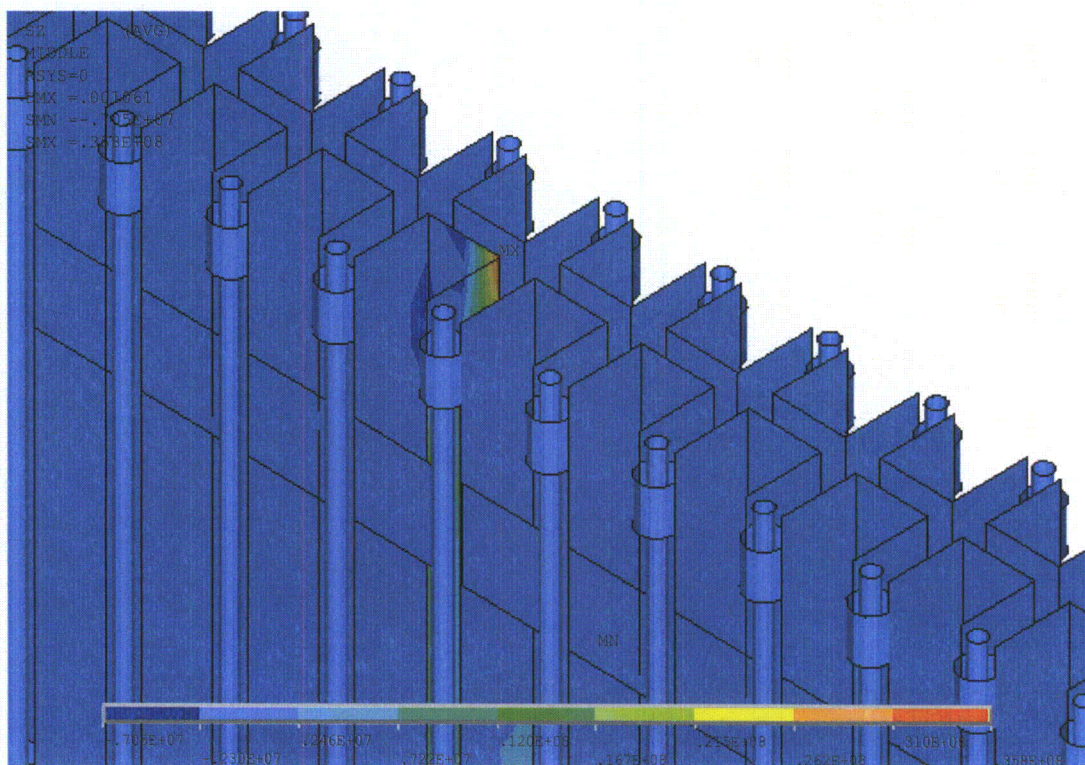


Figure E-25. FSR 8 mm Channel Plates. Level A Vertical Stress (N/m<sup>2</sup>)

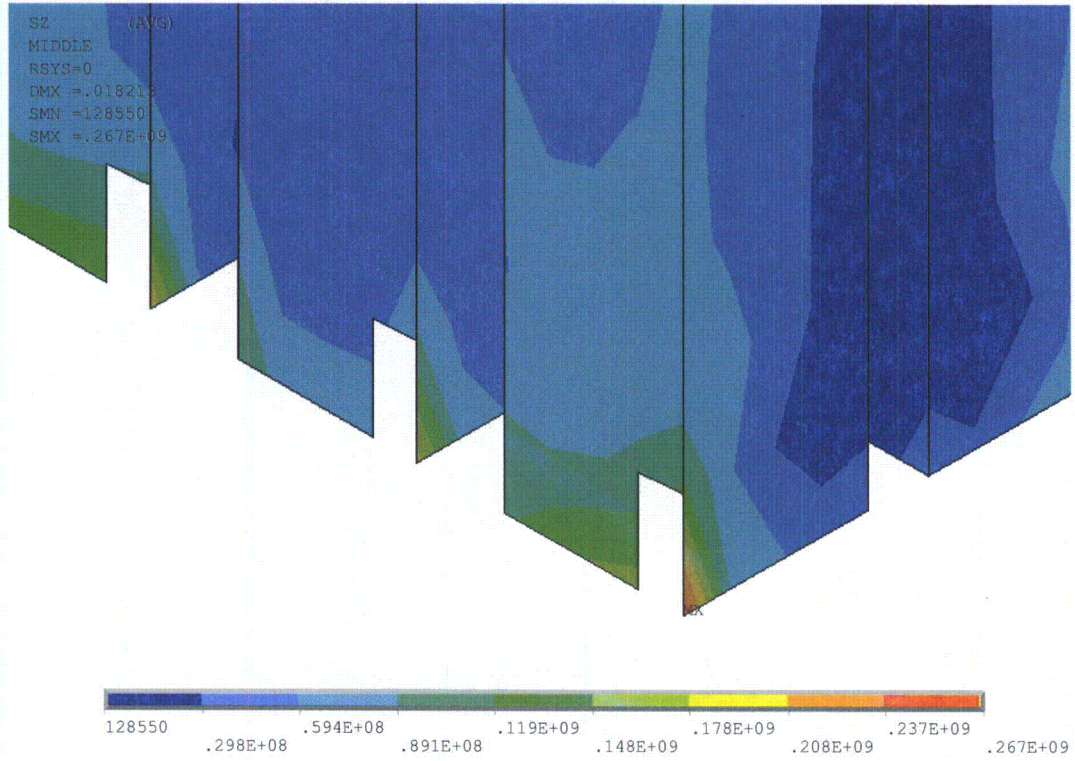


Figure E-26. FSR 8 mm Channel Plates. Level D Vertical Stress (N/m<sup>2</sup>)

SUB =1  
SY (AVG)  
MIDDLE  
RSYS=0  
DMX =.017416  
SMN =109050  
SMX =.123E+09

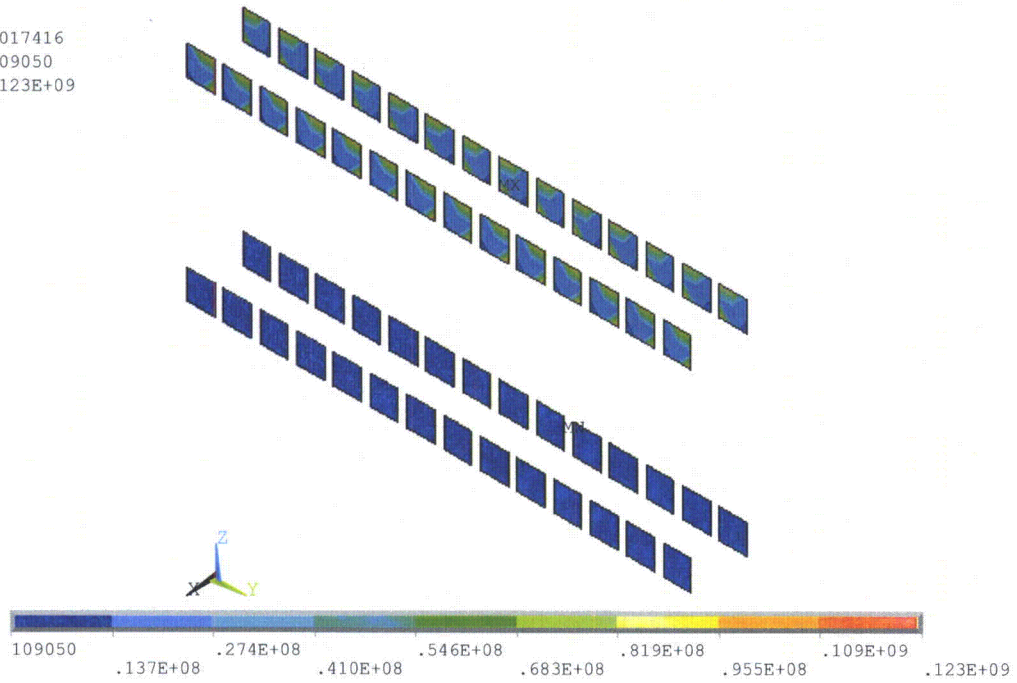


Figure E-27. FSR 12 mm Door Plates. Level D Horizontal Stress (N/m<sup>2</sup>)

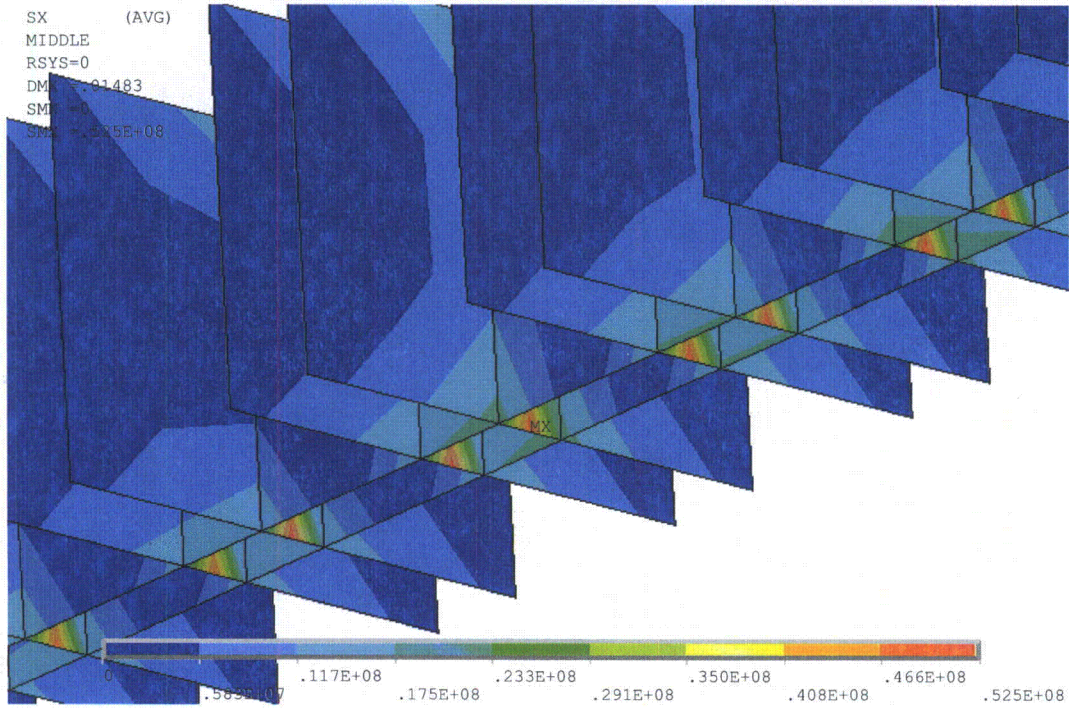


Figure E-28. FSR Assembly Grid Plate. Level D Horizontal Stress (N/m<sup>2</sup>)

SZ (AVG)  
MIDDLE  
RSYS=0  
DMX =.369E-03  
SMN =-.741E+07  
SMX =.473E+08

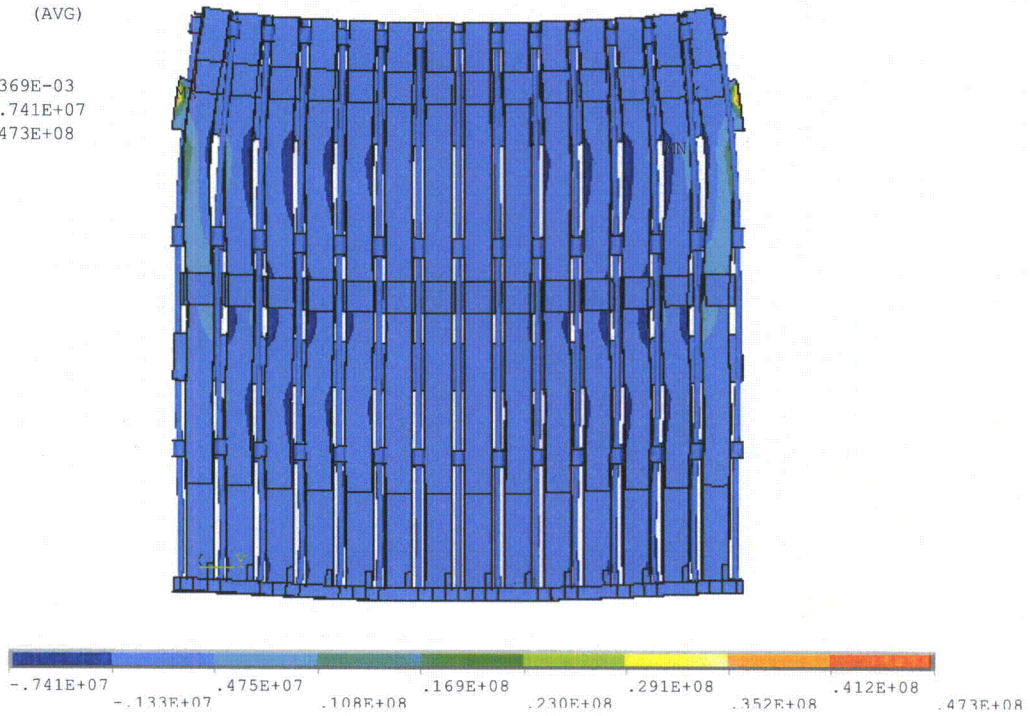
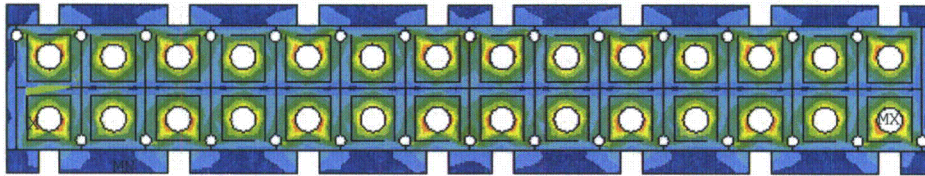


Figure E-29. Lifting Load Stresses (N/m<sup>2</sup>)

SINT (AVG)  
TOP  
DMX =.425E-03  
SMN =.215E+07  
SMX =.180E+09



**Figure E-30. Fuel Impact Forces. Base Plate Stresses (N/m<sup>2</sup>)**

**APPENDIX F - (DELETED)**

## 4. LOAD-DROP (IMPACT) ANALYSIS

### 4.1 INTRODUCTION

Load drop analysis is required in the design of fuel storage racks for new and spent fuel elements. All the racks have to withstand a number of operational and accidental loads. This section is concerned with the effects of postulated impacts arising from the accidental drop of fuel elements onto the various racks during operations at the plant.

#### 4.1.1 *Object*

The object of the work consists of evaluating the performance of the ESBWR racks when they are subjected to postulated accidental impacts from fuel elements. There are two types of racks to be considered: racks for spent fuel and racks for fresh fuel.

In the case of the spent fuel racks, the dropped mass may impact the upper part of the rack, in which case the distortions caused should not affect criticality (i.e. should not reach the active zones of the elements stored in adjoining cells); also, fuel cells other than those directly involved in the impact should not be affected by the accident. Alternatively, the dropped mass may not interact with the upper part of the rack, but enter a cell and proceed all the way to the bottom plate, which should then be capable of successfully arresting the falling mass.

In the case of the fresh fuel racks, the dropped mass may impact the upper part of the short wall of the cell, an accident that should not affect the walls separating contiguous elements. Alternatively, it could continue to impact the bottom plate, which should be capable of successfully arresting the falling mass.

#### 4.1.2 *Scope*

In order to carry out the evaluations mentioned, the necessary data was first acquired and critically assessed. When the value of a parameter could vary over a range, conservative assumptions have been incorporated to evaluate the postulated accidents.

The evaluations have been performed using a combination of computer calculations, hand calculations and engineering judgment, depending on the specific characteristics of the case of interest. The computer calculations are all finite element analyses based on explicit integration in the time domain using Lagrangian formulations. The code Abaqus/Explicit (SIMULIA, 2008) has been used for this task.

As mentioned earlier in relation with spent fuel racks, a dropped element may fall through to the bottom of a cell and impact the base plate of the rack; alternatively, it may be arrested at the top of the storage cells by impact against the upper part of the cell walls. Both possible alternatives have been considered in the present work. For the spent fuel racks, the impacts on the upper part of the cells are supposed to correspond to 6.4 m drops. However, for the impacts on the base plate, the drops are assumed to take place from an elevation of 1.8 m above the top of the racks.

For the fresh fuel racks, the element drops from 1 m above the base plate, thus prescribing the drops heights for impacts against the top of the wall and against the base plate.

It has been assumed that a 201 kg handling tool may or may not accompany the dropped fuel element in all cases; hence the analyses have been repeated with and without the handling tool. Since no specific details are currently known about the handling tool, it has been represented simply as a point mass fixed to the top of the fuel element.

For the spent fuel racks, in which the impacts involve considerable drop heights, the interaction of the falling element with the surrounding water has been taken into account; this removes part of the energy of the dropped element. However, for the impacts against the fresh fuel racks, in which the drop heights are rather small, the effects of this interaction have been conservatively neglected.

### **4.1.3 Layout of Report**

The report is organized as follows:

Section 4.2 describes the problems under consideration, including the geometry and behavior of the falling fuel element and the two types of storage racks, as well as the accident conditions.

The next two sections are dedicated to studying the impacts on spent fuel racks. Section 4.3 is concerned with impacts against the base plate, while Section 4.4 deals with the impacts taking place against the upper part of the rack.

Section 4.5 discusses the impacts against fresh fuel racks, including both the case in which the dropped element impacts the top of the wall and that in which it continues falling through the interior of one of the storage cells to reach the bottom plate.

The conclusions and recommendations derived from the work conducted are presented in Section 4.6.

The appendix contains the list of bibliographic references mentioned in the text of the report.

## **4.2 DESCRIPTION OF THE PROBLEM**

### **4.2.1 The Fuel Element and Handling Tool**

The ESBWR fuel element under consideration is a 10x10 BWR fuel element (GE14E), which is slightly shorter than the traditional fuel elements.

From the viewpoint of the present analyses, the basic mechanical properties of the ESBWR fuel element are the following:

- global mass of the element:  $m = 244$  kg
- length of the element:  $l = 3.671$  m
- first longitudinal frequency:  $f_1 = 124$  Hz

The geometrical shape of the nose at the bottom of the element must be reproduced fairly precisely in the models in order to achieve realistic results during the interaction, but it only involves a comparatively small mass. Apart from that mass, the rest of the fuel element is assumed to behave as a uniform elastic bar with the properties listed above; this assumption is conservative in that it maximizes the forces and damage caused to the rack, which would obviously be smaller if the element were assumed to collapse.

Together with the fuel element, the fuel handling tool is assumed to fall. The only known characteristics about the fuel handling tool are its mass of 201 kg and the fact that its cross section would allow it to follow an element entering a cell without interacting with the cell walls. For lack of more detailed information about the tool, it will be represented here as a point mass, rigidly fixed to the top of the fuel element; again this is considered to be a conservative assumption, as the exchange of momentum would be slower with a more deformable tool or connection with the fuel element.

It has been assumed that the falling fuel element will not collapse or undergo plastic deformations. This is always conservative because all the impact energy has to be dissipated in deformations of the impacted rack or kept as kinetic energy (rebound velocity and internal vibrations)

## **4.2.2 Spent Fuel Racks**

### 4.2.2.1 Description

The rack is described in ENSA drawing no. 5926.D200 rev. 02. It is designed to house 15 x 12 fuel elements within a rectangular arrangement measuring 2.541 m x 2.037 m. The height of the storage cells is 3.587 m, with the top of their base plate located at 0.289 m above the bottom of the pool. The thickness of the uppermost plates of the rack is 7 mm. An elevation view of the rack can be seen in Figure 4-1.

The rack rests on four symmetrically arranged supports, located under the four corner cells. The base plate is 20 mm thick and is provided with a partially tapered orifice for engaging the nose of the fuel element. It is reinforced by several stiffeners, as can be seen in Figure 4-2 and is described in ENSA drawing no. 5926.D210 rev. 02.

The storage cells provide a square inner space, 168 mm per side, and their geometry is described in ENSA drawing no. 5926.D220 rev. 00.

Most of the rack is made with borated steel plates with 3.4 mm thickness. However, the base plate of the rack and the uppermost plates of the cells provide greater structural integrity and are free from isolation requirements; as a consequence, these parts are made using SA-240 Tp.304L steel.

The two steels mentioned have been characterised with a Young's modulus of 210 GPa and a yield stress of 206 Mpa (ASME, 2003). The stress-strain curves are similar in both cases except in respect of the ductility, which attains 0.4 for the structural steel but is limited to only 0.09 for the borated steel. The stress-strain curve mentioned is shown in Figure 4-3.

#### 4.2.2.2 Postulated Accidents

The accidents considered involve drops of a fuel element from various heights above the top of the storage cells. The dropped fuel element may impact the upper part of the walls of the storage cells or, alternatively, it may enter one of the cells and, if the cell is empty, continue falling until it is finally arrested by the base plate.

Following the specifications, the impacts against the upper part of the rack are taken to correspond to 6.4 m drops. By contrast, impacts against the base plate are assumed to take place from an elevation 1.8 m above the top of the rack.

The fall of the fuel element takes place through water, which removes some of the energy from the drop. Following GE's practice (GE, 1978), it will be assumed that the interaction with water removes 20% of the energy of an element falling freely in 1.8 m of water. In the case of the element continuing its fall through one of the storage cells, velocities increase and the lateral confinement of the water by the cell walls provides a more effective brake: the interaction with water would remove then 70% of the energy of the falling element prior to its impact with the base plate. For 6.4 m drops onto the top of the rack, the energy dissipation has been calculated so as to maintain consistency with the 20% dissipation occurring over 1.8 m of unrestrained water.

The above considerations entail an impact velocity of 7.82 m/s for the impacts against the top of the storage cells and 5.68 m/s for the impacts against the base plate.

It is important to consider the reasons why the postulated impacts are potentially significant:

1. Damage to the Rack Cells

The distortions caused by the impacts on the upper part of the cells should be limited; in particular the damage should not reach the active part of other elements stored in adjacent cells. Also, cells other than that directly involved in the impact should not be affected by the accident.

2. Damage to the Base Plate

The base plate should be able to successfully arrest the dropped element, thus preventing its progress towards the pool liner.

3. Survival of the Supports

Excessive loads on the supports of the rack could lead to a failure. Conservative analyses must therefore be carried out to determine the forces developed at the supports in order to allow carrying out the necessary verifications.

#### 4.2.3 Fresh Fuel Racks

##### 4.2.3.1 Description

The fresh fuel racks are described in ENSA drawings no. 5926.D500 rev. 00 and 5926.D510 rev. 00. They are designed to house 2x7 fuel elements within a rectangular arrangement measuring

1.836 m x 0.650 m. The total height of the rack is 3.697 m, with the top of the base plate located at 0.110 m above the bottom of the pool. An elevation view of the rack can be seen in Figure 4-4.

The walls of the cells extend all the way from the base plate to the top except for the outer faces. In those faces the wall is only 0.600 m high in order to allow entry of the element, although there is also an operable door at the top in order to restrain a stored element from leaving the cell accidentally.

The base plate is made with 15 mm structural steel plate and has a number of stiffening members. Figure 4-5 presents a view of the base plate of the fresh fuel racks.

The material used for constructing the fresh fuel racks is the same structural steel SA-240 Tp.304L also employed in the spent fuel racks. Its basic mechanical characteristics were already given in Section 4.2.2.1.

#### 4.2.3.2 Postulated Accidents

The accidents considered here involve drops of a fuel element from a height 1.000 m above the base plate of the rack. The dropped fuel element may impact the upper part of the short wall at the bottom of the storage cells or, alternatively, it may continue falling until it is finally arrested by the base plate. Hence impacts against the wall correspond to 0.400 m drops and impacts against the base plate are associated with 1.000 m drops.

The fall of the fuel element takes place through water, which removes some of the energy from the drop. However, since the drop heights are relatively small and so would be the amount of energy dissipation, this effect has been conservatively neglected. These considerations entail an impact velocity of 2.80 m/s for the impacts against the top of the short wall, which increases to 4.43 m/s for impacts against the base plate.

The reasons why the postulated impacts are potentially significant in the context of the fresh fuel racks are the following:

1. Damage to the rack cells

The distortions caused by the impacts on the upper part of the short wall of the cell should be limited; in particular the double wall separating contiguous elements should remain in place in spite of the accident.

2. Damage to the base plate

The base plate should be able to successfully arrest the dropped element, thus preventing its progress towards the pool liner.

3. Survival of the supports

Excessive loads on the supports of the rack could lead to a failure. Conservative analyses must therefore be carried out to determine the forces developed at the supports in order to allow carrying out the necessary verifications.

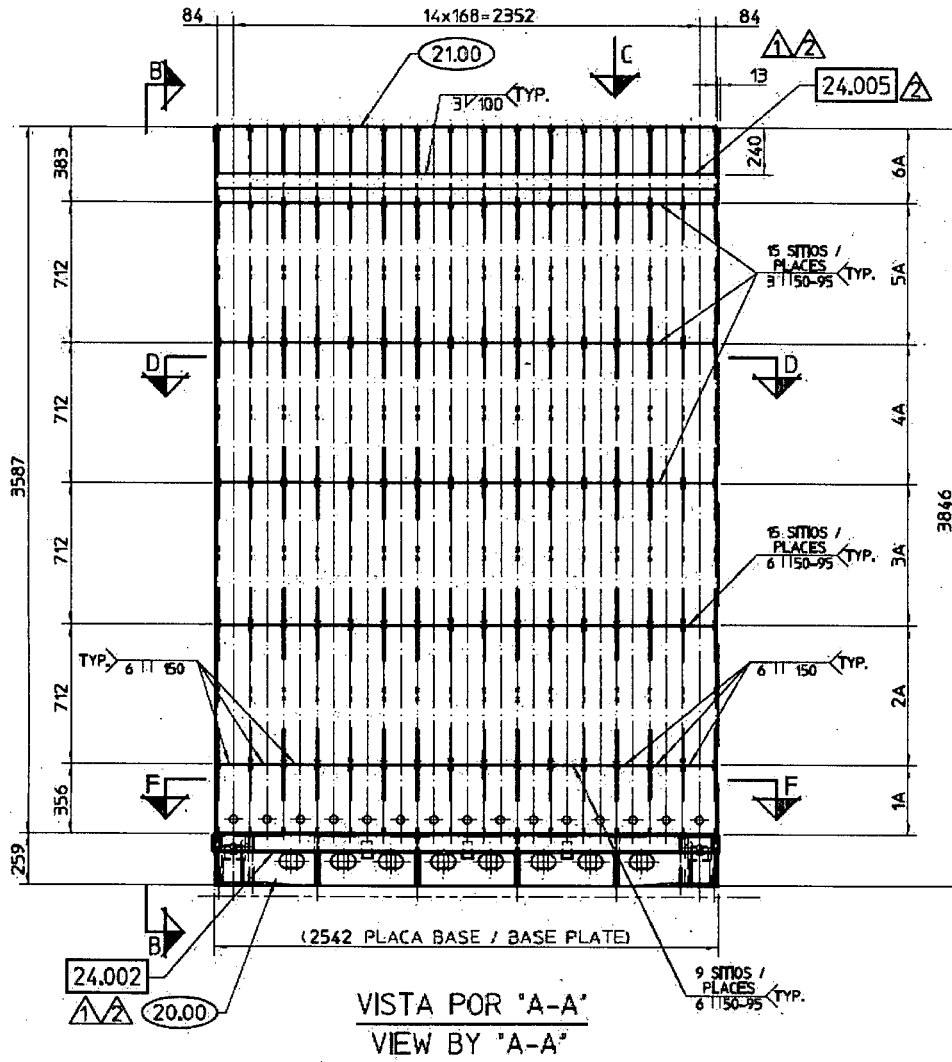


Figure 4-1. Elevation View of the Spent Fuel Rack

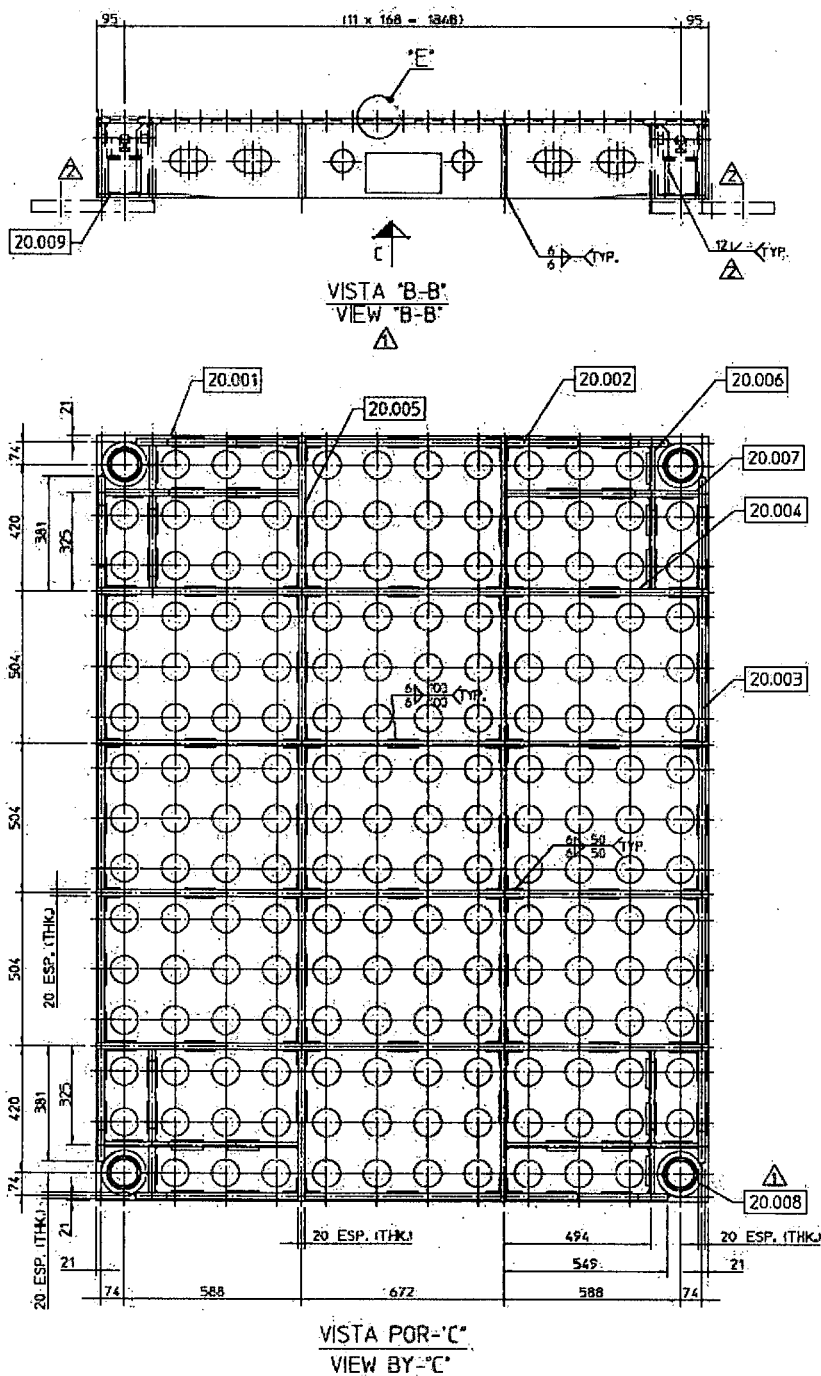
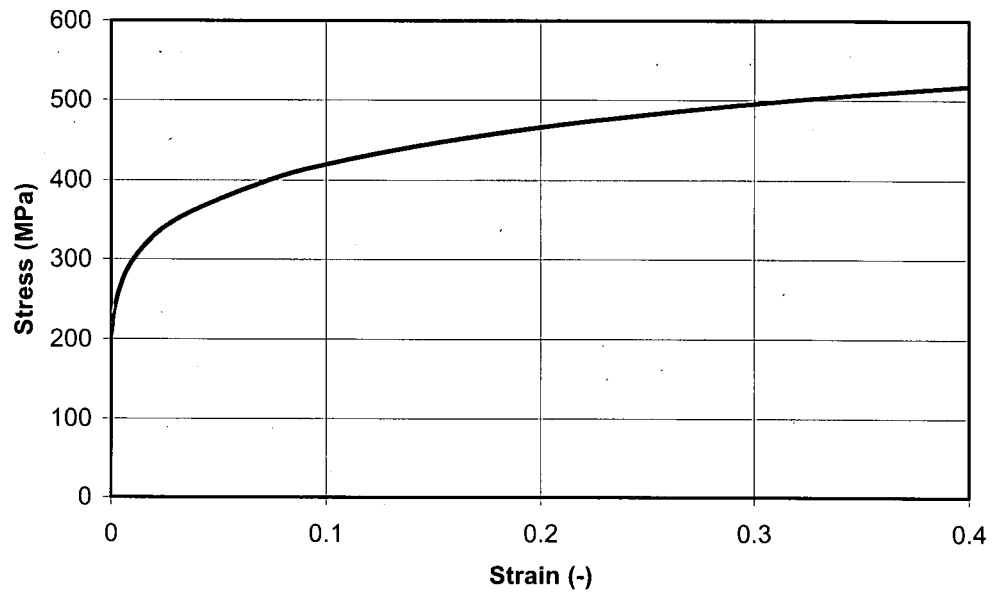


Figure 4-2. Base Plate of the Spent Fuel Rack



**Figure 4-3. Stress-Strain Curve for Structural Steel**

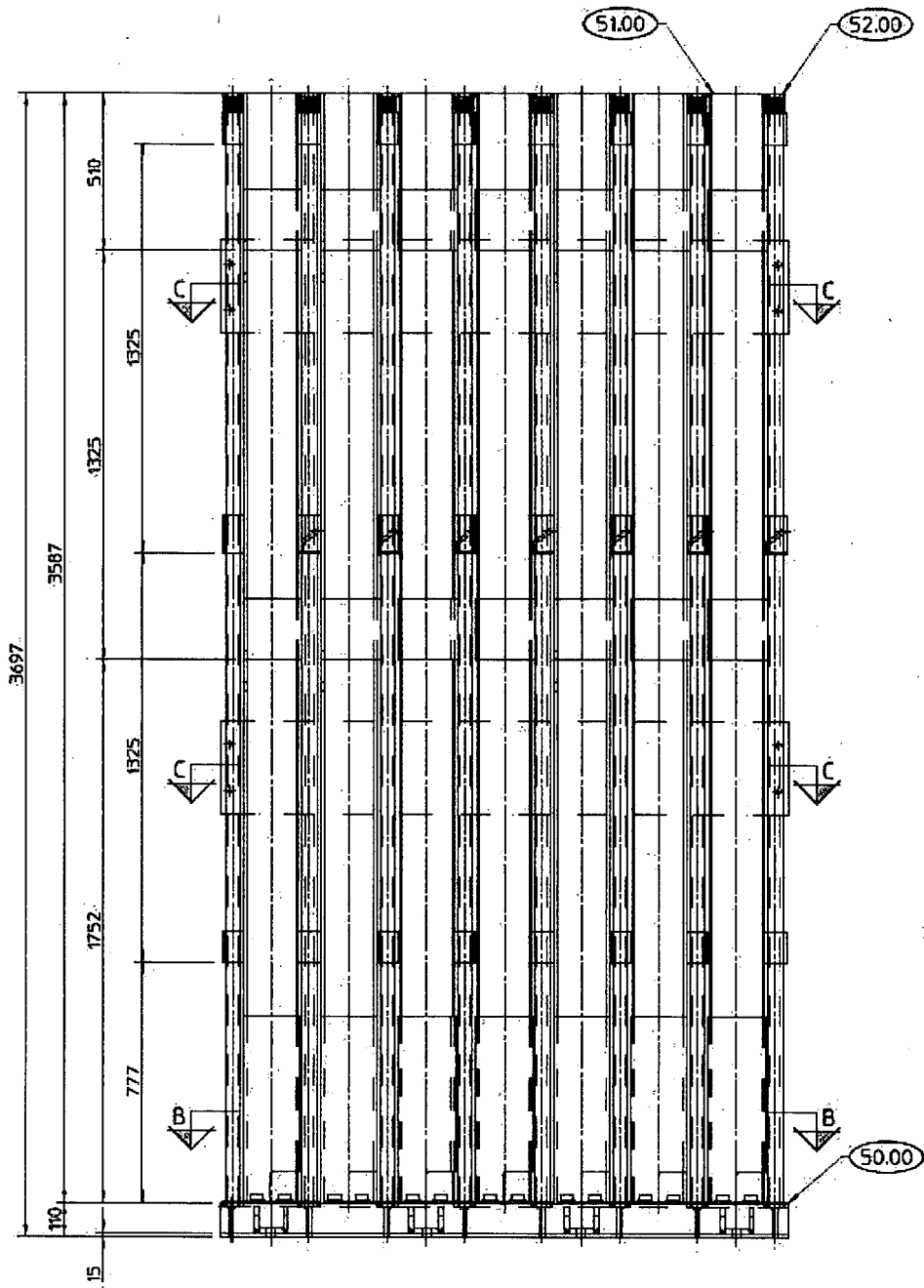


Figure 4-4. Elevation View of the Fresh Fuel Rack

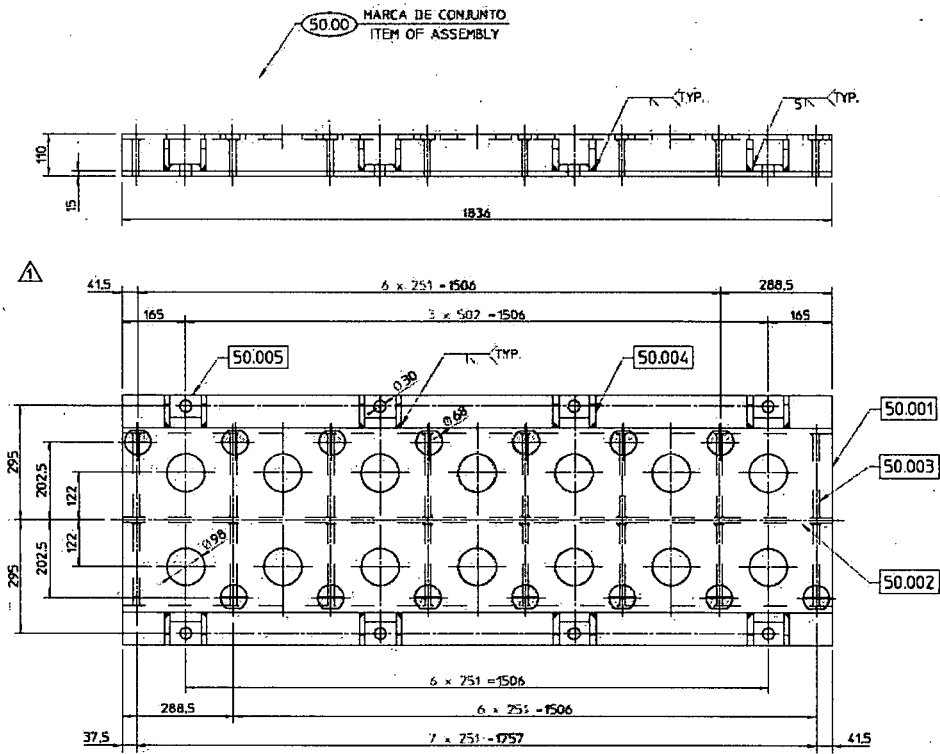


Figure 4-5. Base Plate of the Fresh Fuel Rack

### 4.3 SPENT FUEL RACKS: IMPACTS ON THE BASE PLATE

#### 4.3.1 Introduction

This chapter is dedicated to the numerical analyses of the expected impacts between a dropped fuel element and the base plate of a spent fuel rack. Such impacts would occur if the dropped element managed to enter the storage cell without any direct interaction with its walls.

In all cases, the base plate has been considered to be rigidly fixed at the locations of the supports of the rack. Since the main effect of interest is the load imposed on the support, it is conservative to assume a greater rigidity than the actual case.

The analyses described in this chapter include the cases in which the cell undergoing the impact is located directly above one of the supports and that it is at the maximum distance from all the supports.

The finite element code Abaqus/Explicit (SIMULIA, 2008) has been used for all the numerical calculations.

As mentioned in Section 4.2, it is assumed that both the element and the fuel handling tool fall in water from a height of 1.8 m and that the impact with the base plate takes place with a velocity of 5.68 m/s.

#### 4.3.2 Impact Above a Leg

A finite element model was developed for studying the impacts directly above one of the supports. The model represents the geometry of the base plate and the part of the fuel element which will interact with the base plate. The rest of the fuel element is modelled with bar elements followed by the point mass representing the fuel handling tool. The overall arrangement is presented in Figure 4-6.

For an impact velocity of 5.68 m/s, the resulting history of impact forces appears in Figure 4-7. The initial sustained value is approximately 0.34 MN. The second hump in the force history is associated with the deceleration of the mass of the fuel handling tool, reaches about 0.67 MN.

The plastic deformations of the base plate are considerable, reaching slightly over 0.36, but they remain highly localised as can be seen in Figure 4-8. In any case, this level of plastic strain is well below 0.40, which is the ductility of the material, therefore this interaction is acceptable.

Figure 4-9 shows the velocity histories of the nose, an intermediate point in the element and the fuel handling tool. Both the force and the velocity histories indicate that the impact has finished in about 12 ms.

The same analysis has been repeated without the handling tool. Figure 4-10 shows the history of impact forces, which is similar to that presented in Figure 4-7, except that the hump associated with the arrival of the handling tool is obviously missing.

The plastic deformations that appear in Figure 4-11 are not too different from those caused by the impact with the handling tool. Finally, the velocities of various points along the fuel element are shown in Figure 4-12.

### ***4.3.3 Impact Between Legs***

A similar model to that of the previous section was used here to analyse impacts between the supports of the rack. The new model includes more details of the base plate. The mesh appears in Figure 4-13.

The history of impact forces can be seen in Figure 4-14. The flexibility of the base plate (small but finite) leads to a smoother response than when the base of the cell is rigidly supported. The peak forces are approximately 0.30 MN.

The distribution of the plastic deformations caused by the impact is shown in Figure 4-15. The strains are strongly localised around the orifice and their peak value barely exceeds 0.13, well below the ductility of the material.

Finally, the evolution of the velocities of selected points along the dropped object is presented in Figure 4-16.

The analysis was repeated on the assumption that the element drops without the handling tool. The initial peak impact force is still about 0.30 MN (Figure 4-17), although the force levels at later times are now lower than with the handling tool. The local plastic deformations are limited to 0.11 as can be seen in Figure 4-18. The velocity histories at points of the fuel element appear in Figure 4-19.

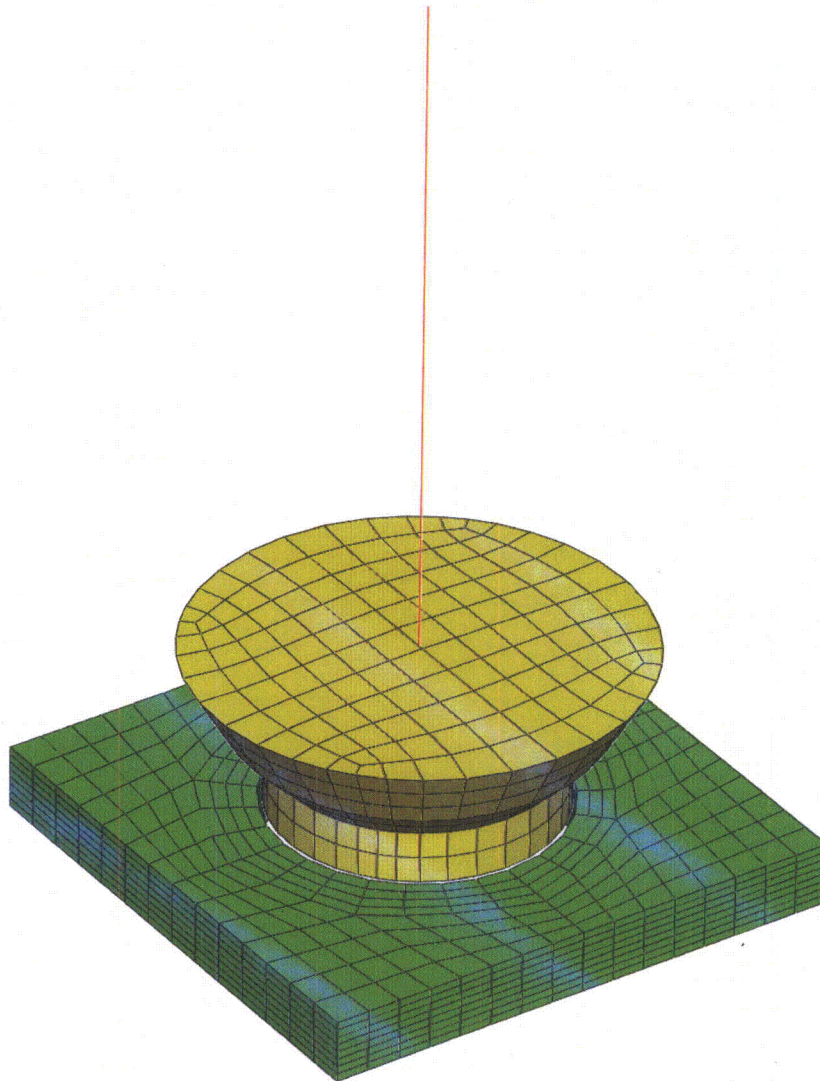


**Figure 4-6. Spent Fuel, Above Leg. View of the Mesh**

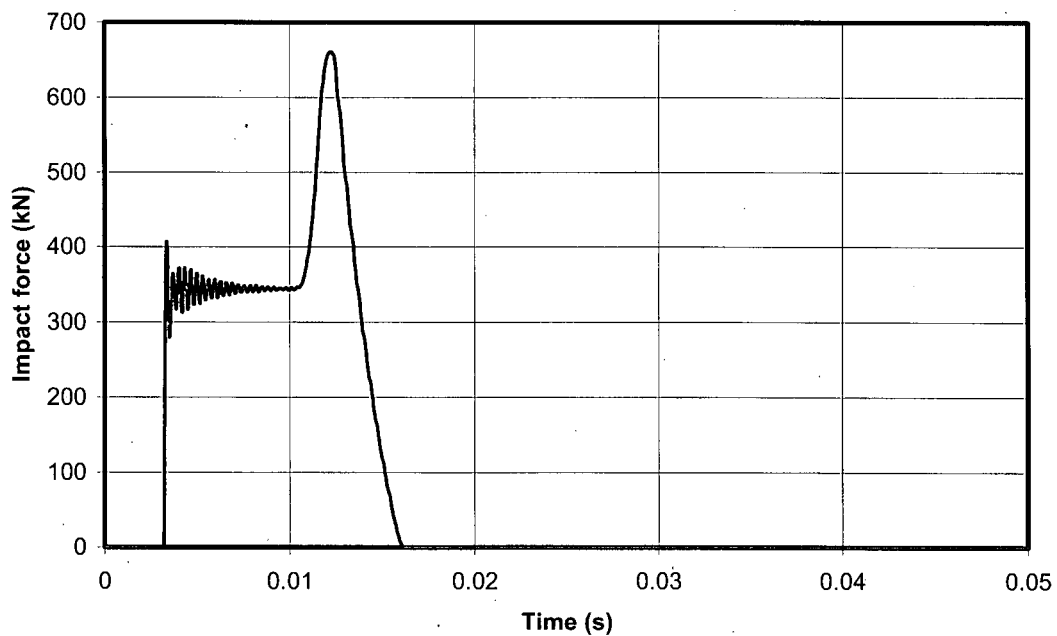


**Figure 4-7. Spent Fuel, Above Leg with Tool. Impact Forces**

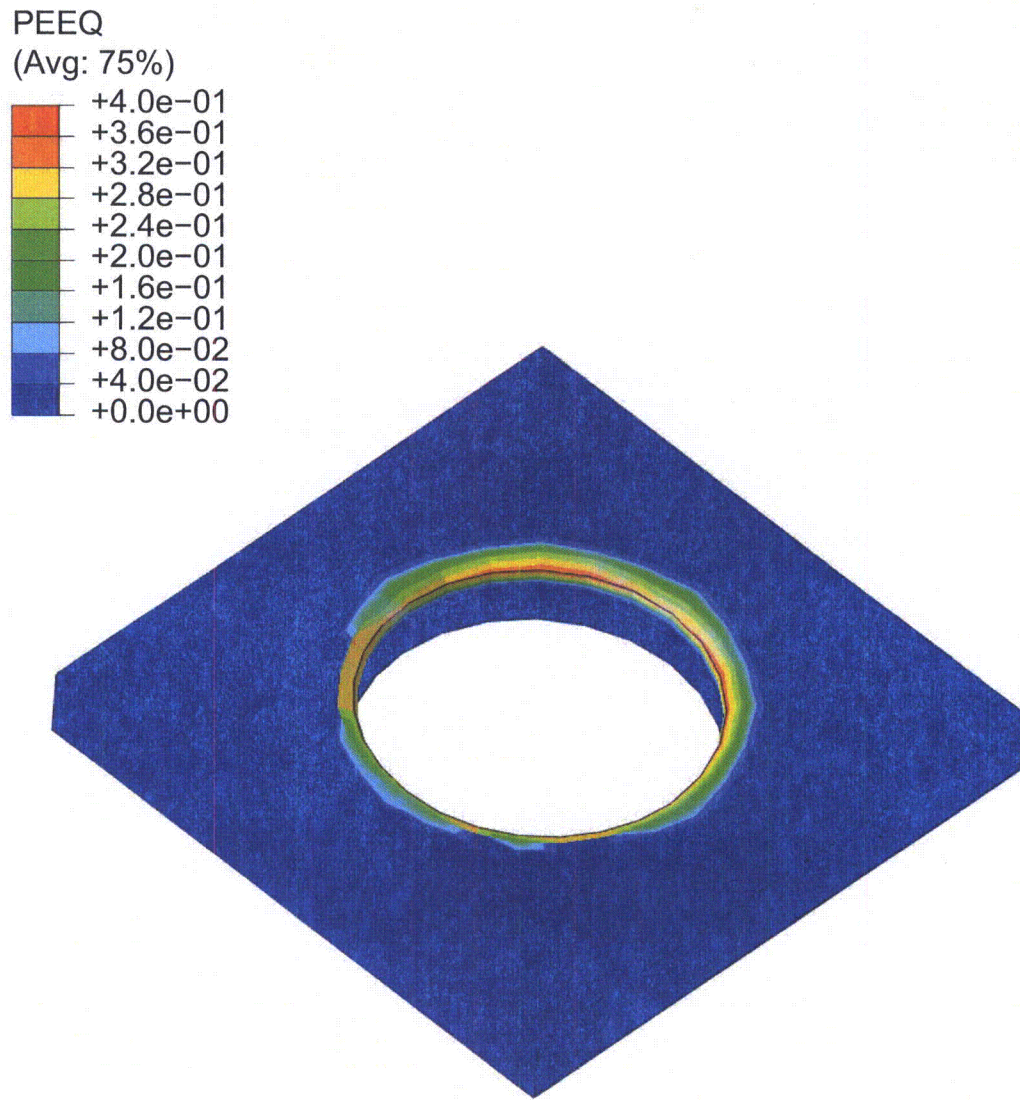


Figure 4-8. Spent Fuel, Above Leg, with Tool. Plastic Deformations

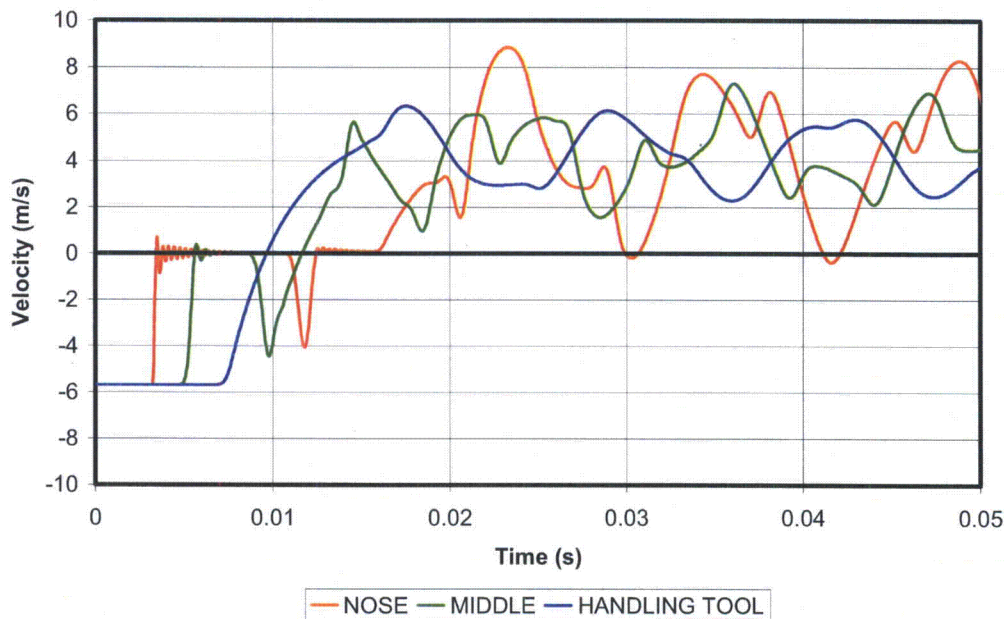
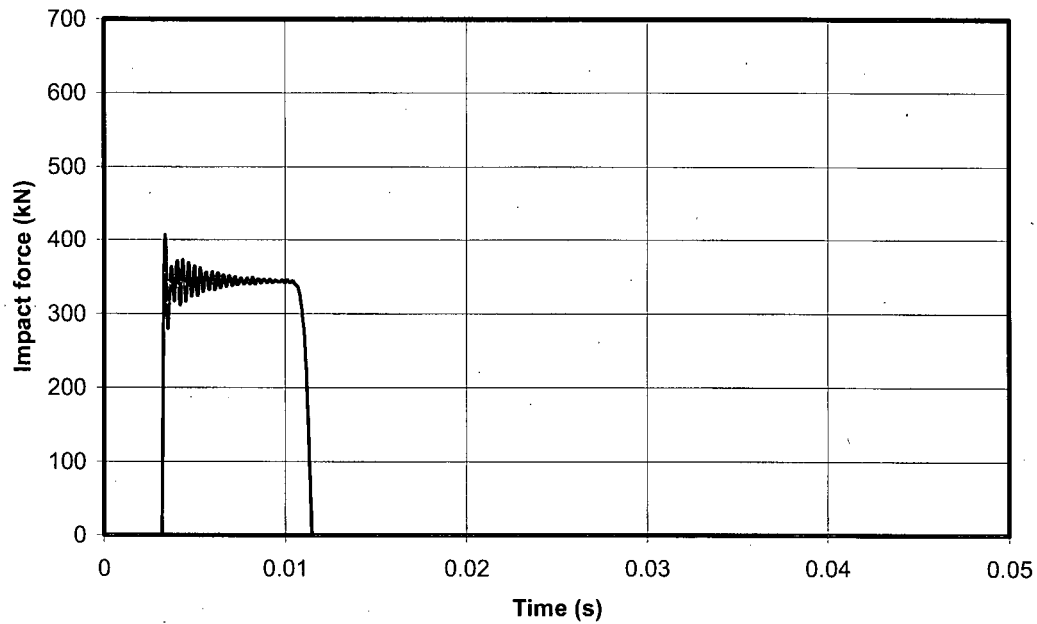
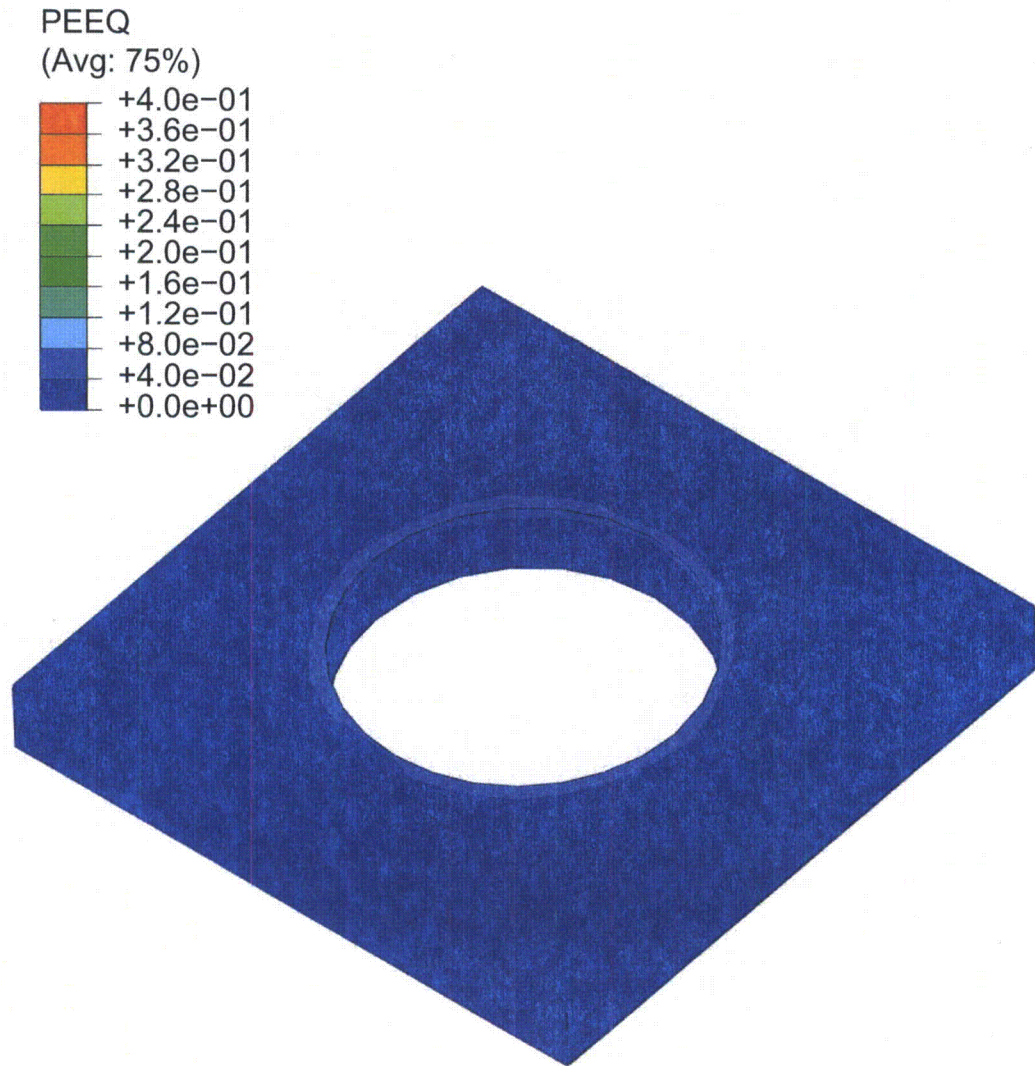


Figure 4-9. Spent Fuel, Above Leg, with Tool. Fuel Velocities



**Figure 4-10. Spent Fuel, Above Leg, without Tool. Impact Forces**



**Figure 4-11. Spent Fuel, Above Leg, without Tool. Plastic Deformations**

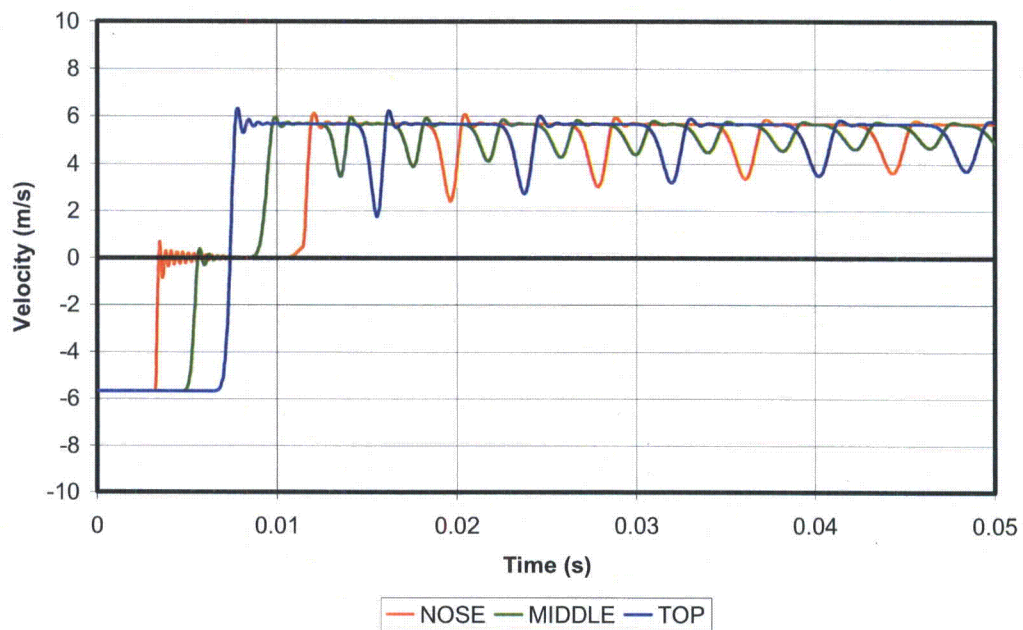
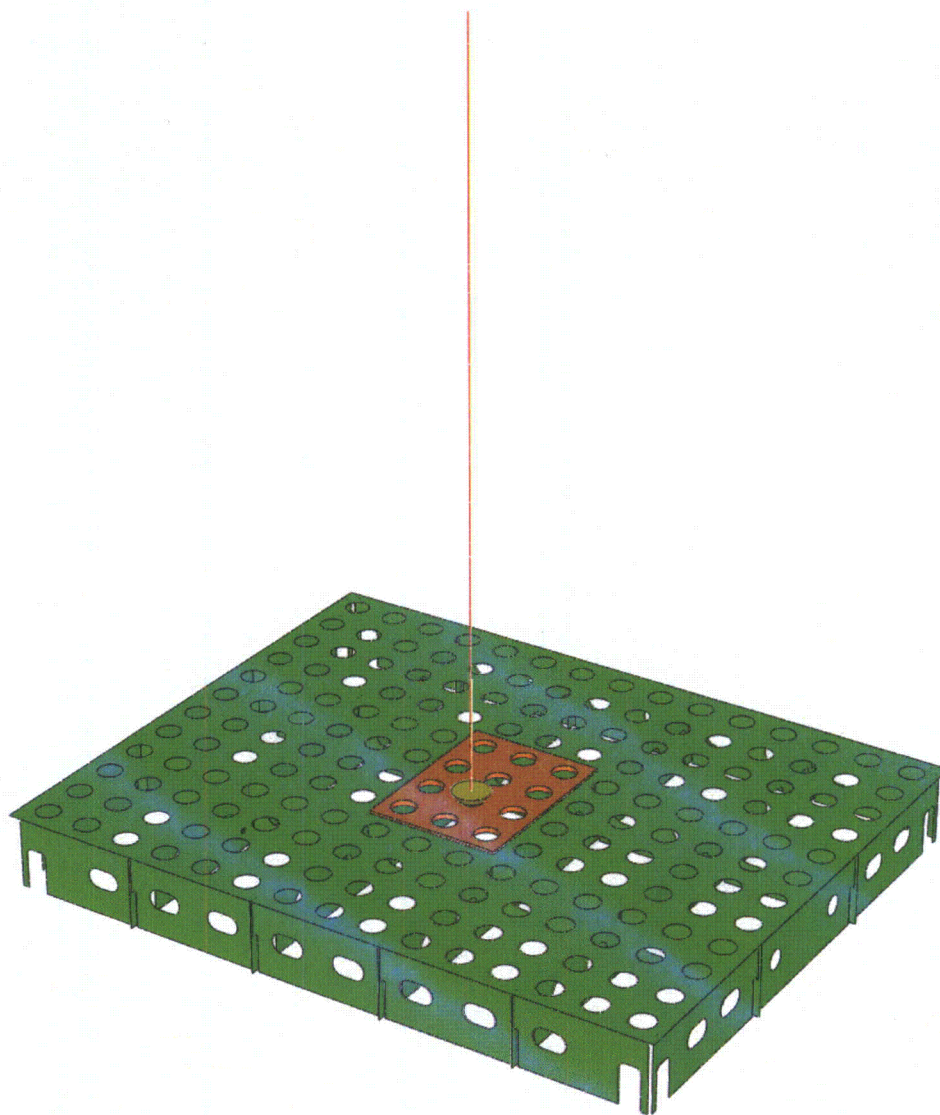
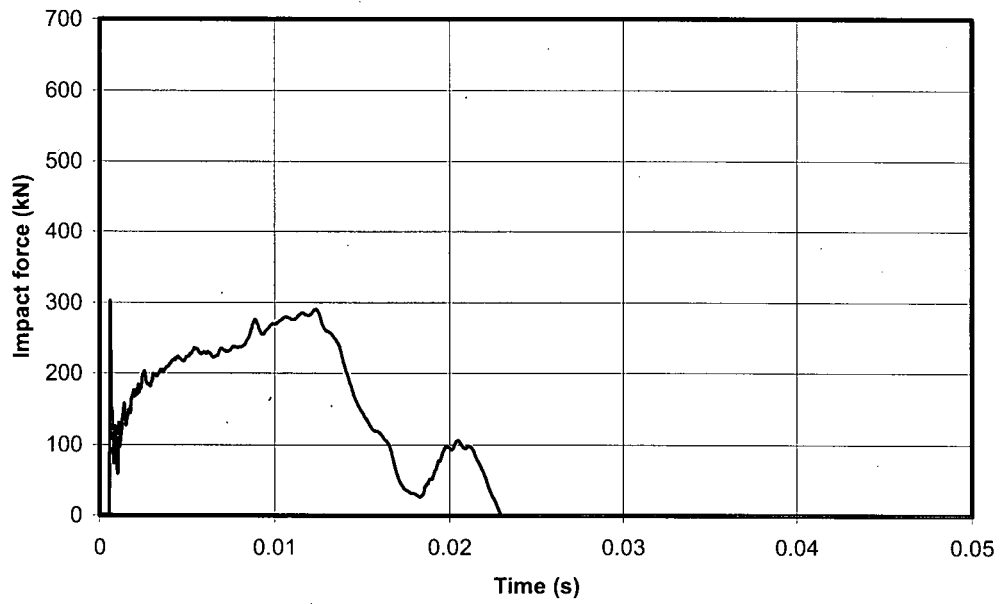


Figure 4-12. Spent Fuel, Above Leg, without Tool. Fuel Velocities



**Figure 4-13. Spent Fuel, Between Legs. View of the Mesh**



**Figure 4-14. Spent Fuel, Between Legs, with Tool. Impact Forces**

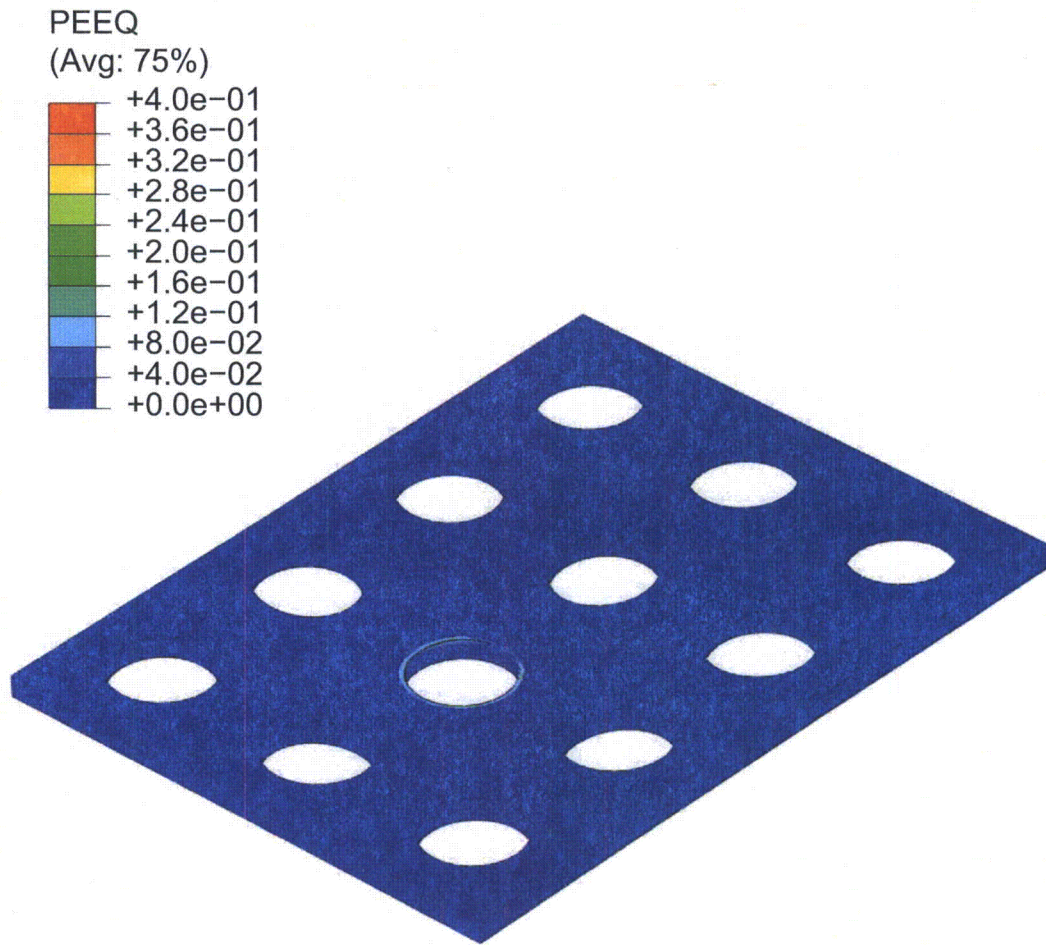


Figure 4-15. Spent Fuel, Between Legs, with Tool. Plastic Deformations

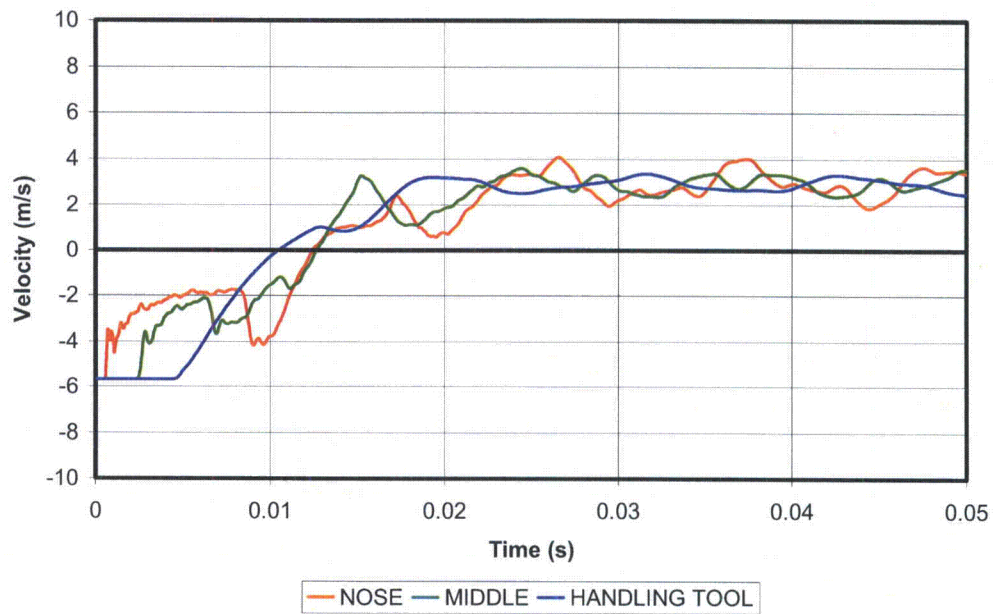
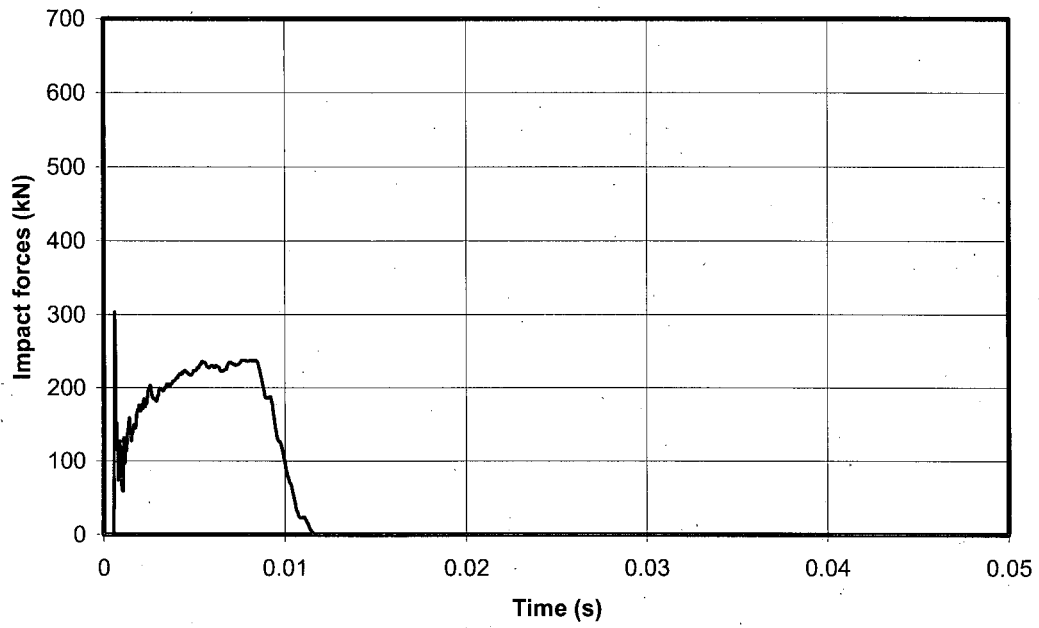
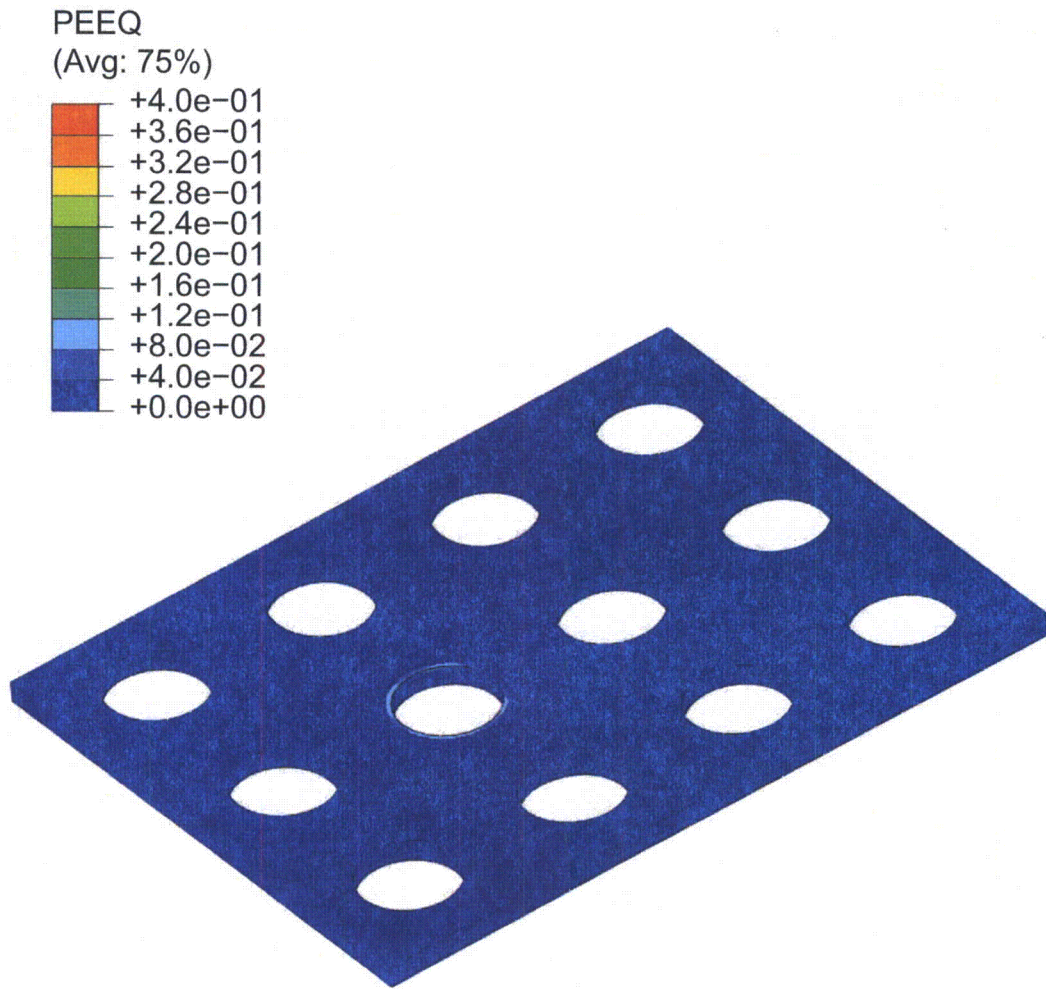


Figure 4-16. Spent Fuel, Between Legs, with Tool. Fuel Velocities



**Figure 4-17. Spent Fuel, Between Legs, without Tool. Impact Forces**



**Figure 4-18. Spent Fuel, Between Legs, without Tool. Plastic Deformations**

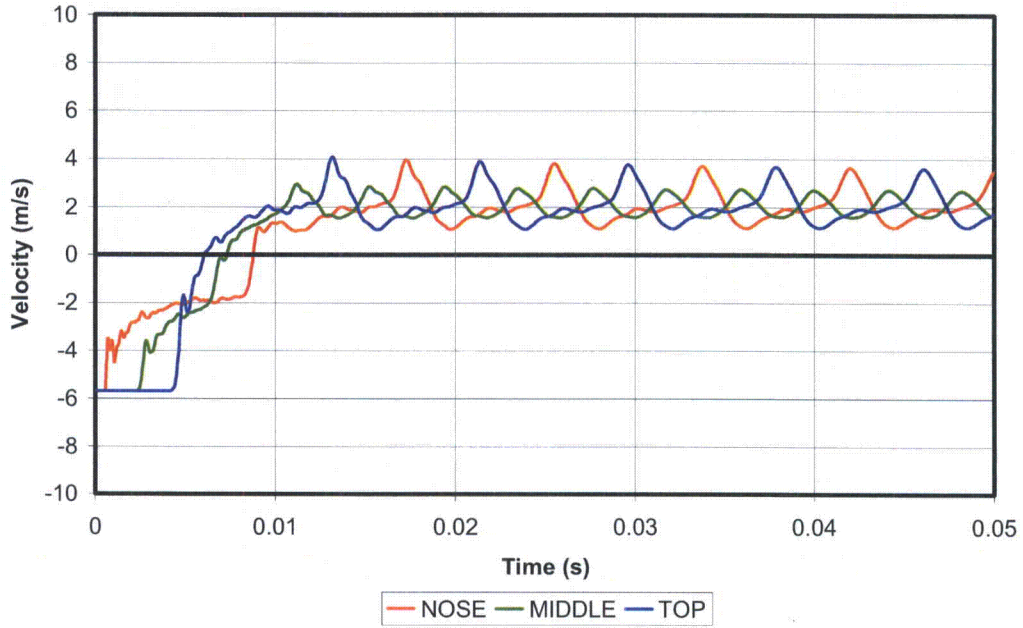


Figure 4-19. Spent Fuel, Between Legs, without Tool. Fuel Velocities

## 4.4 SPENT FUEL RACKS: IMPACTS AT THE TOP OF THE CELLS

### 4.4.1 Introduction

This chapter studies the cases in which the dropped fuel element impacts the top of the cell walls rather than entering the cell. At the point of impacting the upper edge of the walls, the falling element has a velocity of 7.82 m/s, following the drop from 6.4 m in water.

Both vertical and inclined attitudes of the dropped fuel element should be considered. Nevertheless, it should be noticed that the kinetic energy which is effective for inducing deformations in the missile or target is maximised when the centre of gravity of the missile and the centre of the contact area are aligned with the missile velocity. Otherwise, the impact results in part of the translational kinetic energy of the missile being converted into rotational kinetic energy; that part of the kinetic energy is preserved and not used for producing deformations.

In the present case, the center of gravity of the fuel element will be aligned with the impact point only when the fuel element falls with a vertical attitude or when the fuel element has a very small inclination (less than 2°) with respect to the vertical. The deviation from verticality in the latter case is so small as to make it unnecessary to repeat the analyses with that inclination. Any other angle of inclination would result in a reduction of the kinetic energy available for producing deformations.

As a consequence, it is concluded that only the vertical attitude should be considered for the study of dropped fuel elements impacting the top of the cell walls.

Three different impacts must be studied, which will be the object of the following sections. In each case, it will be considered that the fuel element may drop with or without the handling tool. The three impacts are:

- Impact on a wall slotted in its upper part
- Impact on a wall slotted in its lower part
- Impact at the intersection between two walls

### 4.4.2 Impacts on Cell Walls

The first impact considered is that in which the dropped element falls on the center of one of the cell walls. This impact against the cell wall is softer than against the base plate, because the impact is now more energetic and the structure is more susceptible to damage at the top of the rack. Hence, the impact duration can be expected to lengthen and the forces developed will be correspondingly smaller.

The present impacts are negligible from the viewpoint of the demands imposed on the supports. The reason for conducting the analyses is to assess the damage caused on the cell structure.

#### 4.4.2.1 Walls Slotted Below

The upper structural steel plates are slotted, some in their upper region and some in their lower region. This creates two different types of impacts on cell walls, depending on whether the impacted wall is slotted above or below. Impacts on walls slotted below will be considered first.

A considerable portion of the rack, spanning 4 x 4 cells, has been modelled using shell elements (see Figure 4-20). This type of representation is adequate for any deformation mechanisms that trigger primarily local effects. Lateral boundaries are sufficiently spaced that they do not influence the analysis of local effects. The nodes at the bottom of the model are considered to be fixed.

Assuming that the fuel element falls together with the handling tool, Figure 4-21 presents the history of forces developed between the fuel element and the cell wall. There is an initial peak at approximately 0.35 MN, after which the impact force averages approximately 0.20 MN. The dropped fuel element and handling tool are arrested in about 25 ms; over that time, the element has crushed slightly over 7 cm of the upper region of the cell wall, as indicated by the history of displacements of the nose of the fuel element (Figure 4-22).

The deformations caused by the impact can be seen in Figure 4-23, which confirms the very local character of the effects of the impact and the fact that neighboring cells remain unaffected in spite of the severe distortions and minor tearing caused on the impacted wall.

If the fuel element drops without the handling tool, the first part of the history of forces changes little but the second part, which previously corresponded to the arrival of the handling tool, is now considerably reduced (Figure 4-24). This reduction is also reflected by the displacements shown in Figure 4-25, which indicate that only the upper 4 cm at the top of the wall are now crushed. The deformations caused are presented in Figure 4-26.

A difference between the impacts on walls slotted above and below is that, if the wall was slotted below, the impacted plate must displace with it all the structural steel plates located immediately below and running transversely to it. This provides for a fairly wide distribution of the forces transmitted to the weaker and thinner borated steel located at lower levels. The analysis is therefore conservative with respect to those effects, which are not of a purely local nature and which would span 12 or 15 cells rather than the 4 represented in the model.

#### 4.4.2.2 Walls Slotted Above

As in the previous case, a mesh was generated to support the analyses; the numerical model can be seen in Figure 4-27.

Again on the assumption that the handling tool drops with the fuel element, the history of impact forces (Figure 4-28) is now longer than that obtained in the previous section, even though the initial peak changes little. About 50 ms are now necessary to arrest the element and the handling tool.

The displacements achieved by the dropped element grow to approximately 20 cm as can be observed in Figure 4-29. Figure 4-30 presents the deformations induced and the plastic strains induced by the impact, which provide the explanation for the previous observations: the

impacted wall, slotted in its upper part, bends out of the way, thus giving rise to a much softer response on the target.

Similar results are produced when the fuel element drops without the handling tool. The first peak in the force history (Figure 4-31) remains unchanged, although the second part of the history reflects the absence of the handling tool. The peak displacements decrease to about 10 cm (Figure 4-32), but the response mechanism is still that of wall bending, as shown by the deformations presented in Figure 4-33.

#### **4.4.3 Impacts on Cell Contacts**

Impacts on the intersection of the walls of neighboring cells have also been analyzed for the sake of completeness. In this case, the fuel element is dropped with its axis coinciding with the contact between the intersecting walls of the cells.

The mesh for studying the problem was constructed as in the previous analyses and is presented in Figure 4-34.

For an element dropped together with the handling tool, the history of impact forces is shown in Figure 4-35. The displacements caused appear in Figure 4-36, peaking at about 3 cm, and the deformations are presented in Figure 4-37. The response of the rack is much stiffer than during impacts on single walls.

When the analysis is repeated without the handling tool, the target is sufficiently strong to generate an essentially elastic response. This is particularly clear in the force and displacement histories (Figures 4-38 and 4-39). Consistently with this, the plastic deformations induced are practically negligible, as evinced in Figure 4-40.

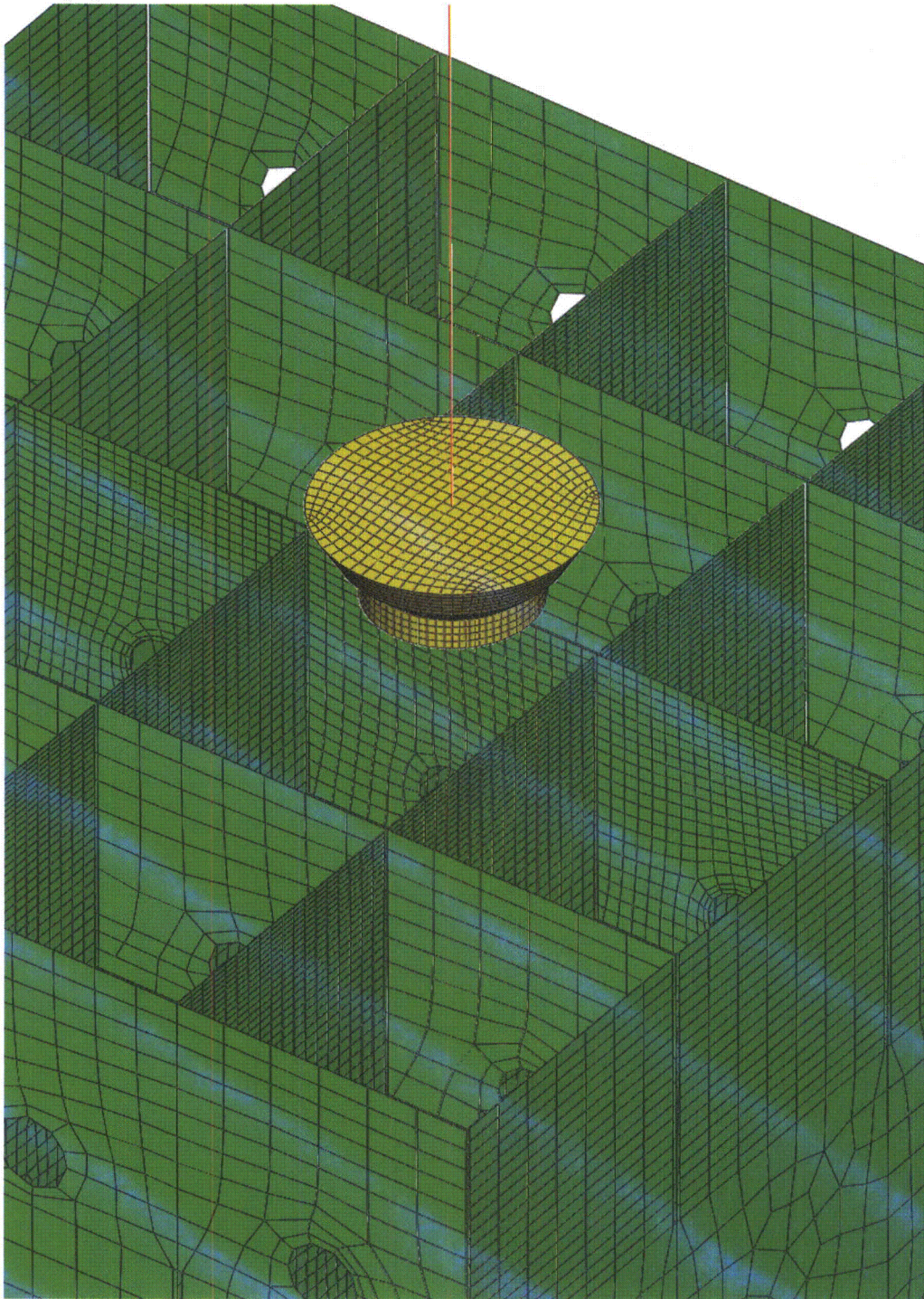


**Figure 4-20. Spent Fuel, Slots Below. View of the Mesh**

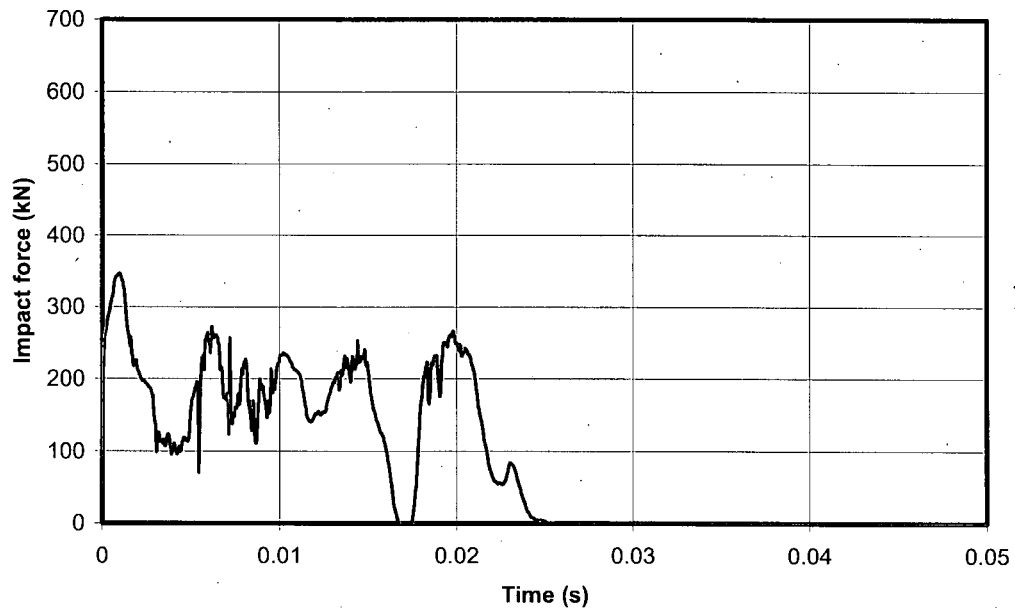


**Figure 4-21. Spent Fuel, Slots Below, with Tool. Impact Forces**

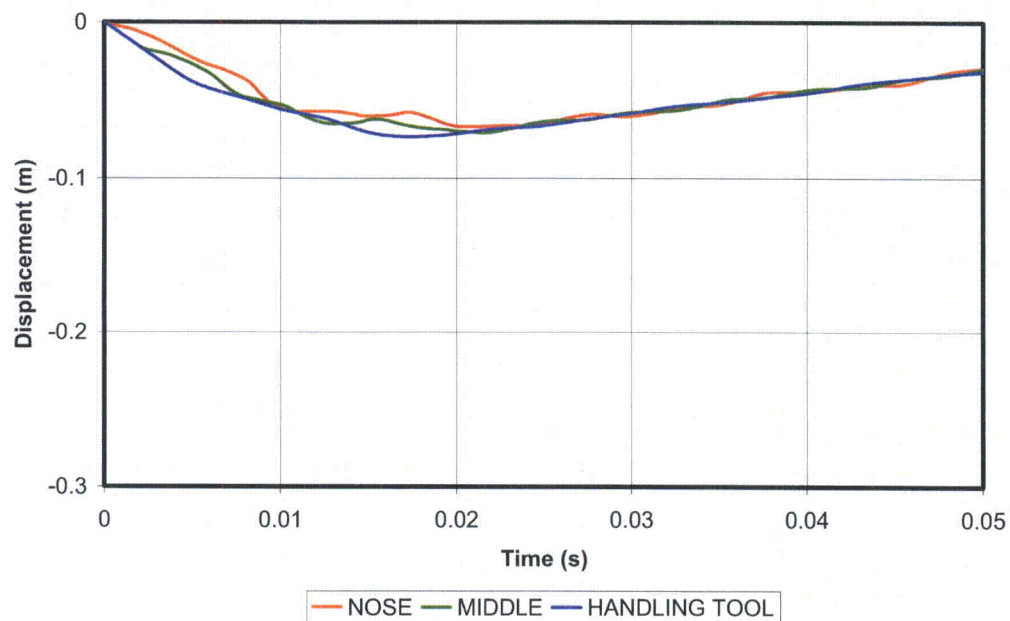


Figure 4-22. Spent Fuel, Slots Below, with Tool. Fuel Displacements

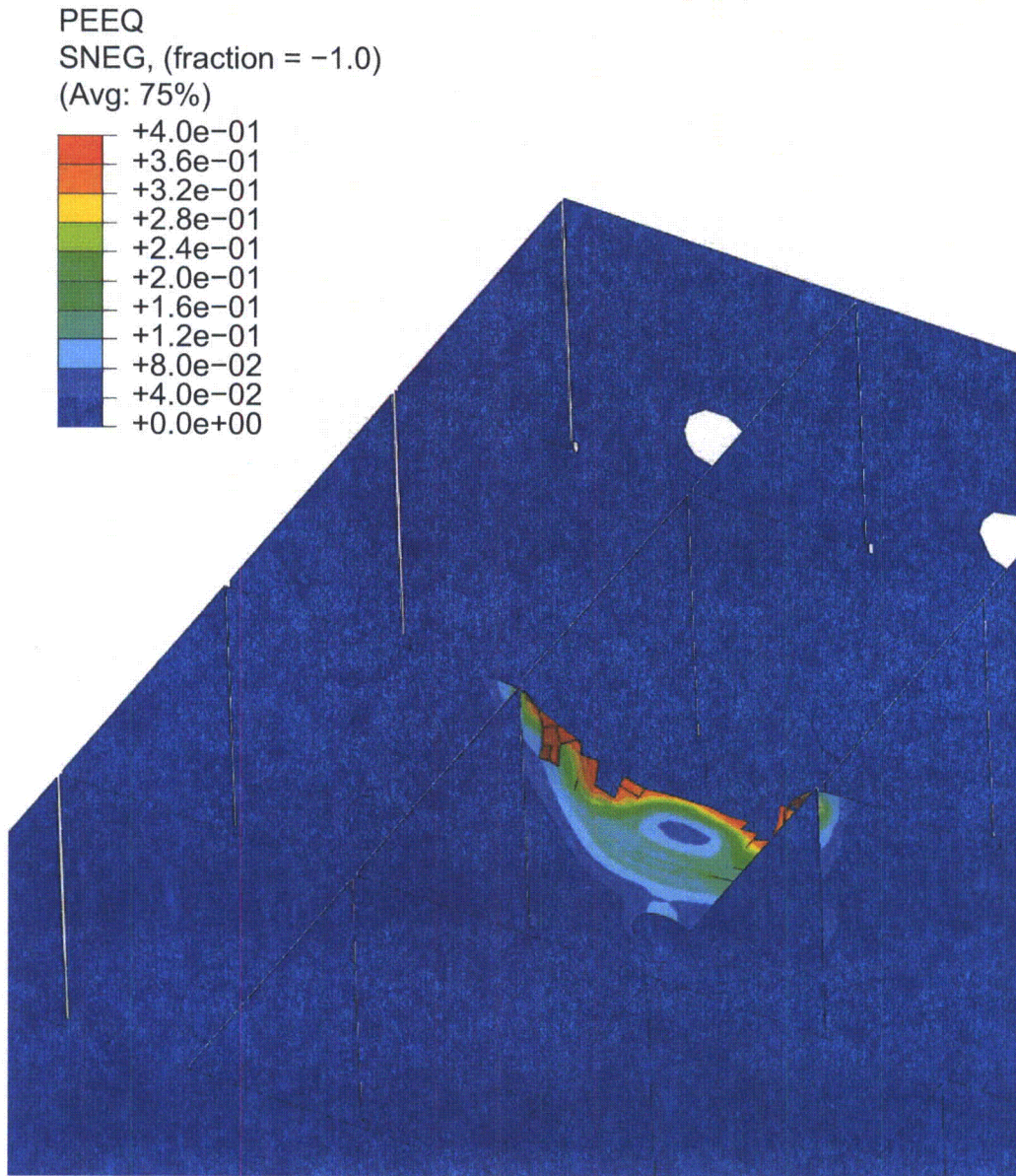
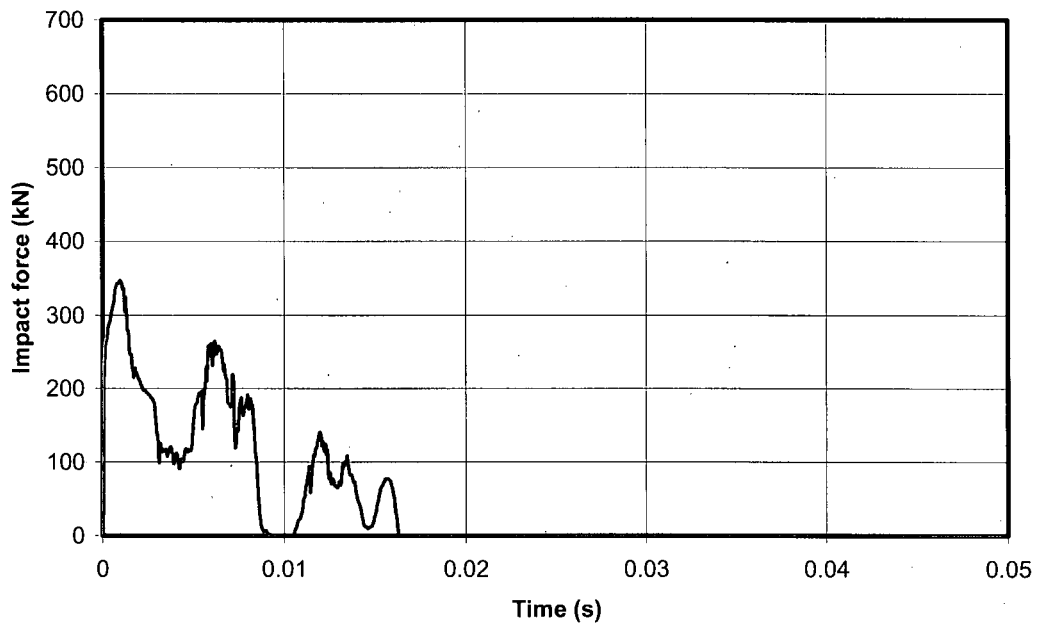


Figure 4-23. Spent Fuel, Slots Below, with Tool. Plastic Deformations



**Figure 4-24. Spent Fuel, Slots Below, without Tool. Impact Forces**

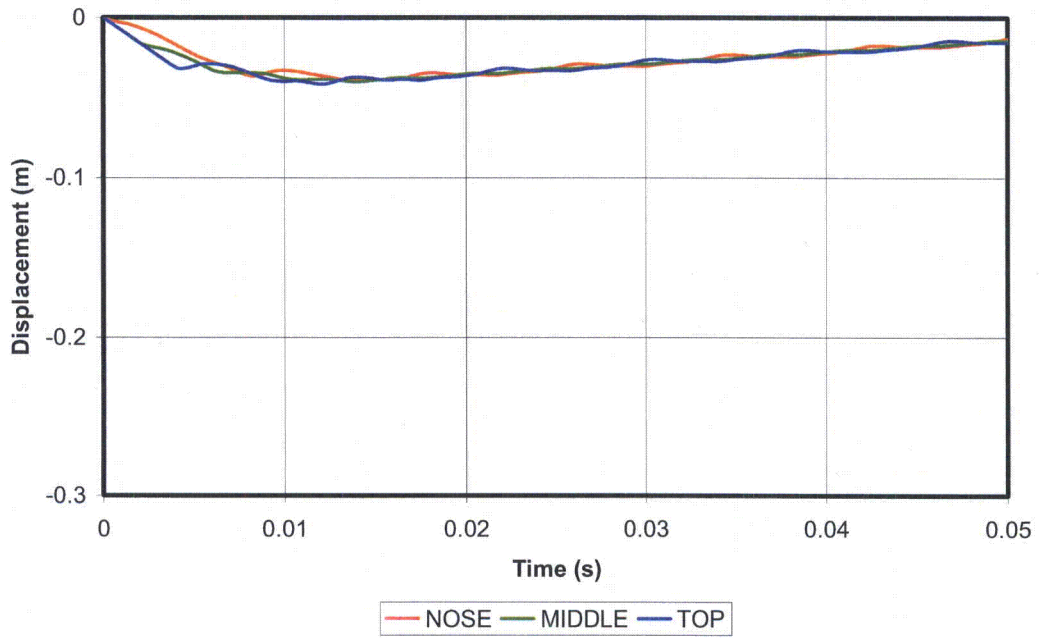


Figure 4-25. Spent Fuel, Slots Below, without Tool. Fuel Displacements

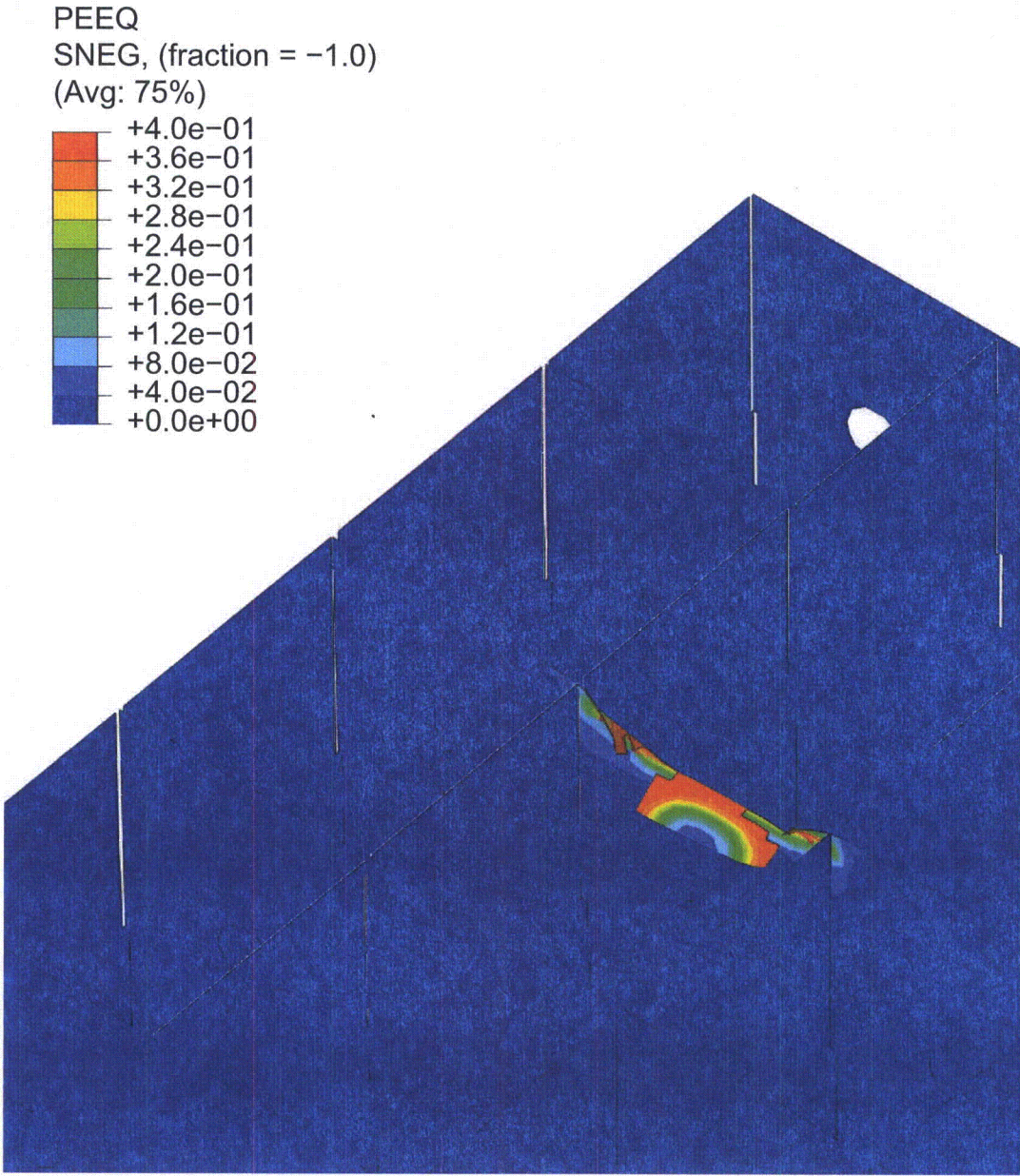


Figure 4-26. Spent Fuel, Slots Below, without Tool. Plastic Deformations

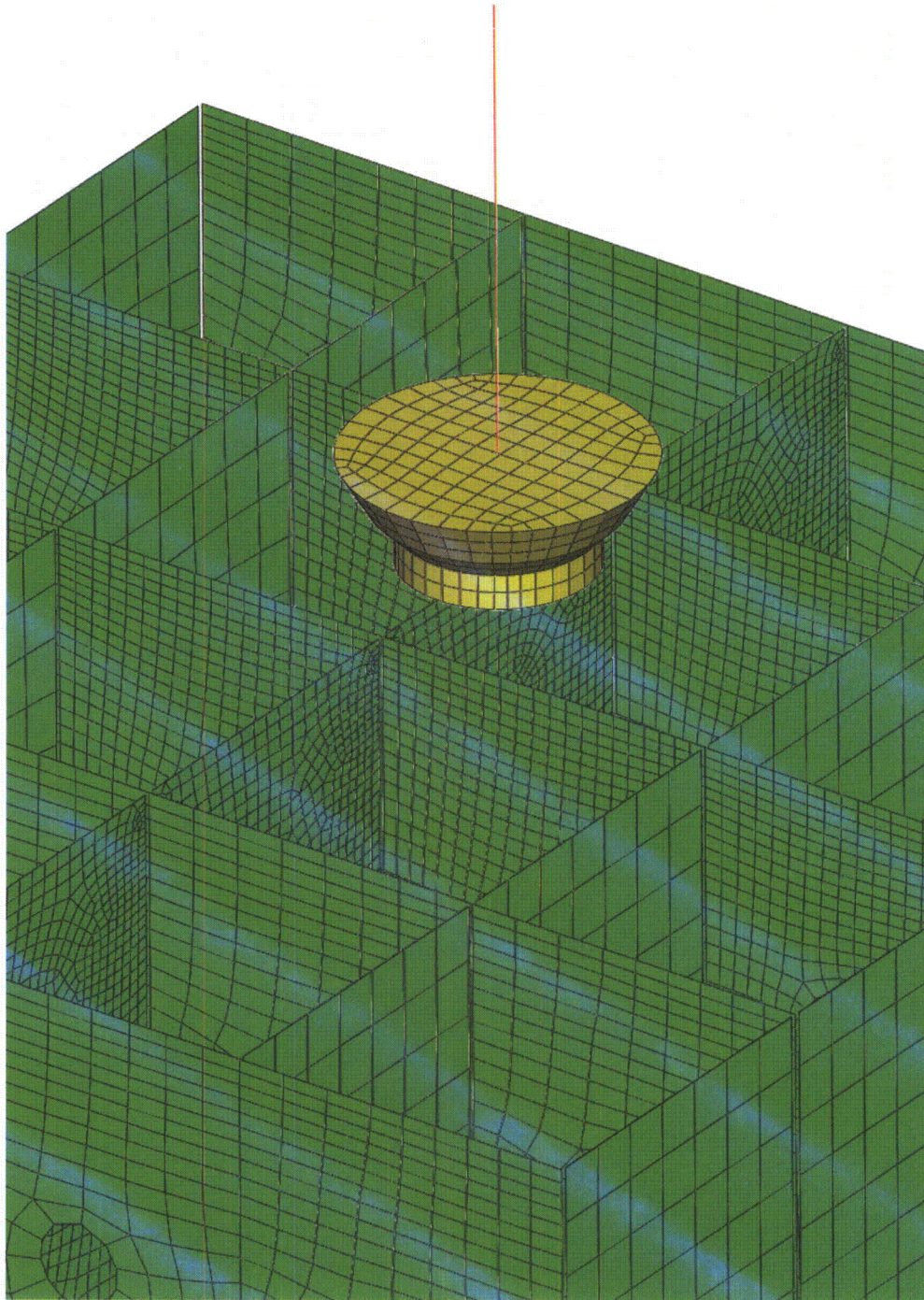
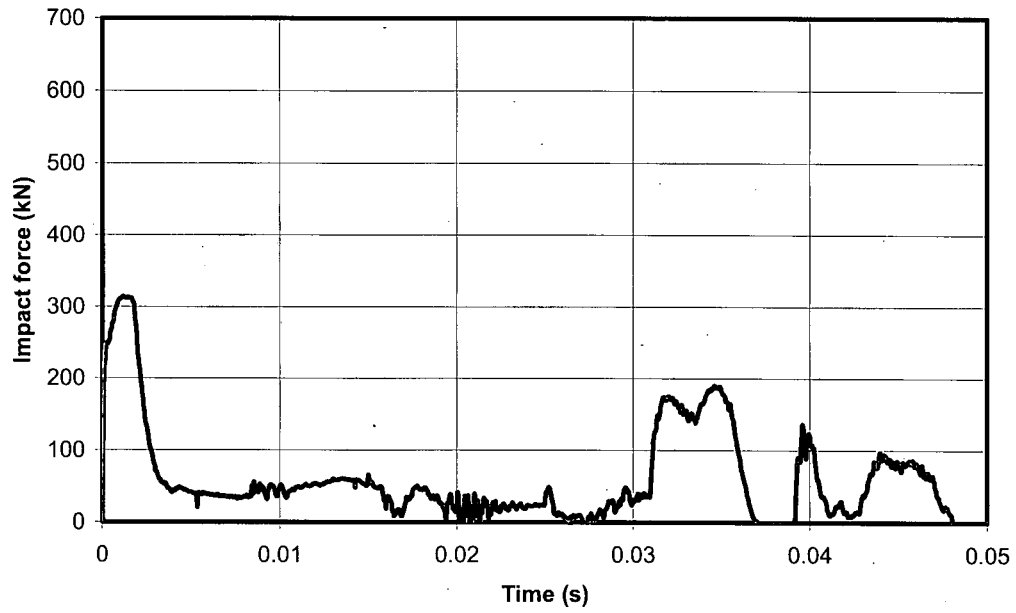


Figure 4-27. Spent Fuel, Slots Above. View of the Mesh



**Figure 4-28. Spent Fuel, Slots Above, with Tool. Impact Forces**

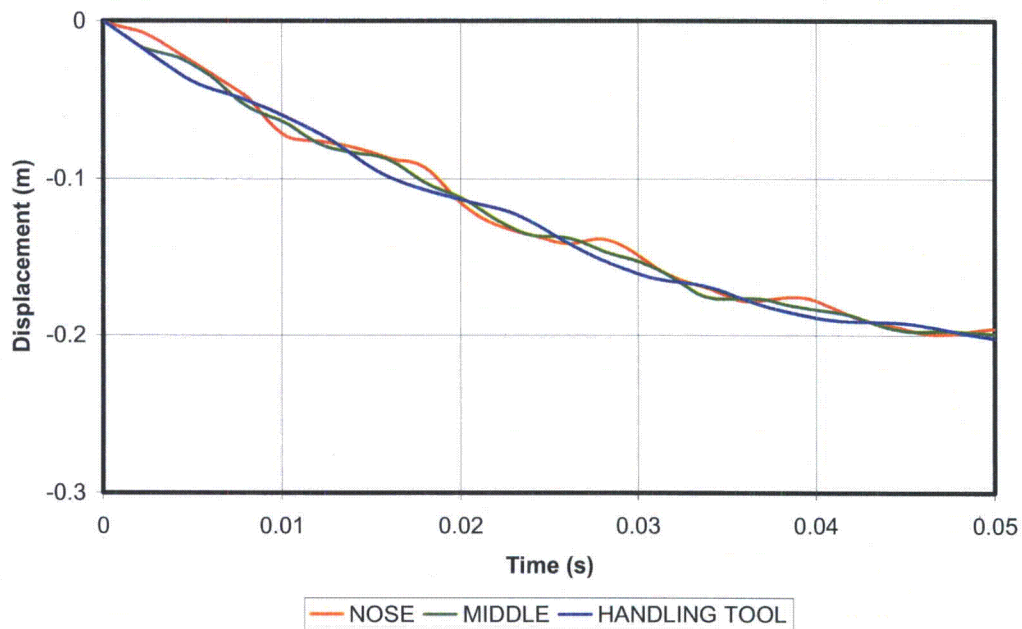


Figure 4-29. Spent Fuel, Slots Above, with Tool. Fuel Displacements

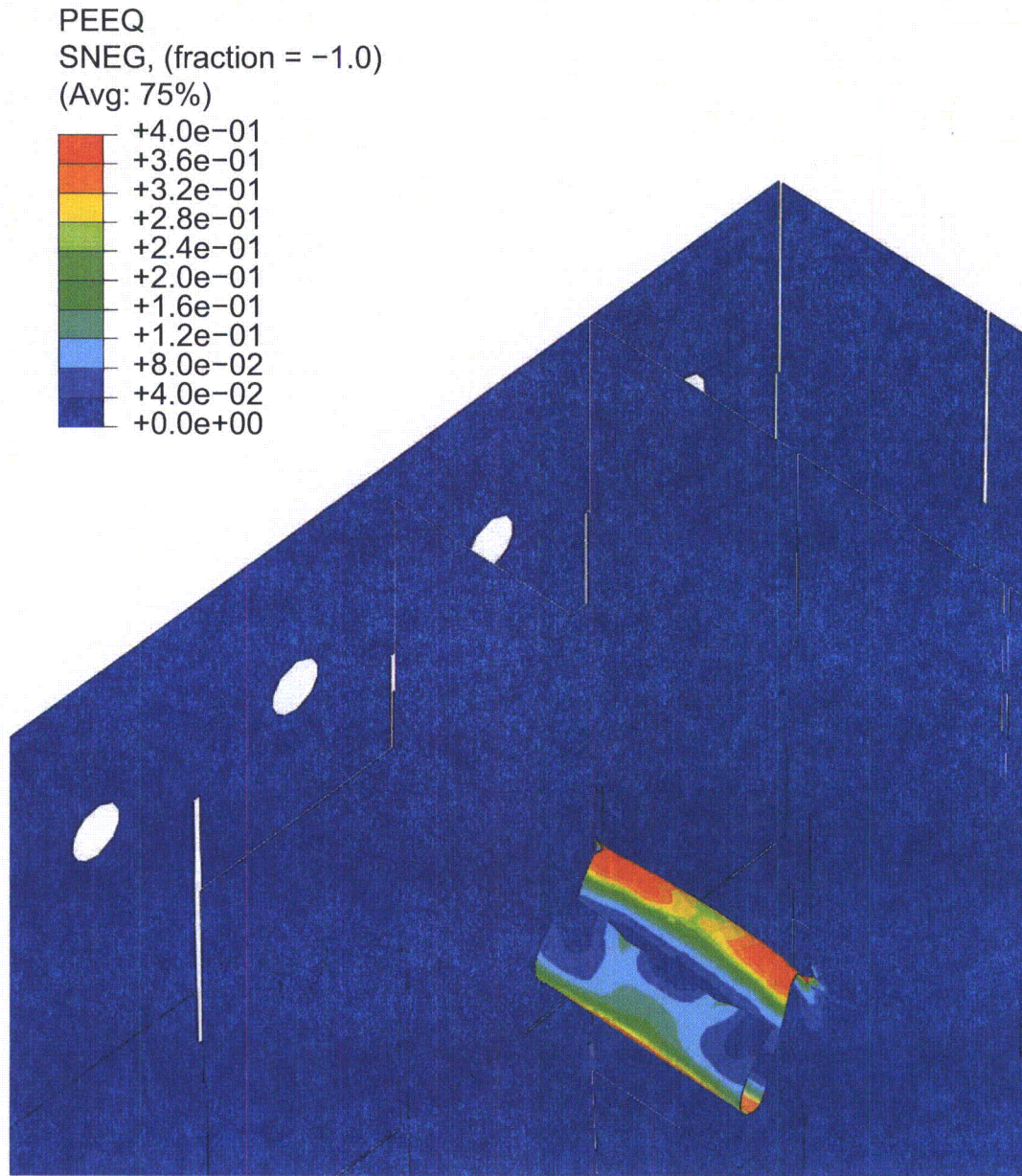
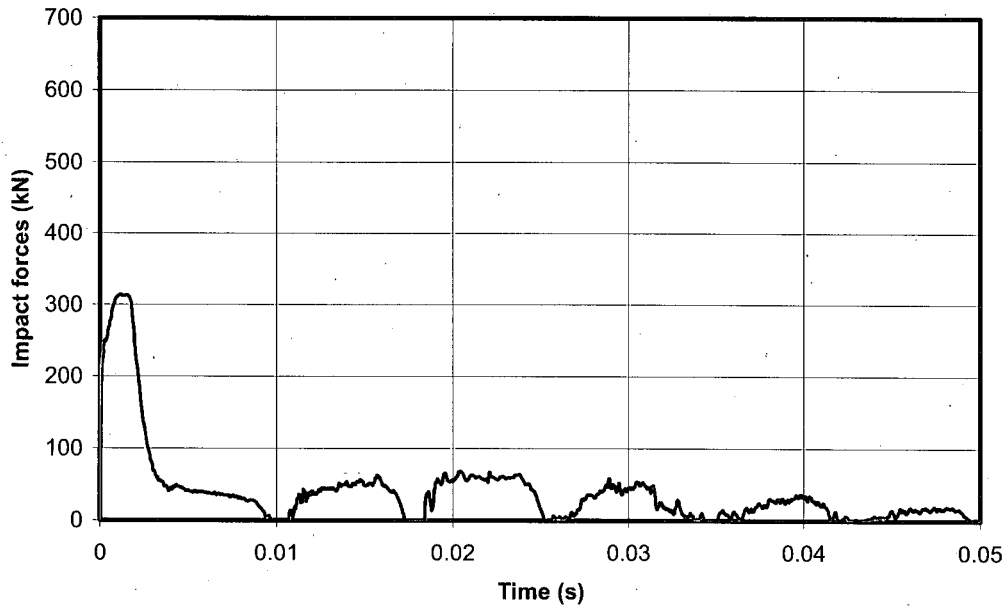


Figure 4-30. Spent Fuel, Slots Above, with Tool. Plastic Deformations



**Figure 4-31. Spent Fuel Slots Above, without Tool. Impact Forces**

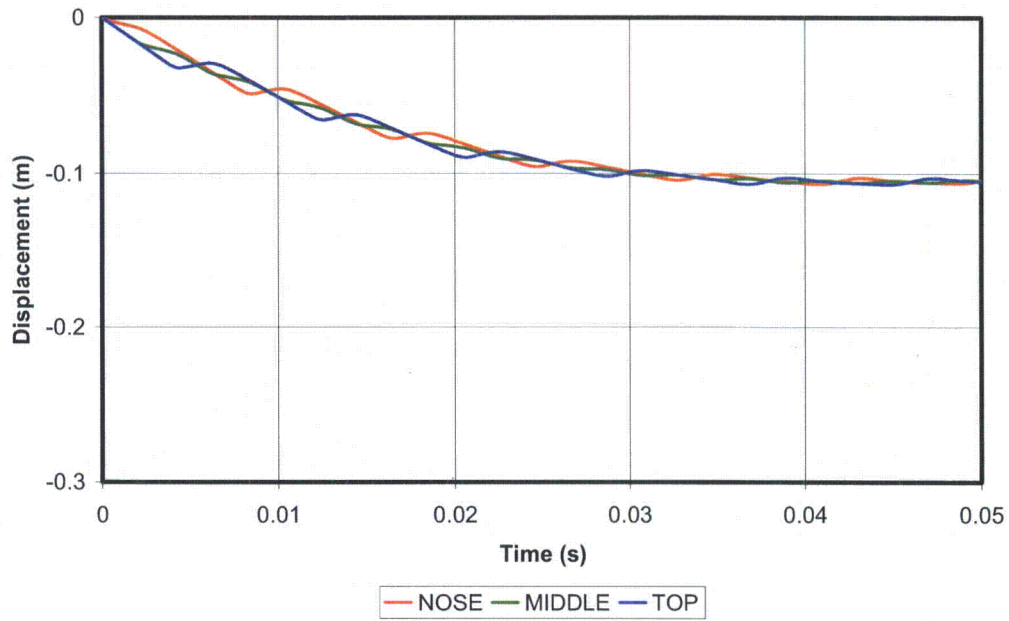


Figure 4-32. Spent Fuel, Slots Above, without Tool. Fuel Displacements

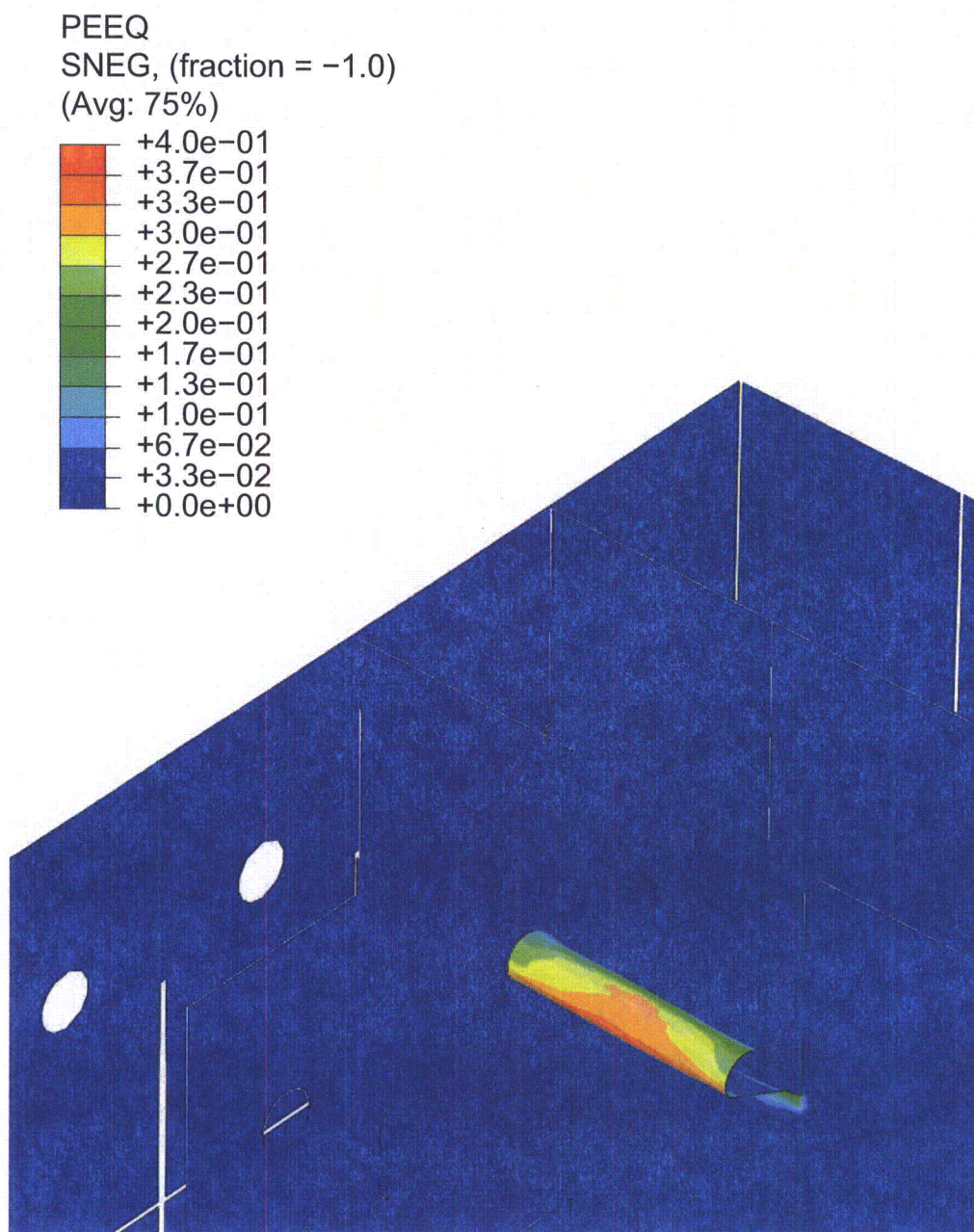


Figure 4-33. Spent Fuel, Slots Above, without Tool. Plastic Deformations

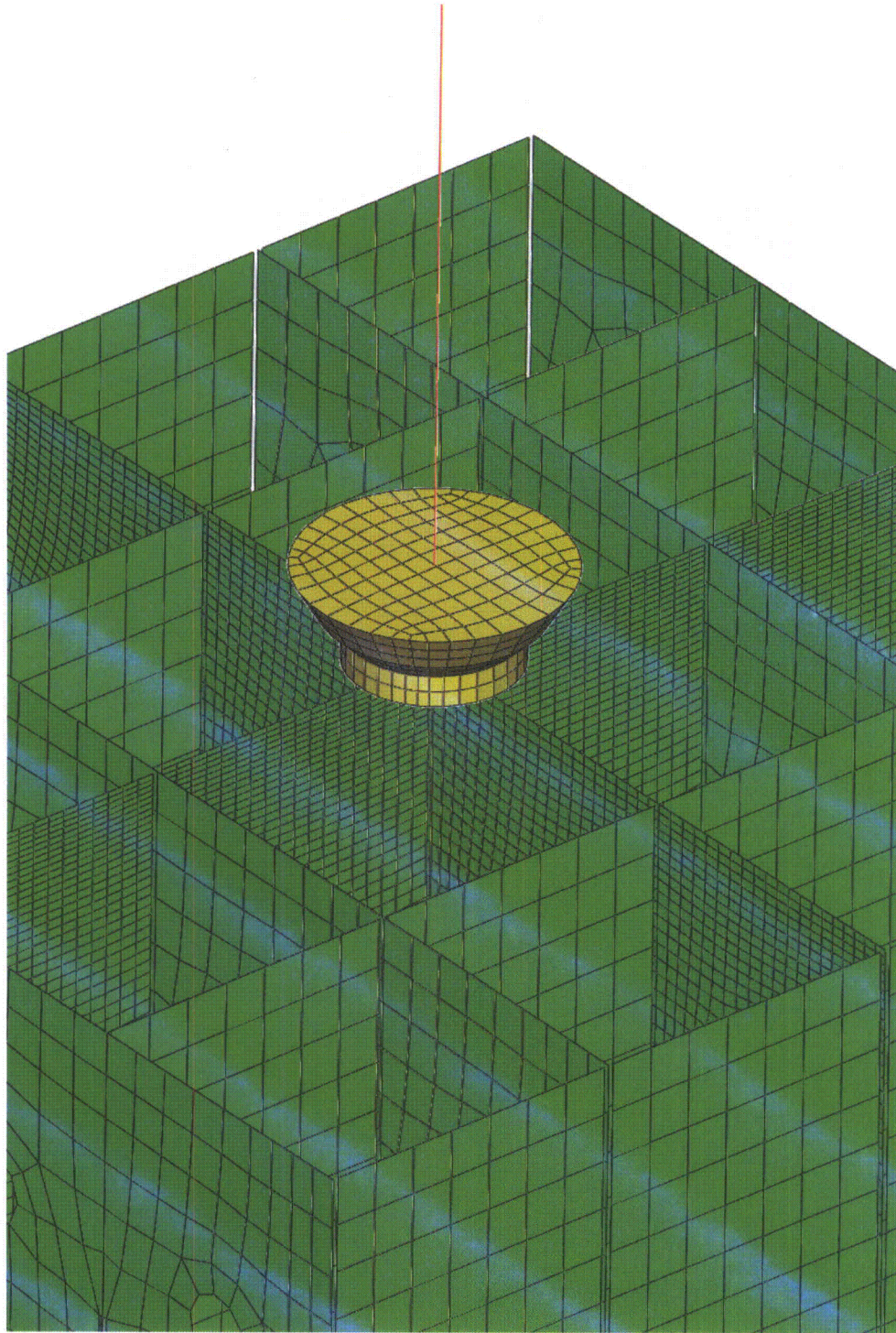
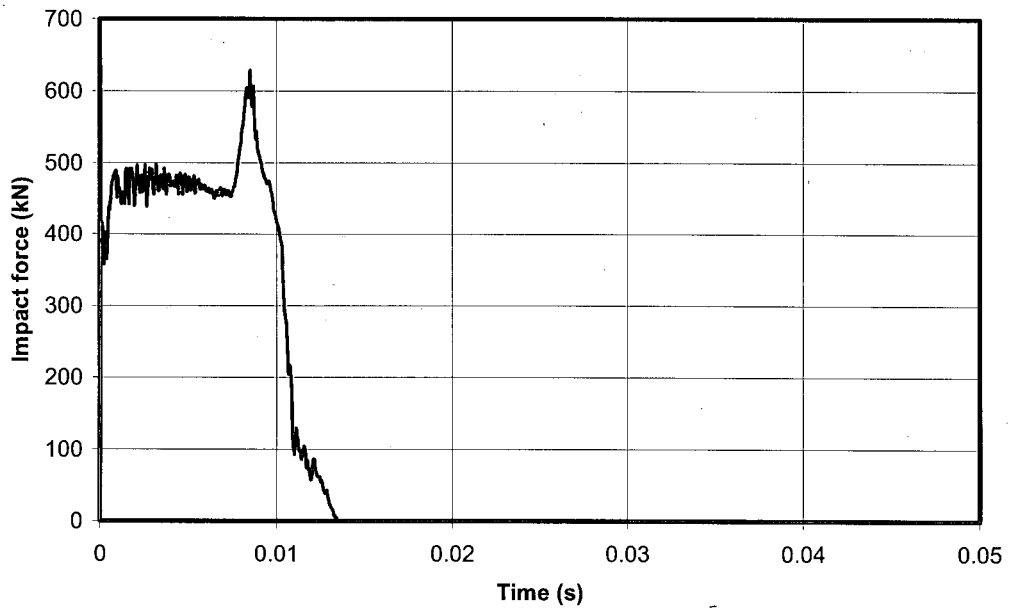


Figure 4-34. Spent Fuel, Intersection. View of the Mesh



**Figure 4-35. Spent Fuel, Intersection. Impact Force**

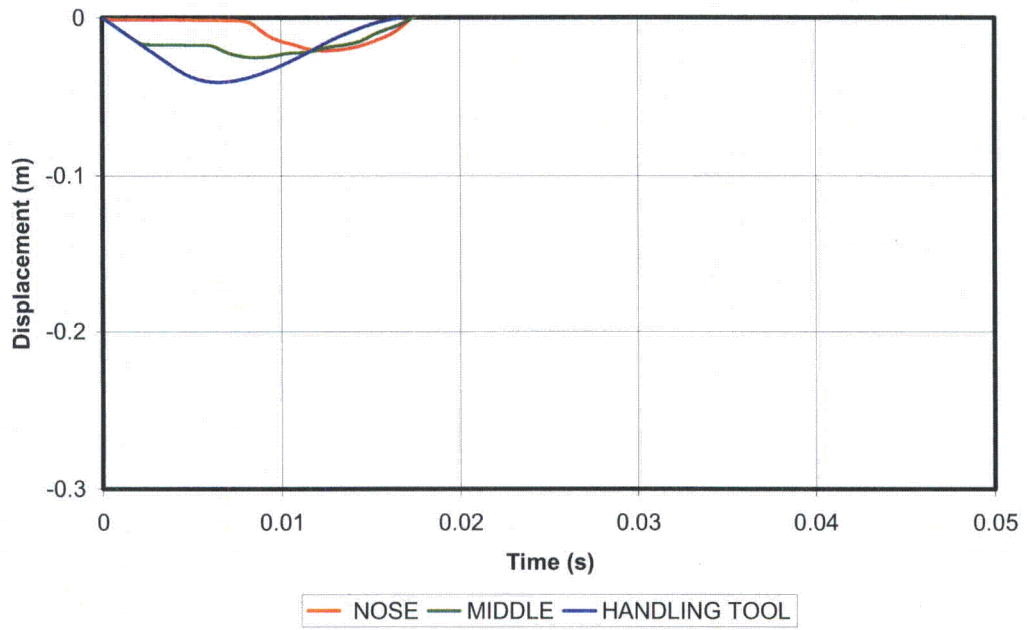


Figure 4-36. Spent Fuel, Intersection, with Tool. Fuel Displacements

PEEQ  
SNEG, (fraction = -1.0)  
(Avg: 75%)

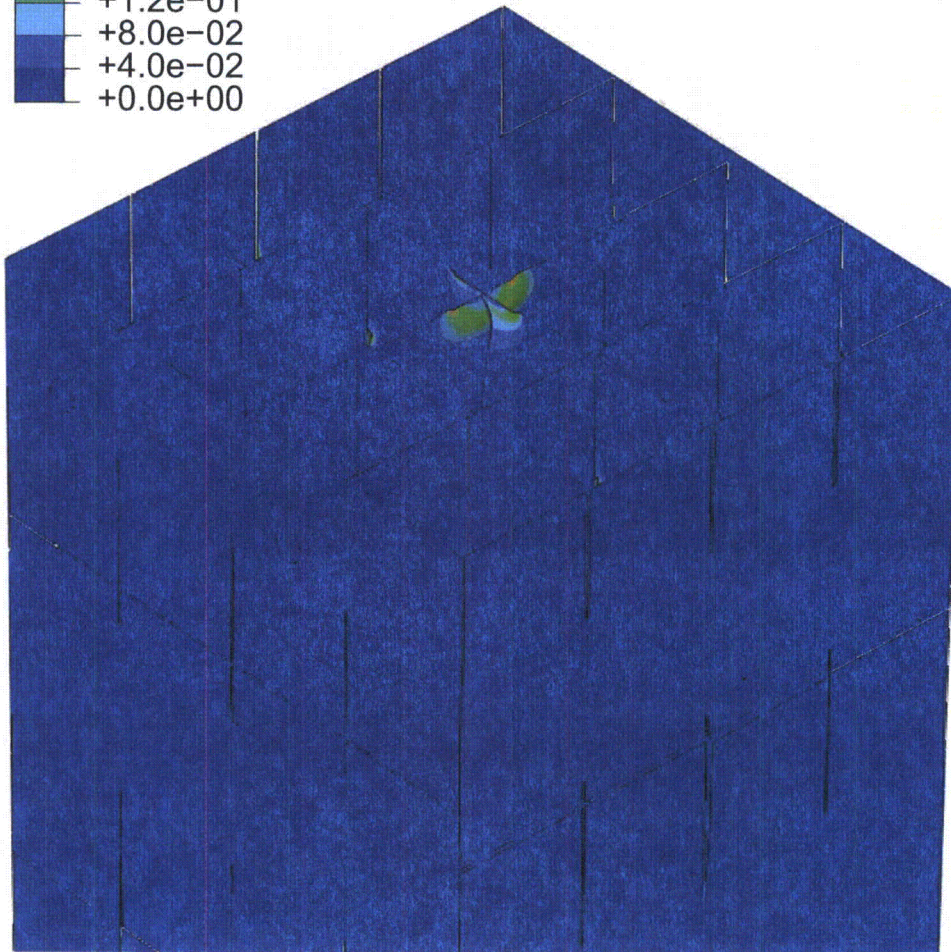
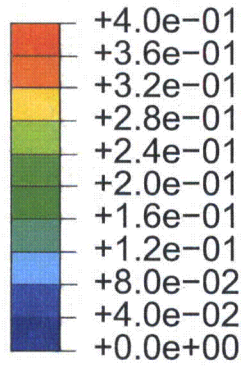
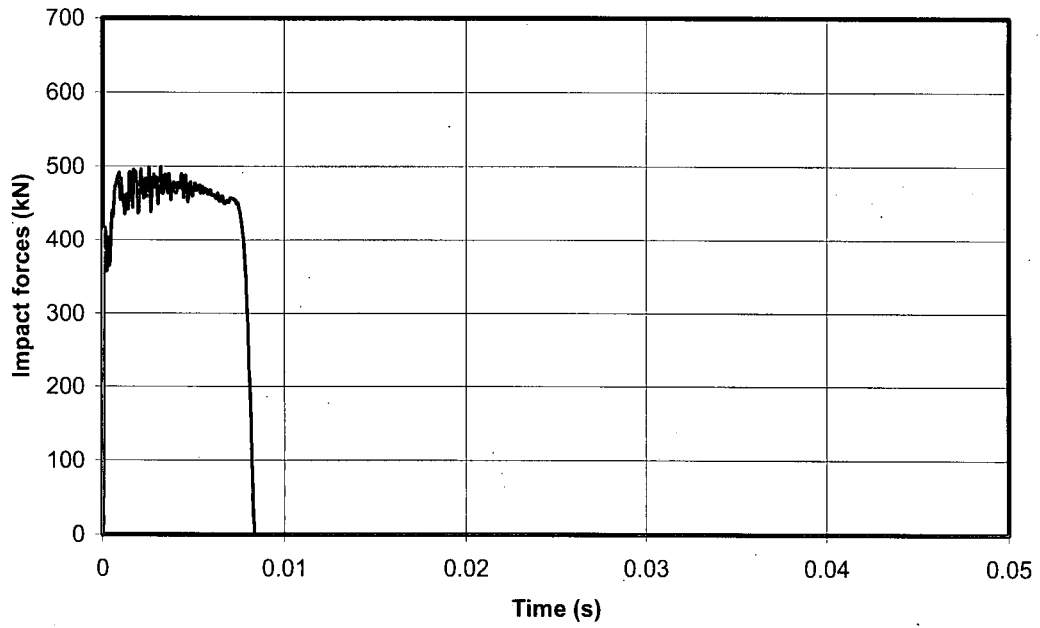


Figure 4-37. Spent Fuel, Intersection, with Tool. Plastic Deformations



**Figure 4-38. Spent Fuel, Intersection, without Tool. Impact Forces**

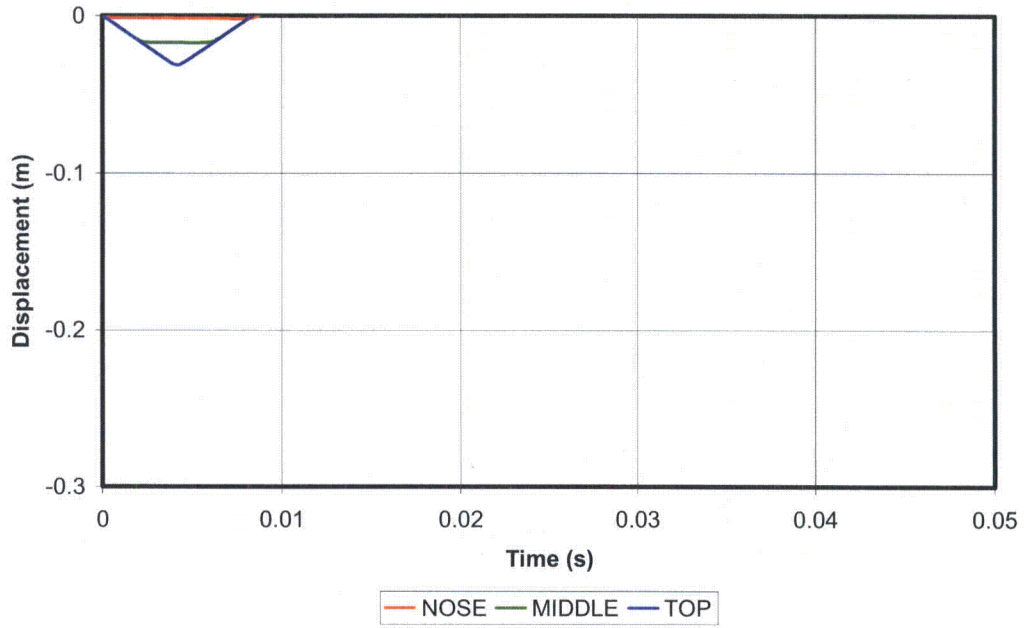


Figure 4-39. Spent Fuel, Intersection, without Tool. Fuel Displacements

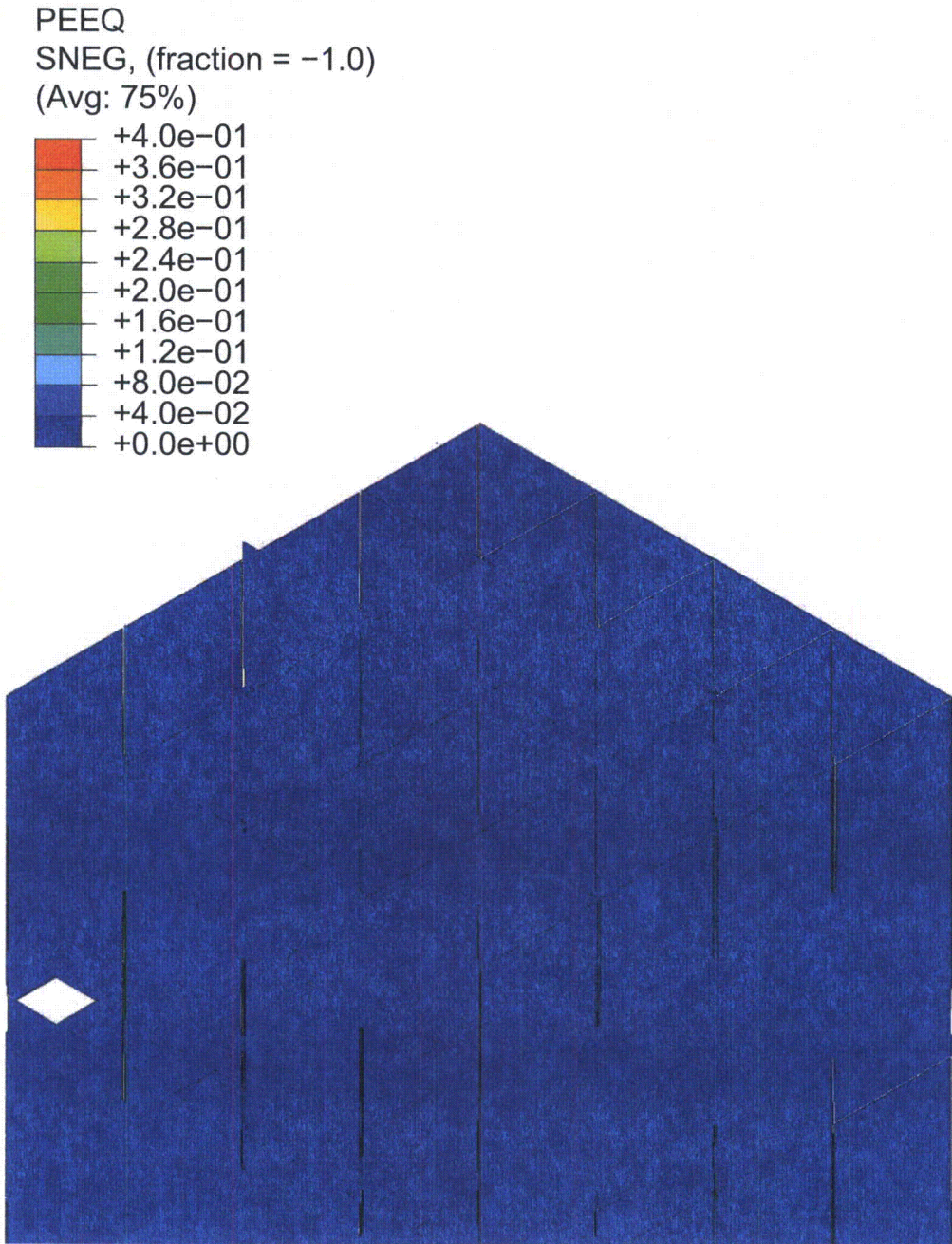


Figure 4-40. Spent Fuel, Intersection, without Tool. Plastic Deformations

## 4.5 FRESH FUEL RACKS

This section is dedicated to analyzing the postulated impacts on the racks for fresh fuel. These impacts are all assumed to occur when the fuel element is accidentally released from an elevation 1 m above the bottom plate of the rack. The fuel element may or may not be accompanied by the handling tool in the drop. Because of the smaller drop height, the present impacts are far less energetic than those studied in previous sections.

After being released, the element may impact the top of the short wall of the cell or proceed to impact the bottom plate. Both of these problems are analyzed in the present section.

### 4.5.1 *Impact on the Base Plate*

The impact velocity for 1 m drops onto the base plate, disregarding energy losses by interaction with the water, is 4.43 m/s.

The mesh used for analysing the impact in a cell next to a stiffener is shown in Figure 4-41. For a fuel element falling together with the handling tool, the resulting history of impact forces can be seen in Figure 4-42 and the deformations generated appear in Figure 4-43.

The timing along the history of forces is similar to that characterising the impacts on the base plate of the spent fuel racks. Timing is essentially prescribed by the vibrational characteristics of the fuel element together with the handling tool. What is different is the level of forces developed, which is now smaller as a consequence of the smaller impact velocity. The first part of the history, with sustained forces around 0.24 MN, approximately coincides with the theoretical expectations for impact of an elastic bar; the second part reflects the deceleration of the fuel handling tool.

The plastic deformations are of an essentially local nature and remain below 0.04, hence much lower than ductility of the material, which is 0.4.

When the analysis is repeated without the handling tool, the force history (Figure 4-44) is not very different, except that the hump associated with the handling tool is no longer present. The deformations induced are now very small, as indicated in Figure 4-45.

### 4.5.2 *Impact on the Wall*

The other possible impact against a fresh fuel rack is the one that could take place against the upper edge of the short outer wall of the cell. The drop height is only 0.400 m and the impact velocity, neglecting any water interaction effects, is 2.80 m/s.

Such an impact has little significance from the viewpoint of the forces generated. The information being sought is the magnitude of the distortions caused on the short wall and the possible transmission of the effects to the side walls.

Figure 4-46 presents the mesh used and Figure 4-47 shows the effects of the postulated impact when the fuel element drops together with the handling tool. Given the relatively small energy of the drop, the distortions caused are only moderate and the plastic deformations do not reach

the ductility of the material, thus no tearing of the wall would take place. Finally, no deleterious effects occur on the side walls.

The effects are even smaller if the fuel element drops without the handling tool. Figure 4-48 shows that the plastic strains induced are indeed negligible.

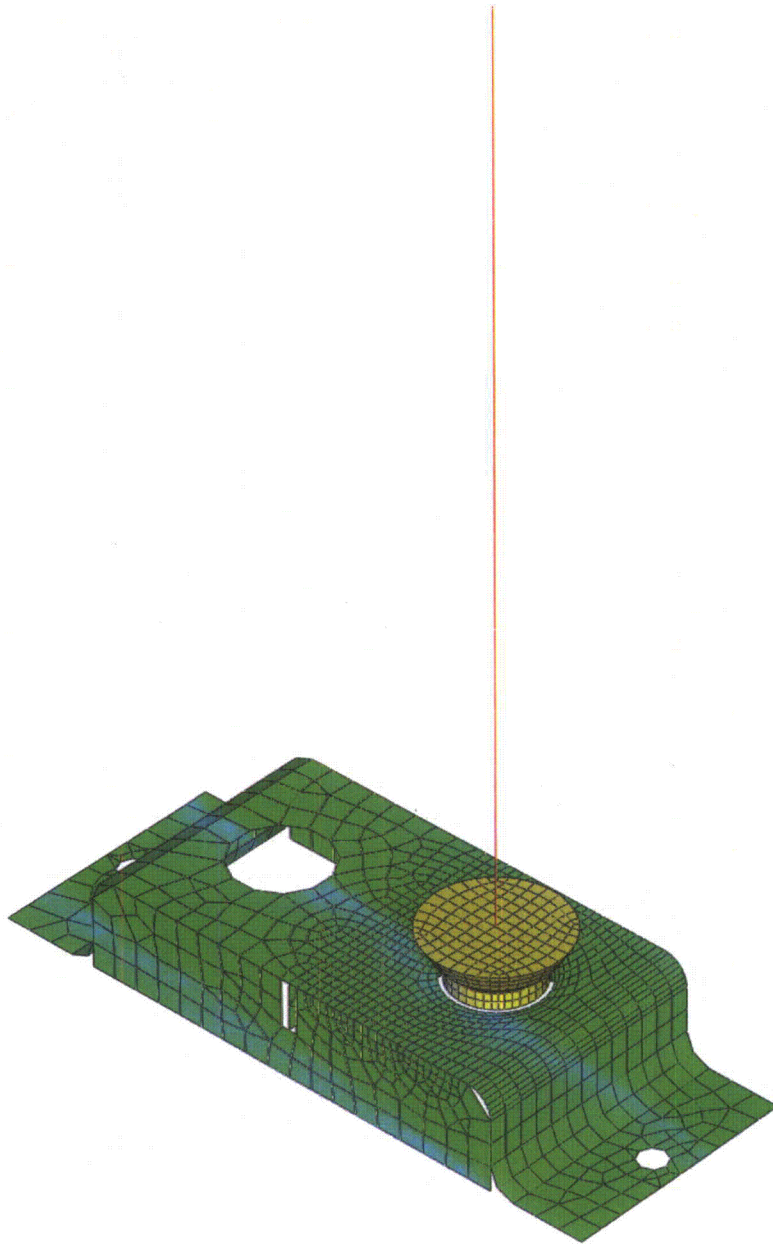


**Figure 4-41. Fresh Fuel, Bottom Plate. View of the Mesh**

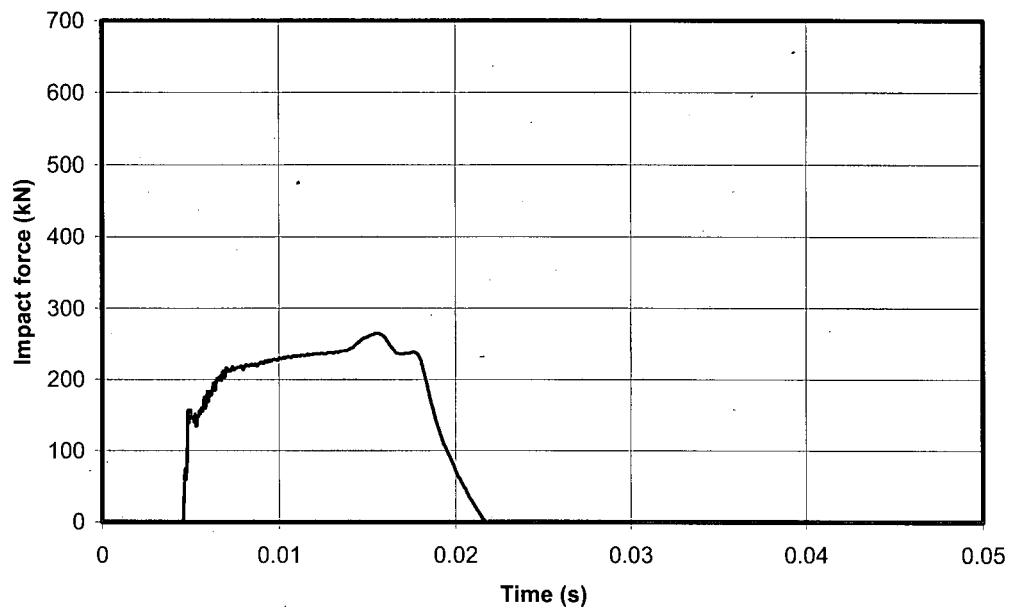


**Figure 4-42. Fresh Fuel, Bottom Plate, with Tool. Impact Forces**

PEEQ  
SNEG, (fraction = -1.0)  
(Avg: 75%)

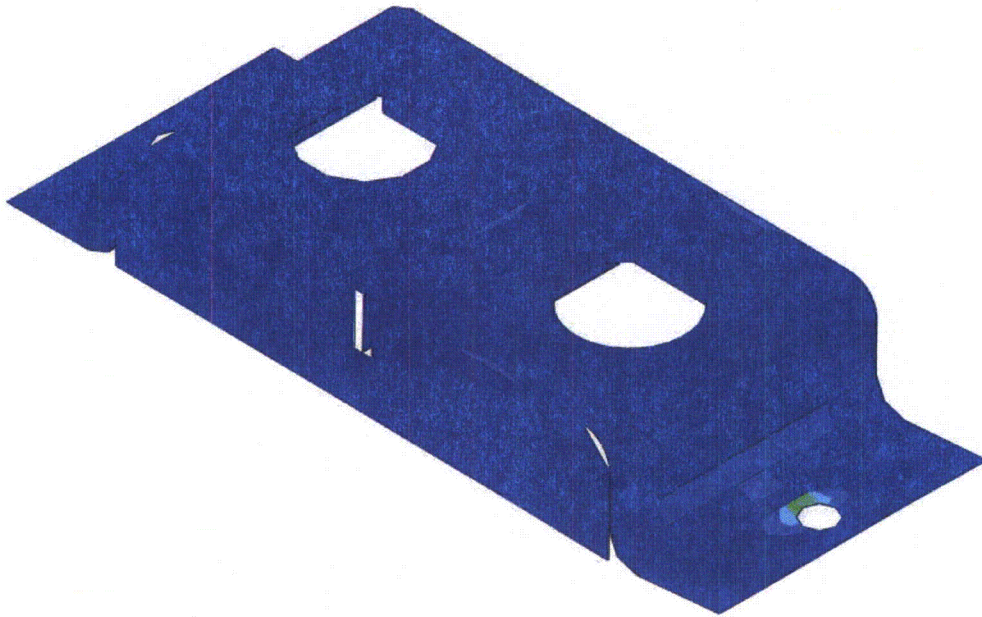
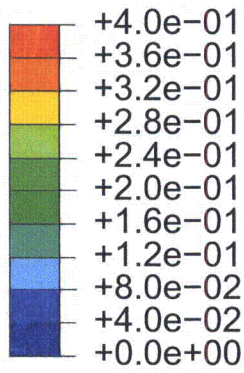
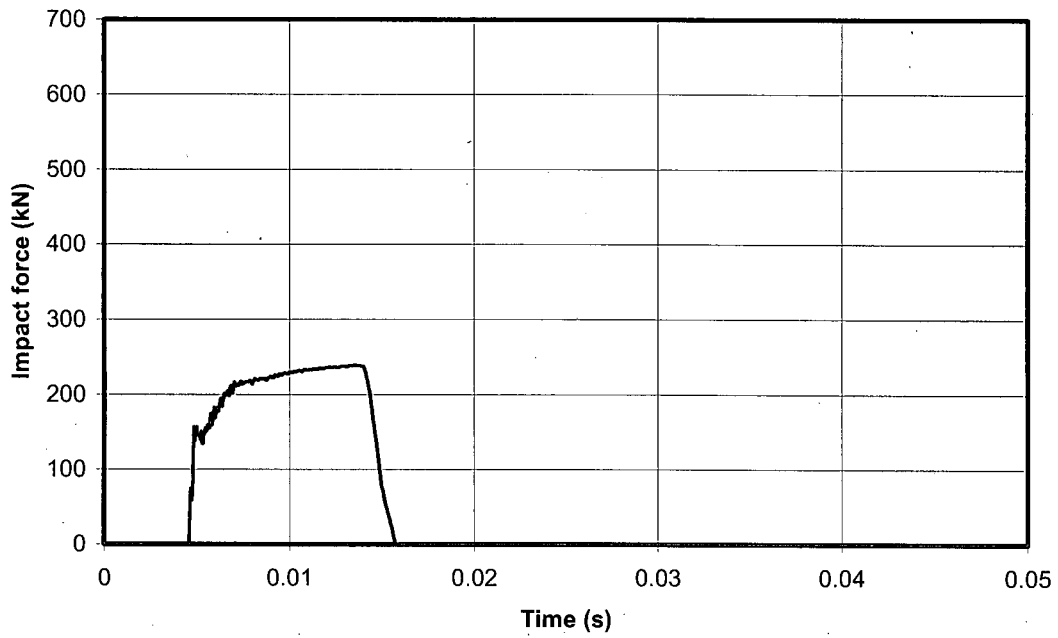
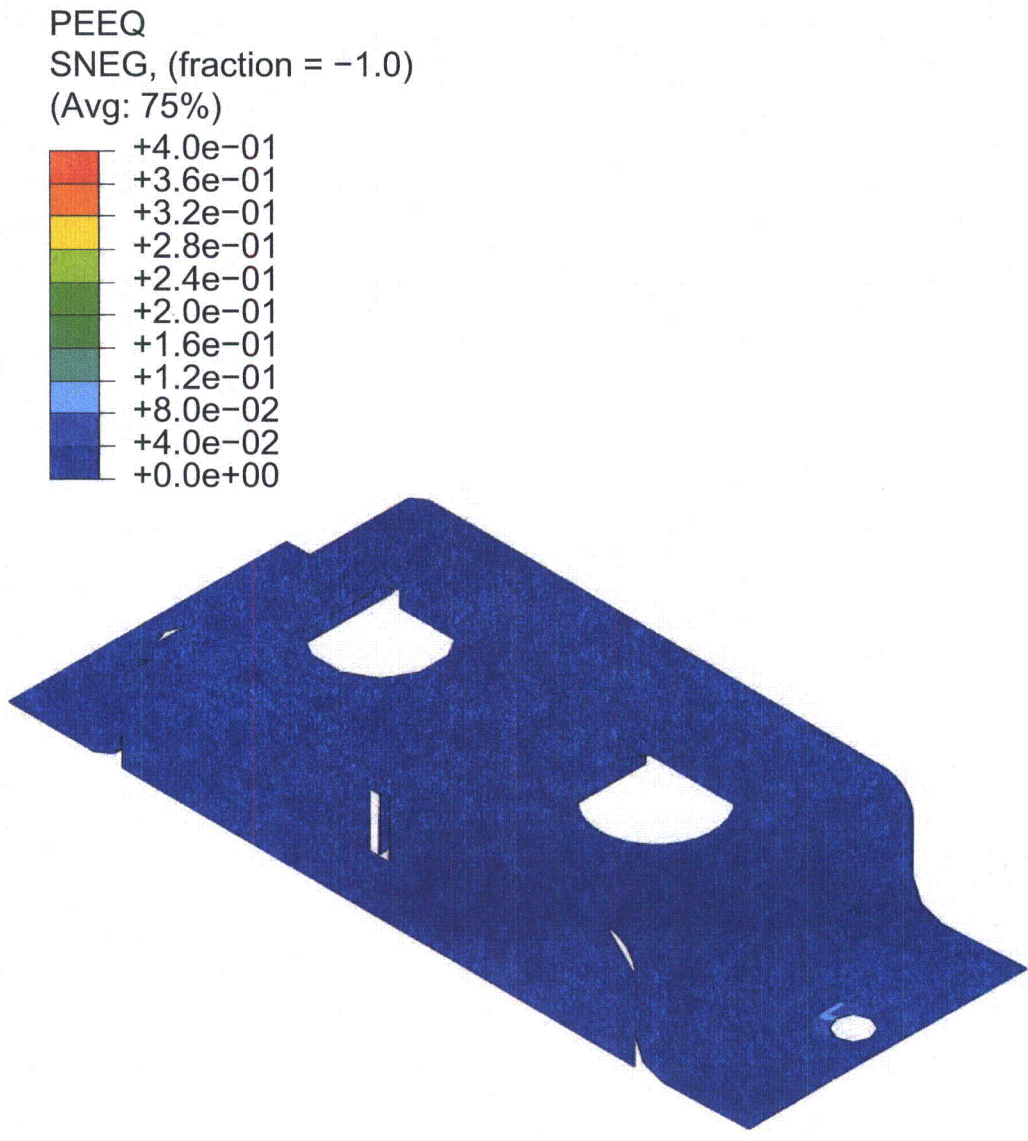


Figure 4-43. Fresh Fuel, Bottom Plate, with Tool. Plastic Deformations



**Figure 4-44. Fresh Fuel, Bottom Plate, without Tool. Impact Forces**



**Figure 4-45. Fresh Fuel Bottom Plate, without Tool. Plastic Deformations**

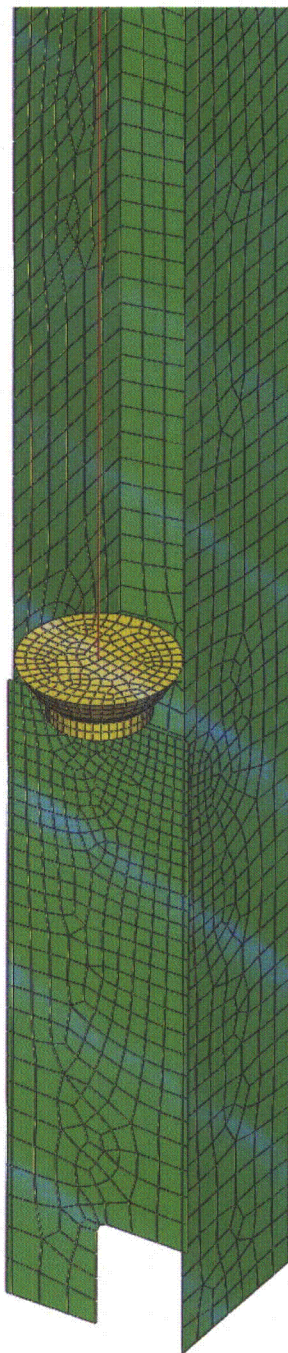


**Figure 4-46. Fresh Fuel, Wall. View of the Mesh**

PEEQ  
SNEG, (fraction = -1.0)  
(Avg: 75%)

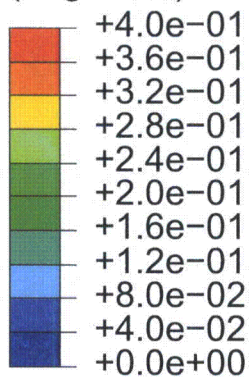


Figure 4-47. Fresh Fuel, Wall with Tool. Plastic Deformations

PEEQ  
SNEG, (fraction = -1.0)  
(Avg: 75%)

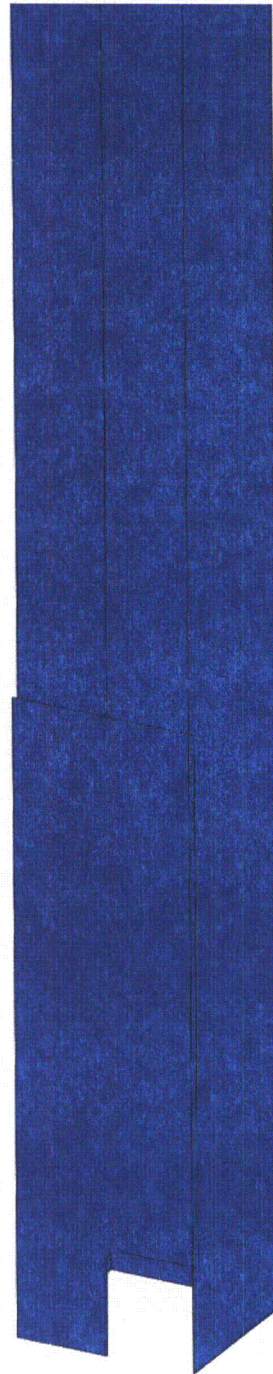
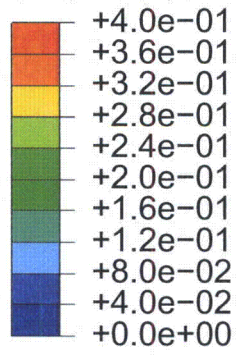


Figure 4-48. Fresh Fuel, Wall, without Tool. Plastic Deformations

## 4.6 CONCLUSIONS

Analyses have been conducted of the consequences of the impacts arising from postulated drops of fuel elements onto the ESBWR fuel storage racks, including both the racks for spent fuel and for fresh fuel. The analyses have considered both the cases in which the element is arrested by impacts against the upper part of cell walls and those in which the dropped element continues falling through a storage cell until it impacts the base plate. Also, all analyses have been performed twice, taking into account that the handling tool may or may not accompany the fuel element in the drop.

As a result of the analyses conducted, the following conclusions can be offered:

### Spent Fuel Racks

1. From the viewpoint of possible damage to the walls, the most demanding impacts are those taking place against the top of the spent fuel racks, which occur after 6.4 m drops with a velocity of 7.82 m/s.
2. When these impacts affect a single wall with the slots in the lower part of the plate, considerable local damage is caused on the upper part of the wall, extending to a depth of about 7 cm if the fuel element falls with the handling tool and about 4 cm otherwise. Such effects are acceptable because they do not reach the active zones of the elements. Impact forces are always moderate and do not exceed 0.35 MN.
3. When the impacts affect a single wall with the slots in the upper part of the plate, the impacted wall can easily bend away, thus generating a fairly soft response. As a consequence, the dropped element is able to advance about 20 cm into the rack if it falls together with the handling tool and about 10 cm without it. Such effects are again acceptable because the 10 cm drop is insufficient to reach the active zones of the elements. It should also be noticed that a greater penetration is not possible by wall bending, but would require tearing through the wall material; this implies that the 20 cm mentioned will not be exceeded.
4. When the impacts take place at the intersection of cell walls, the target is more competent than in impacts against wall single walls. The deformations are therefore considerably smaller and the indentation caused in the rack does not go beyond 3 cm.
5. Impacts against the base plate of the spent fuel racks are due to drops 1.8 m above the rack and result in impact velocities of 5.68 m/s. After an initial peak of 0.41 MN, the impact force quickly stabilizes at about 0.34 MN, a plateau that will eventually be followed by a 0.67 MN hump if the handling tool accompanies the fuel drop in its fall. In all cases the plastic strains remain below the ductility of the material.

### New Fuel Racks

6. The impacts postulated against the fresh fuel racks have very moderate effects because the drops occur from only 1 m above the base plate. If the handling tool falls with the fuel element, irrespective of the location in relation with the stiffeners, peak impact forces do not exceed 0.27 MN, a figure that decreases to 0.24 MN without the handling tool. In all cases plastic strains remain covered by the ductility of the material.

7. Finally, impacts on the short front wall of the cell correspond to only 0.4 m drops. The deformations produced are very limited and local and they do not extend to the side walls separating the element from the surrounding ones.

In summary, as a general conclusion, it can be stated that both racks are capable of sustaining the postulated impacts within the bounds imposed by the specifications.

#### **4.7 REFERENCES**

1. ASME - American Society of Mechanical Engineers (2003) "ASME Section III. Boiler and Pressure Vessel Code".
2. GE - General Electric (1978) "6' Fuel Drop Analysis", Report EC-07 Rev. 0.
3. GE Hitachi Nuclear Energy (2008) "Fuel Storage Rack Design Specification", Document No. 26A7032 Rev.2,
4. SIMULIA (2008) "Abaqus/Explicit Users' Manual", Version 6.8, Providence, Rhode Island.

## 5. THERMAL-HYDRAULIC ANALYSIS (17.3 MW CASE)

The analysis in this section assumes an abnormal heat load input of 17.3 MW. However, this heat load was determined not to be a bounding condition. An updated abnormal condition heat load of 19.0 MW (Reference 11) is bounding and shall be considered in addition to the analyses performed at 17.3 MW and 29.0 MW. See Appendix G for the evaluation of the 19.0 MW case.

### 5.1 INTRODUCTION

The purpose of this analysis is to determine the maximum peak temperatures that will be reached at the exit of the spent fuel racks in the spent fuel pool and the buffer pool in the ESBWR nuclear power station. Also, analysis shall demonstrate that these fuel storage racks are designed such that nucleate boiling is prevented.

A Computational Fluid Dynamics (CFD) based method will be used for the spent fuel pool analysis. This will allow analysis of the behavior of the water within the pool and the temperatures that the water will reach.

Cooling water flow provided to the Buffer Pool is equal to cooling water flow provided to the SFP. Since the heat loads in the Buffer Pool are significantly less than the heat loads in the SFP, the analysis for the Buffer Pool is bounded by the analysis of the SFP (See Section 5.4).

#### 5.1.1 Inputs / Assumptions

1. There are two postulated scenarios to be evaluated for the spent fuel pool (SFP):

a. Normal Conditions

- Heat Load = 10-Year spent fuel accumulation  
= 7.626 MW (Reference 1)
- Maximum Pool Bulk Temp = 48.9°C (Reference 1)
- Pool Cooling Rated Flow Rate = 545.1 m<sup>3</sup>/hr = 150.96 Kg/s  
(Reference 1)

b. Abnormal Conditions

- Heat Load = 10-Year spent fuel accumulation + full core offload  
= 17.3 MW (Reference 1)
- Maximum Pool Bulk Temp = 60°C (Reference 1)
- Pool Cooling Rated Flow Rate = 1090.2 m<sup>3</sup>/hr = 301.92 Kg/s  
(Reference 1)

2. For the purpose of this analysis, it is assumed that the FAPCS maintains the pool at a steady bulk temperature and always removes heat at the rate it is produced. This assumption simplifies the model into a steady-state analysis by avoiding bulk temperature transients.

### **5.1.2 Acceptance Criteria**

The design of the racks shall allow adequate natural circulation to prevent nucleate boiling within the stored fuel assemblies.

The local coolant temperature of the fluid exiting the top of the spent fuel storage rack shall not exceed the temperature limit for stress properties of the various fuel rack materials, which is 121°C (250°F).

## **5.2 CALCULATION METHODOLOGY**

### **5.2.1 General Description**

The calculation methodology for this analysis consists of two phases.

#### **5.2.1.1 Pool Inlet Temperature Determination**

In order to model the fluid dynamics of the pool, it is necessary to determine the temperature of the cooled water being returned to the pool from the FAPCS. The pool inlet temperature will be back-calculated from the assumptions described in 5.1.1. Because this analysis assumes a steady-state condition where the pool bulk temperature is “locked in” at its maximum value, the temperature of the pool inlet water does not necessarily reflect the realistic capabilities of the FAPCS. To determine the maximum inlet temperature of the water in each of the cases, the following values are used: the maximum bulk temperature (also equivalent to the pool outlet temperature), the heat generated by the fuel elements, and the flow rate provided by the FAPCS. Although the calculated pool inlet temperature is not a realistic design parameter, it is conservative in the context of this analysis due to the higher-than-normal bulk pool temperature.

#### **5.2.1.2 Calculation of the Velocities and Temperatures within the Spent Fuel Pool (SFP)**

Once the model inputs have been determined, the calculation of the velocities and temperatures are performed using a CFD based method, in order to evaluate the bounding temperature profile within the SFP.

## 5.2.2 Pool Inlet Temperature Determination

In this section, the maximum pool inlet temperatures are calculated for the normal and abnormal conditions.

The normal condition is defined as the spent fuel from 10 years of plant operation, which is limited by the capacity of the initial configuration of fuel racks in the spent fuel pool. The abnormal condition is defined as the spent fuel from 10 years of plant operation plus a full core offload, which is also limited by the capacity of the initial configuration of fuel racks in the spent fuel pool.

### 5.2.2.1 Normal Conditions Case

The heat generated under normal conditions is 7.626 MW (Reference 1).

In the normal conditions case, the flow rate is  $545.1 \text{ m}^3/\text{h} = 150.96 \text{ Kg/s}$  (Reference 1).

The normal maximum pool bulk temperature is  $48.9^\circ\text{C}$  (Reference 1).

$$\Delta T = \frac{\text{Heat}}{C_p \cdot \text{Flow}} = \frac{7.626 \cdot 10^6 \text{ W}}{4182 \frac{\text{J}}{\text{Kg} \cdot \text{K}} \cdot 150.96 \frac{\text{Kg}}{\text{s}}} = 12.08 \text{ K}$$

Maximum Inlet Temperature

$$T_{\text{in}} = 48.9 - 12.08 = 36.8^\circ \text{C}$$

Therefore, the maximum inlet temperature is  $36.8^\circ\text{C}$  for the normal conditions case.

### 5.2.2.2 Abnormal Conditions Case

The heat generated under abnormal conditions is 17.3 MW (Reference 1). In the abnormal conditions case, the flow rate is  $1090.2 \text{ m}^3/\text{h} = 301.92 \text{ Kg/s}$  (Reference 1).

$$\Delta T = \frac{\text{Heat}}{C_p \cdot \text{Flow}} = \frac{17.3 \cdot 10^6 \text{ W}}{4182 \frac{\text{J}}{\text{Kg} \cdot \text{K}} \cdot 301.92 \frac{\text{Kg}}{\text{s}}} = 13.7 \text{ K}$$

Maximum Inlet Temperature

$$T_{\text{in}} = 60 - 13.7 = 46.3^\circ \text{C}$$

Therefore, the maximum inlet temperature is  $46.3^\circ\text{C}$  for the abnormal conditions case.

### 5.2.3 Calculation of the Velocities and Temperatures within the Spent Fuel Pool (SFP)

The calculation of the velocities and temperatures are performed using a CFD (Computational Fluid Dynamics) based method, ANSYS CFX 11.0 (Reference 2).

The Spent Fuel Pool (SFP) water has been modeled and the racks located in the SFP have been modeled as subdomains. In these subdomains a volumetric heat generation and a directional loss coefficient have been imposed (the heat generation for each rack is calculated in Sections 5.2.3.2 and 5.2.3.3 the directional loss coefficient is calculated in Section 5.2.3.1).

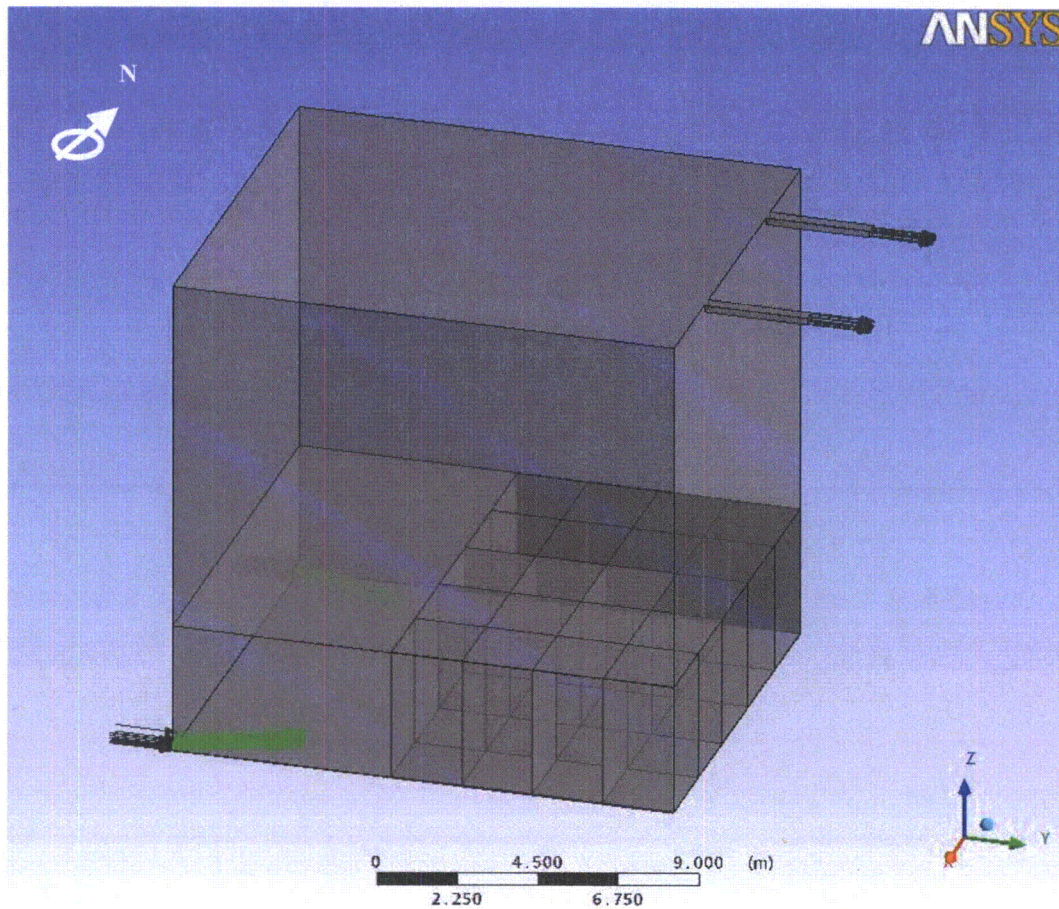


Figure 5-1. SFP Model

The rack layout modeled in Figure 5-1 represents the 10-year configuration (Reference 5). The racks in the three northern rows have an array of 15 x 12. The racks in the two southern rows have an array of 14 x 12. This layout provides a total of 3504 fuel storage spaces.

Two outlets have been modeled at the top of the SFP. Two inlet areas have been modeled at the bottom of the SFP in the corners opposite the racks, including the effect of the diffuser, driving the flow in an angle of 20° measured from the inlet normal direction. The actual inlet locations are inboard from the corners, equally spaced between the pool walls. As this difference from the modelled locations is considered to have negligible impact on results, the model was not modified to reflect the actual inlet locations.

A 42 mm gap between the racks and the northern and southern pool walls has been included in the model. No gap has been considered between the racks and the eastern pool wall. Nor was any gap considered between racks. The gaps used in the model are conservative relative to actual design values.

### 5.2.3.1 Loss Coefficient Calculation

Figure 5-2 (Reference 8) shows the loss coefficient in the vertical direction inside the racks. This curve is mathematically fit using the following parabolic expression:

$$y = ax^2 + bx + c$$

Where:

$y$  is the pressure drop (PSI)

$x$  is the mass flow rate (LBM/hr)

Since there is no pressure drop when the mass flow rate is zero,  $c = 0$ . From the parabolic fitting, the coefficients values are:

$$b = 0$$

$$a = 6.2 \cdot 10^{-10} \text{ PSI} \frac{\text{hr}^2}{\text{LBM}^2} = 269.55 \frac{1}{\text{kg} \cdot \text{m}}$$

Thus, pressure loss can be represented by the following formula:

$$\Delta P = K \cdot (m)^2$$

Where:

$$K = 269.55 \text{ Kg}^{-1} \cdot \text{m}^{-1}$$

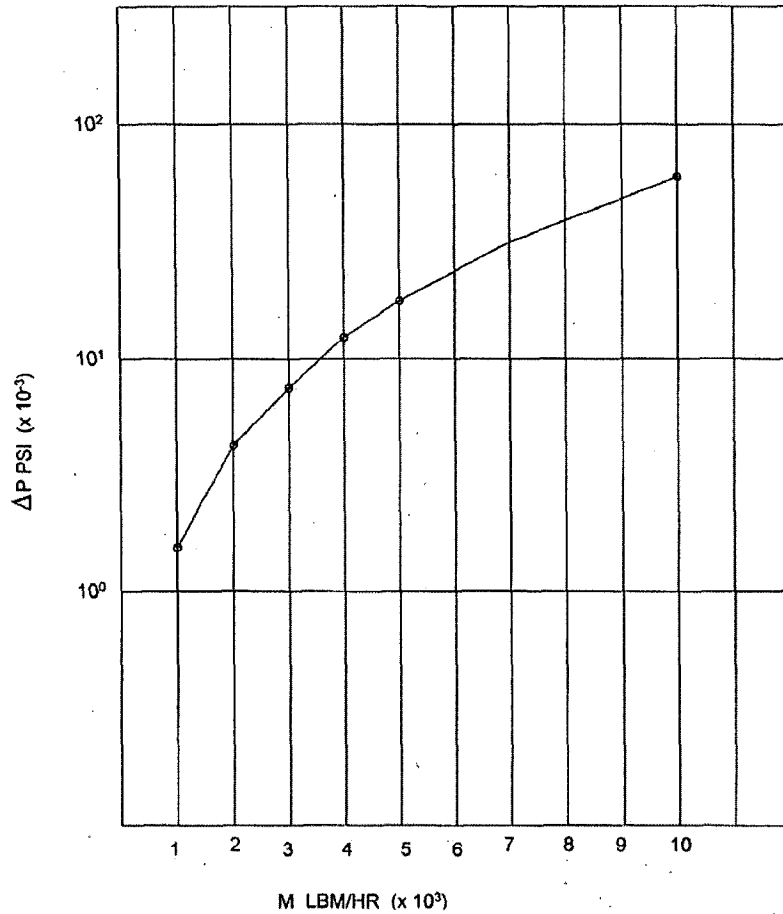


**Figure 5-2. Loss coefficient in Racks**

The CFD code requires that this loss coefficient be input as a function of velocity. Therefore, an additional calculation using the following formula must be performed. An 8% safety factor has been applied to the loss coefficient obtained previously ( $K=269.55\text{Kg}^{-1}\cdot\text{m}^{-1}$ ).

$$K_N \cdot \rho \cdot L \cdot V^2 = K \cdot (m)^2$$

$$m = \rho \cdot V \cdot A$$

$$K_N = K \cdot \rho \cdot \frac{A^2}{L} = 269.55 \cdot 1.08 \cdot 1000 \cdot \frac{(0.168^2)^2}{3.856} = 60.13 \text{m}^{-1}$$

This is the value used for all the racks in the model. To model vertical-only water movement inside the racks, the loss coefficient applied in the two horizontal directions (x, y) is assumed to be  $10^6$  times greater than in the vertical direction.

To simulate the heat generation produced by the Fuel Assemblies (FA) inside the racks, a volumetric heat generation has been applied to the subdomains. For conservatism, it has been assumed that the most recently discharged FA (the most active FA) are located together. The temperature reached with this configuration is greater than the temperature that would be reached if the discharged FA were distributed uniformly between all the racks in the SFP.

### 5.2.3.2 Heat Generation Calculation in Each Rack Under the Normal Conditions Case

The heat generated by the FA under the normal conditions case is = 7.626MW. For conservatism, it is assumed that all the heat is generated by the discharged FA.

$$\frac{7.626 \cdot 10^6 W}{476 FA_{new}} = 16021 \frac{W}{FA_{new}}$$

In reference to the FA distribution between the racks, the worst-case configuration has the discharged FA located in the racks farthest from the SFP inlet. The discharged FA will be located in the racks 5, 9 and 13.

$$\text{Heat generated in rack 5: } 180 FA_{New} \cdot 16021 \frac{W}{FA_{New}} = 2883780W$$

$$\text{Heat generated in rack 9: } 180 FA_{New} \cdot 16021 \frac{W}{FA_{New}} = 2883780W$$

$$\text{Heat generated in rack 13: } 7.626 \cdot 10^6 W - 2883780W - 2883780W = 1858440W$$

The rest of the racks do not have any heat generation applied.

### 5.2.3.3 Heat Generation Calculation in Each Rack Under the Abnormal Conditions Case

The heat generated by the FA under the abnormal conditions case is = 17.3MW. Of the 17.3MW considered, 7.626MW is attributed to the accumulation of 10-years of spent fuel. The remainder is attributed to a full core offload.

$$\frac{(17.3 - 7.626) \cdot 10^6 W}{1132 FA_{new}} = 8545.93 \frac{W}{FA_{new}}$$

Fuel from a full core offload requires 6 complete racks and 76 storage spaces in a 7th rack. The heat generated by the accumulation of 10 years of spent fuel is divided among the remainder of storage capacity.

The hottest fuel assemblies are conservatively assumed to be located in the area receiving the least amount of cooling. These racks are 5, 6, 9, 10, 13, and 14.

$$\text{Heat generated in rack 5, 6, 9 and 10: } 180FA_{New} \cdot 8545.93 \frac{W}{FA_{New}} = 1538267.4W$$

$$\text{Heat generated in rack 13 and 14: } 168FA_{New} \cdot 8545.93 \frac{W}{FA_{New}} = 1435716.2W$$

Heat generated in rack 11:

$$(17.3-7.626) \cdot 10^6 W - 4 \cdot 1538267.4W - 2 \cdot 1435716.2W = 649498W \rightarrow FA_{New} \text{ in rack 11} = \frac{649498W}{8545.93 \frac{W}{FA_{New}}} = 76FA_{New}$$

$$\text{Number and generation of old FA: } 8 \cdot (15 \cdot 12) + 6 \cdot (14 \cdot 12) + (15 \cdot 12 - 76) = 2552FA \rightarrow \frac{7.62610^6 W}{2552FA} = 2988.24 \frac{W}{FA}$$

$$\text{so, heat generated in rack 11: } 76FA_{New} \cdot 8545.93 \frac{W}{FA_{New}} + (15 \cdot 12 - 76)FA \cdot 2988.24 \frac{W}{FA} = 960267.6W$$

Heat generated in racks not completed by new FA:

$$15 \times 12 \text{ Type: } 180FA \cdot 2988.24 \frac{W}{FA} = 537883.2W$$

$$14 \times 12 \text{ Type: } 168FA \cdot 2988.24 \frac{W}{FA} = 502024.32W$$

**5.2.4 Summary Tables**

The following tables show a summary of the model characteristics and the modeled fluid properties used.

**Model Characteristics**

Solver	CFX Serial Standard
Solver Advection Scheme	High Resolution
Simulation Type	Steady State
Buoyancy Option	Buoyant
Gravity direction	<0, 0, -9.81m/s <sup>2</sup> >
Buoyancy Ref. Temperature	60°C
Heat Transfer Option	Total Energy
Turbulence Option	k-Epsilon
Fluid	Liquid Water
	Density = 997 Kg/m <sup>3</sup>
	Dynamic Viscosity = 0.0008899 Kg/m s
	Specific Heat Capacity Cp = 4181.7 J/Kg°C
	Thermal Conductivity = 0.6069 W/m K
	Linear Variation of Density with Temperature

**Boundary Conditions**

Normal Conditions	Abnormal Conditions
In Flow Rate = 150.96 Kg/s 75.48 Kg/s (each inlet)	In Flow Rate = 301.92 Kg/s 150.96 Kg/s (each inlet)
Inlet Flow Direction = 20° Offset Diffuser, Offset towards center of pool	Inlet Flow Direction = 20° Offset Diffuser, Offset towards center of pool
Turbulence Intensity = 1%	Turbulence Intensity = 1%
Inlet Temperature = 36.8°C	Inlet Temperature = 46.3°C
Adiabatic Walls	Adiabatic Walls
Outlet Flow Rate 150.96 Kg/s (total of both outlets)	Outlet Flow Rate 301.92 Kg/s (total of both outlets)
Loss coeff = 60.13/m	Loss coeff = 60.13/m
Transverse Loss Coeff. Multiplier = 1000000	Transverse Loss Coeff. Multiplier = 1000000
Heat Generation per Section 5.2.3.2	Heat Generation perSection 5.2.3.3

### 5.2.5 CFD Model Sensitivity

CFD analysis methodology has been used in the past for other spent fuel pool thermal-hydraulic studies. The effect of hypothesis and assumptions, and also the modelling methodology (turbulence model selection, buoyancy treatment or mesh density) has been evaluated by sensitivity studies, according to the best practice guidelines for the use of CFD in nuclear reactor safety applications.

The sensitivity studies are presented in two parts: sensitivity to the numerical method and sensitivity to the mesh density.

Considering the numerical method, many parameters have been evaluated as shown below:

- Inlet mass flow rate increased by 10%
- Inlet temperature reduced by 10%
- Loss coefficient increased by 20%
- Turbulence model validated by a different model (k- $\epsilon$  model vs. SST-k- $\omega$  model)
- Reference temperature for buoyancy model reduced by 10%
- Turbulence intensity at the inlets increased by 9% (maximum allowed by the code)

The shape of the temperature distribution throughout the pool remains constant, with temperature variations (peak and bulk) of  $\approx 1.5\%$ . For variations of inlet mass flow rate, loss coefficient, and inlet temperature, the temperature variations (peak and bulk) are  $\approx 4\%$  to  $6\%$ . Inlet temperature refers to the maximum allowable pool inlet temperature. This value is dependent on the heat load in the pool, as the abnormal flow rate (301.92 Kg/s) and maximum bulk pool temperature (60°C) are analyzed as constant. As the heat load in the pool is increased, the corresponding rack exit temperature increases and the maximum allowable pool inlet temperature must decrease to maintain the bulk pool temperature. Conversely, as the heat load in the pool is decreased, the corresponding rack exit temperature decreases and the maximum allowable pool inlet temperature can increase to maintain the bulk pool temperature.

With regard to the sensitivity of mesh density, typically three cases are used for comparison: the original mesh density, a 50% increase over the original mesh density, and a 100% increase over the original mesh density. Specific examples from a specific thermal-hydraulic analysis of an operating BWR are presented below.

The temperature profiles and values of horizontal slices through the spent fuel pool are analyzed at various elevations for comparison purposes. In comparing the three models, the temperature distributions within the pools were constant and the bulk temperature variance for different locations was less than 2°C.

For the peak temperature value, the original mesh density model produced a result of 101.1°C. The 50% mesh density increase case produced a maximum peak temperature of 105.9°C. The doubled mesh density case produced a maximum peak temperature of 107.0°C. The maximum variation for peak temperature was 5.9°C.

Also a thermal-hydraulic analysis of a representative spent fuel pool has been modelled and solved by two different CFD codes. The shape of the temperature distribution throughout the pool is similar for both models.

The results of these sensitivity studies show that the hypothesis and numerical model to be valid.

### 5.3 RESULTS

Solving the two cases described previously, the results shown in the following sections are obtained.

#### 5.3.1 Temperature Distribution Under Normal Conditions Case

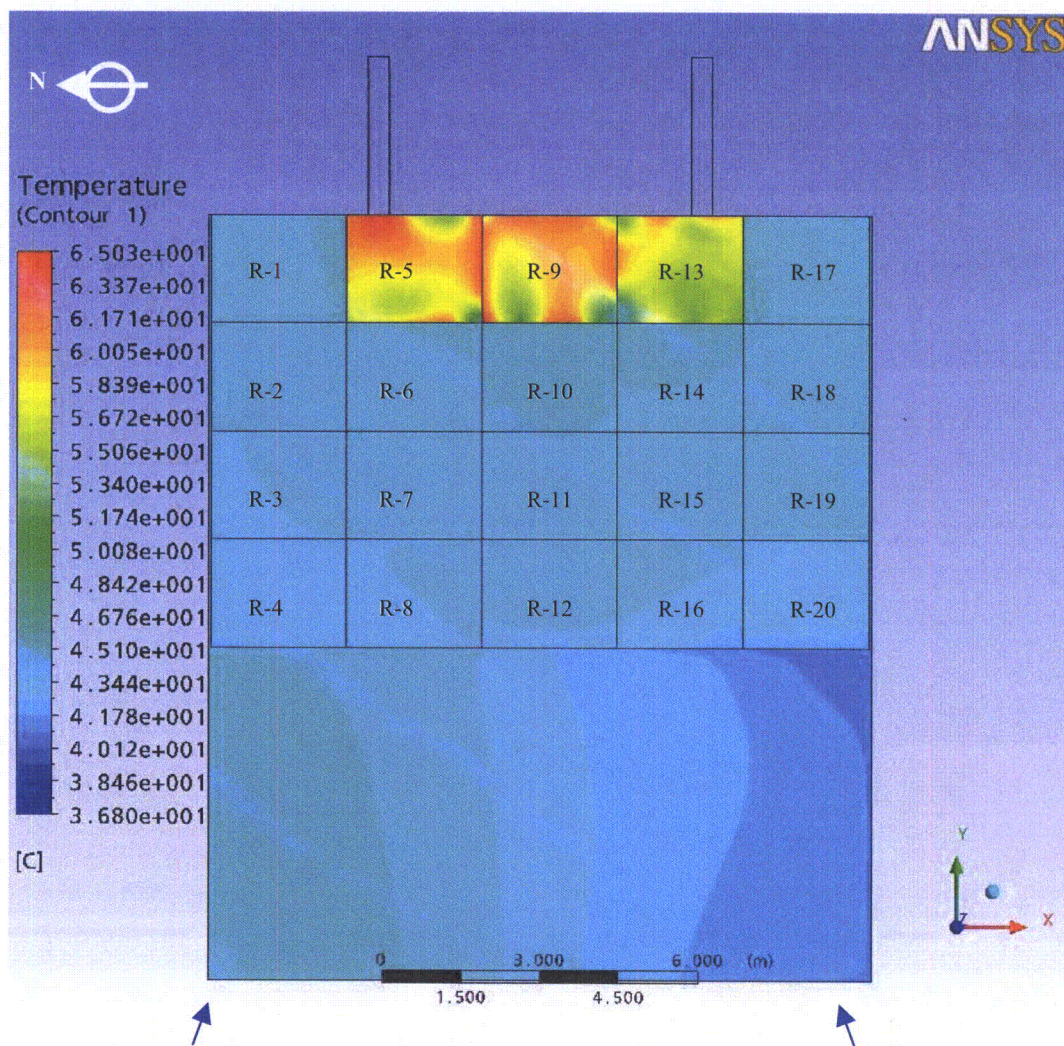
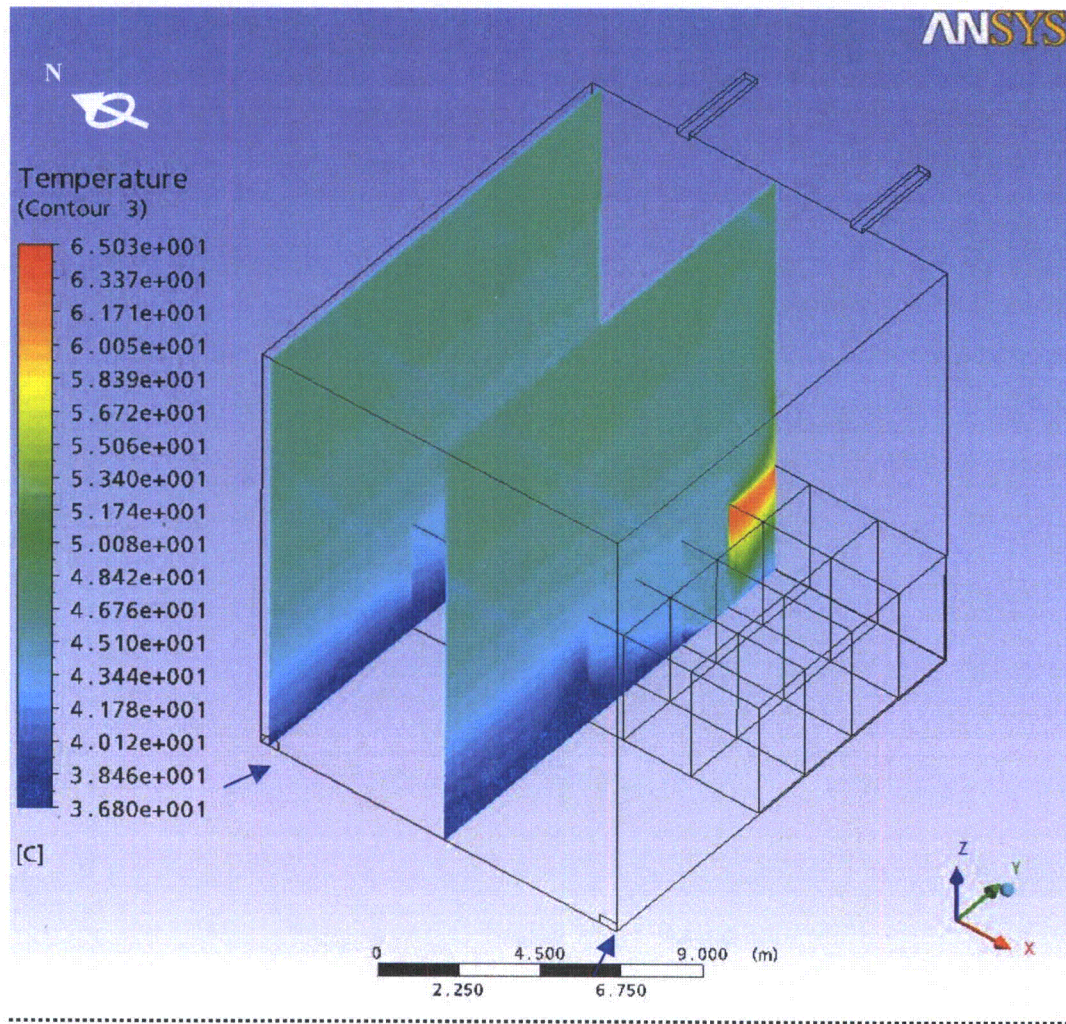


Figure 5-3. Temperature Distribution under the Normal Conditions Case (x,y)

Figure 5-3 shows the temperature distribution in the racks under the normal conditions case. The maximum peak temperature reached in this case is 65.03°C and is reached in the racks where the discharged FA are located. The maximum is reached at the top of the rack and is significantly less than the maximum allowable temperature of 121°C.



**Figure 5-4. Temperature Distribution under the Normal Conditions Case (y,z)**

Figure 5-4 shows the temperature distribution in the SFP under the normal conditions case. The temperature scale on the left ranges from the minimum to the maximum temperature on the SFP global. Given the outlet temperature of 48.9°C presented in Section 5.1.1, the maximum inlet temperature (as calculated in Section 5.2.2.1) is determined to be 36.8°C.

5.3.2 Temperature Distribution Under Abnormal Conditions Case

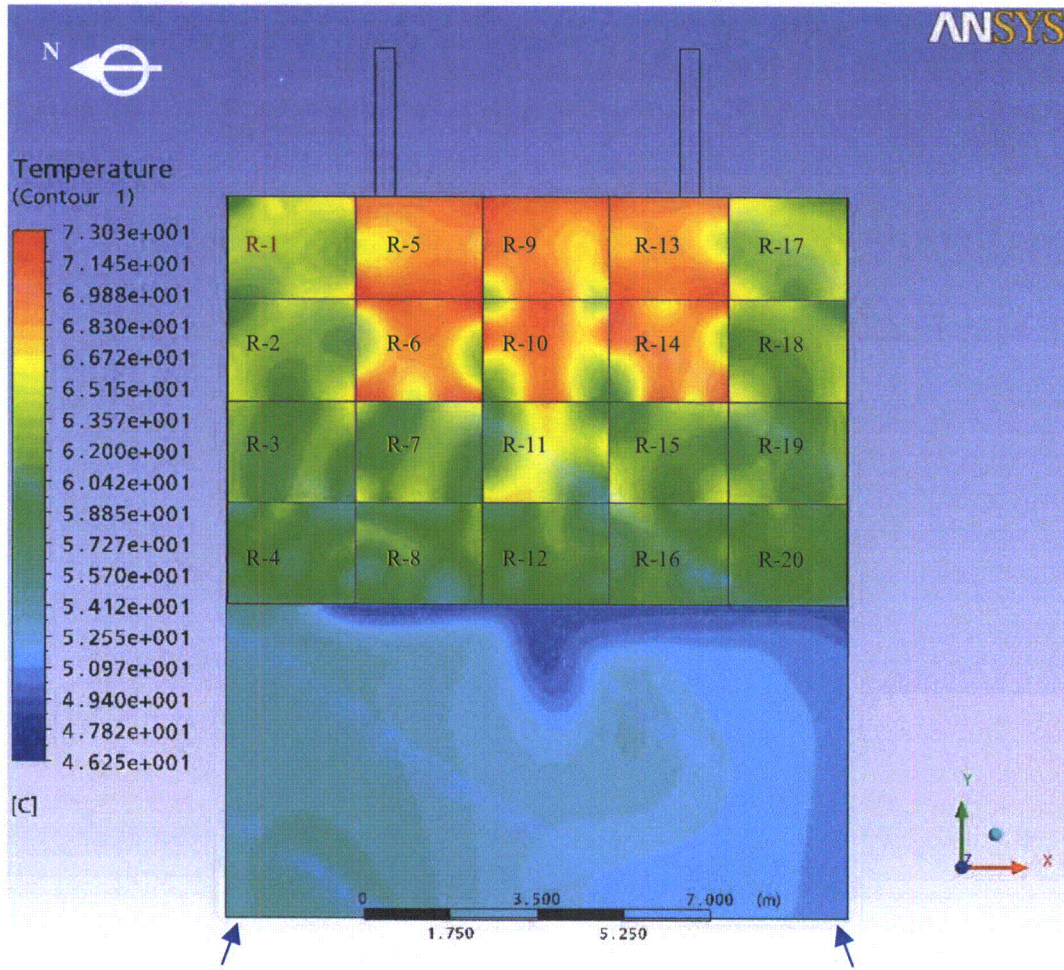
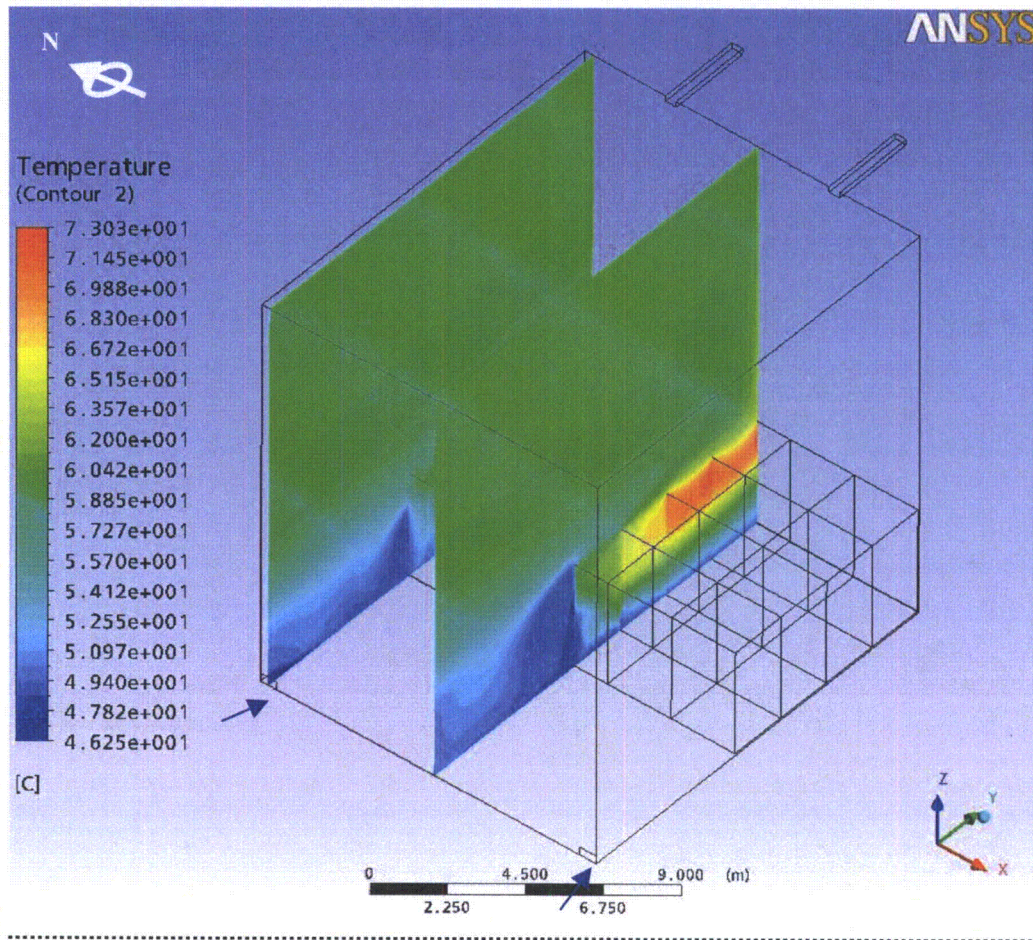


Figure 5-5. Temperature Distribution under the Abnormal Conditions Case (x,y)

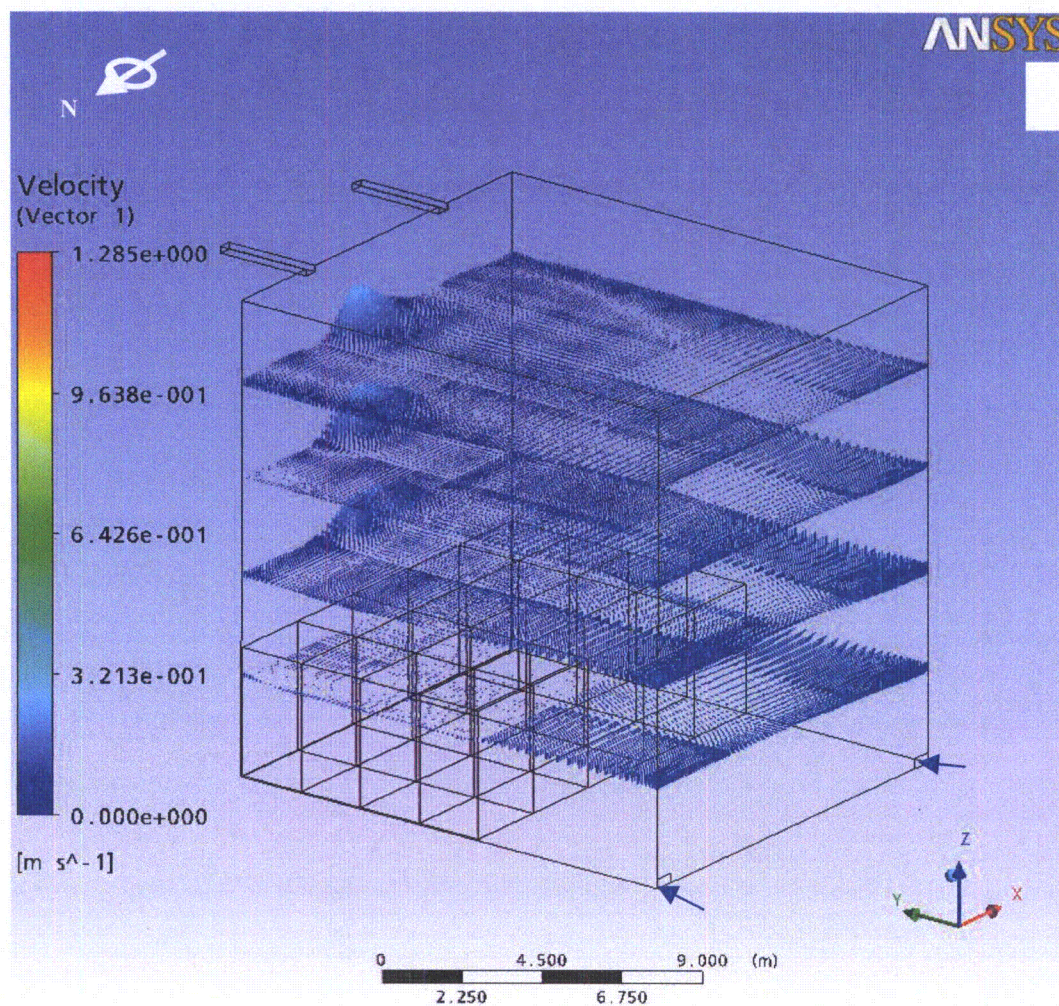
Figure 5-5 shows the temperature distribution in the racks under the abnormal conditions case. The maximum peak temperature reached in this case is 73.03°C and is reached in the racks where the discharged FA are located. The maximum is reached at the top of the rack and is significantly less than the maximum allowable temperature of 121°C.



**Figure 5–6. Temperature Distribution under the Abnormal Conditions Case (y,z)**

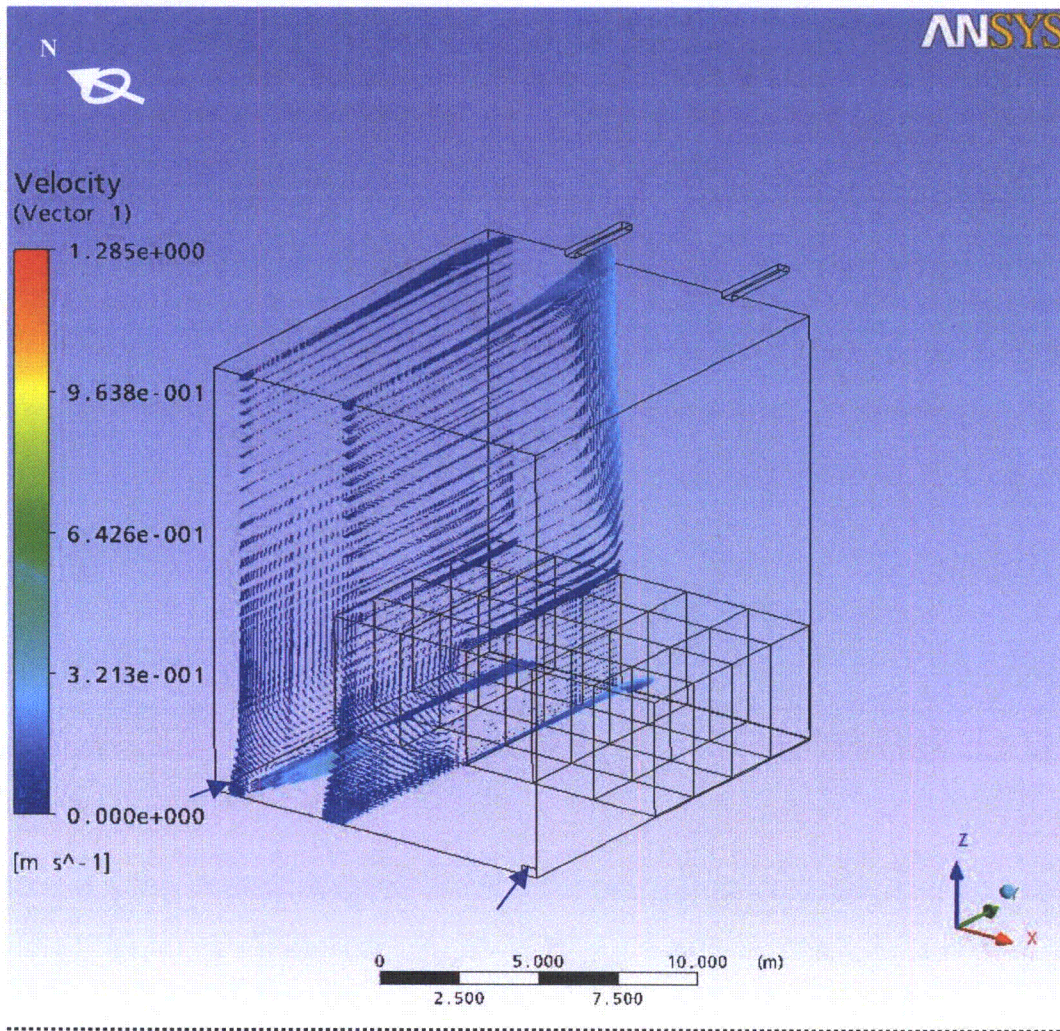
Figure 5-6 shows the temperature distribution in the SFP under the abnormal conditions case. The temperature scale on the left ranges from the minimum to the maximum temperature on the SFP global. Given the outlet temperature of 60°C presented in Section 5.1.1, the inlet temperature (as calculated in Section 5.2.2) is 46.3°C.

### 5.3.3 Velocity Distribution Under Normal Conditions Case



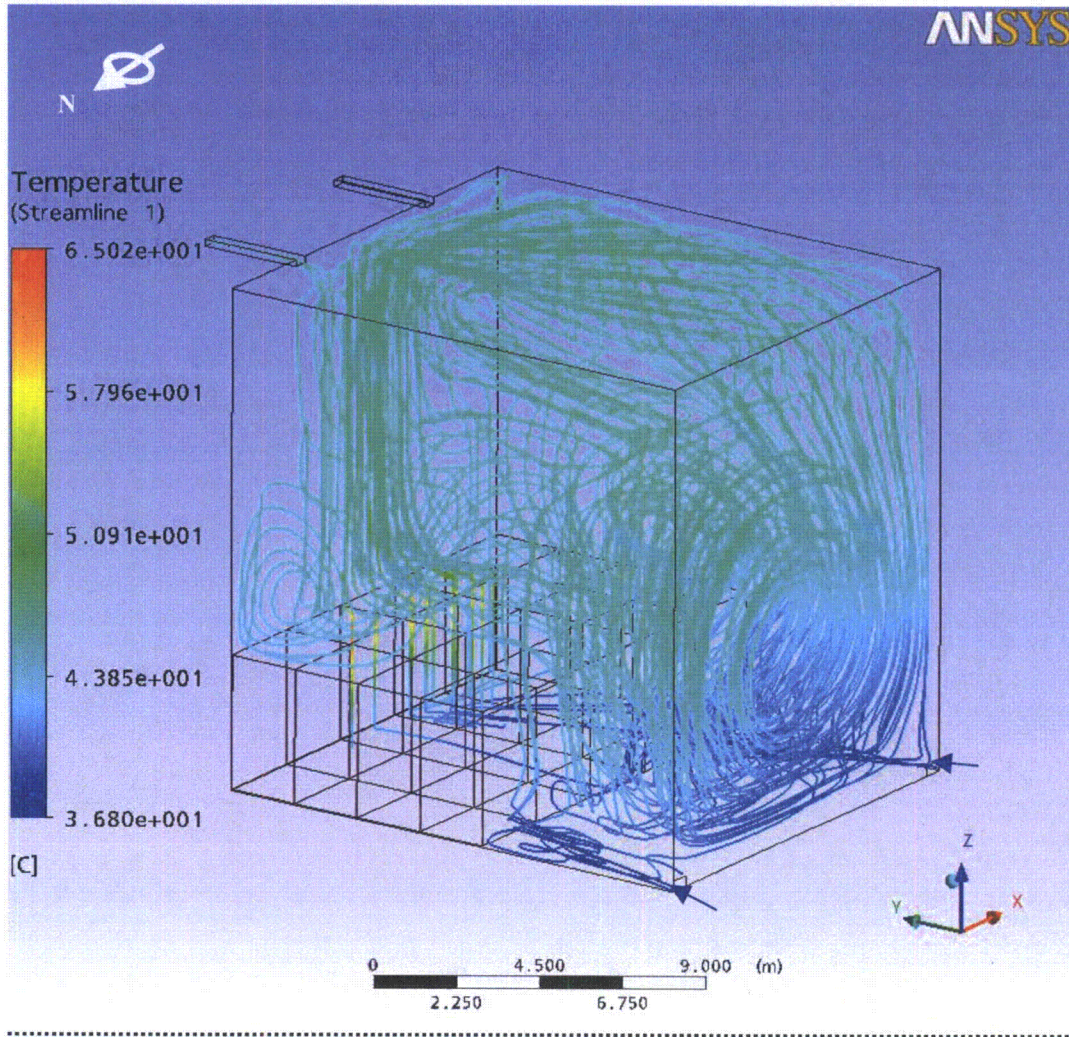
**Figure 5–7. Velocity under the Normal Conditions Case (y,z)**

Figure 5-7 shows the velocity distribution in the SFP under the normal conditions case. Velocities for horizontal planes at 3, 6, 9, & 12 metres high are shown. Natural convection is forcing a vertical flow from the racks with the highest heat load.



**Figure 5–8. Velocity under the Normal Conditions Case (y,z)**

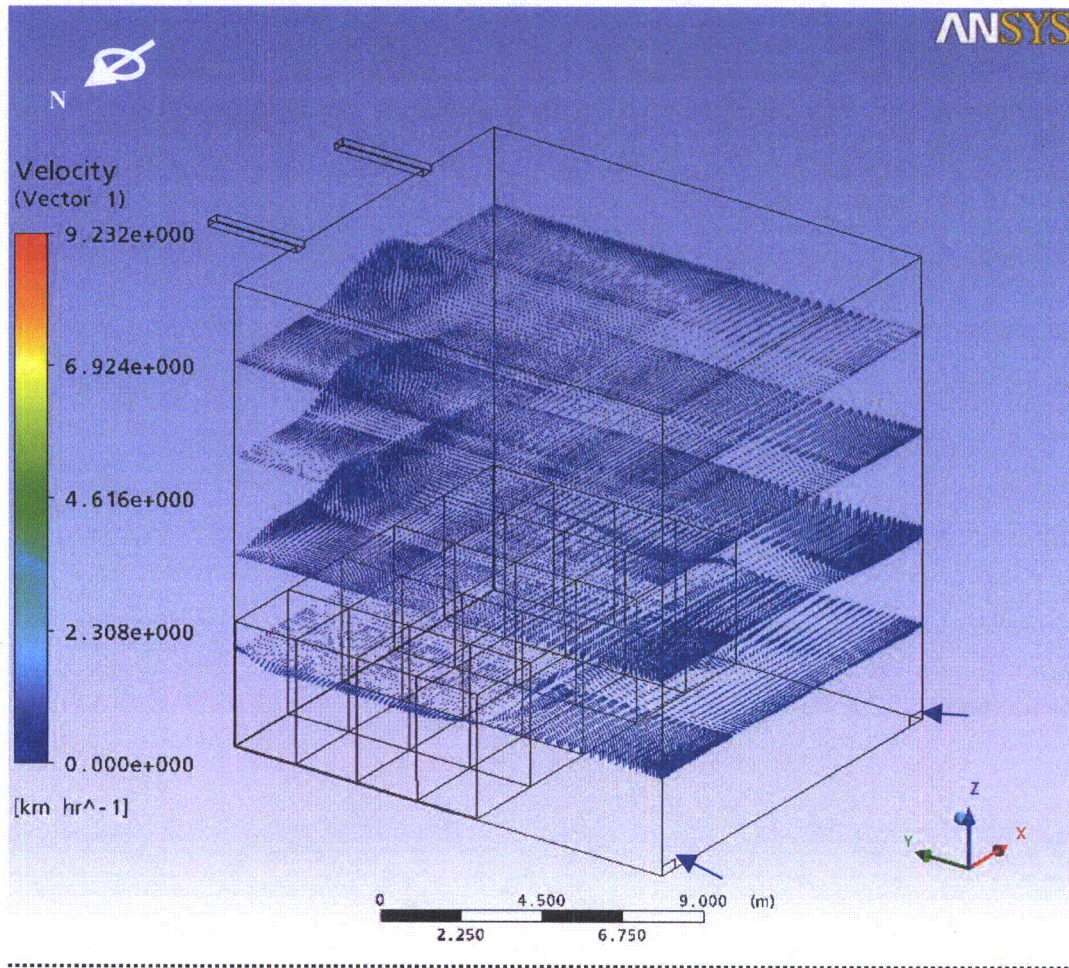
Figure 5-8 shows the velocity distribution in the SFP under the normal conditions case. For this figure vertical planes (y,z) have been selected.



**Figure 5-9. Streamlines from Inlets to Outlets under the Normal Conditions Case**

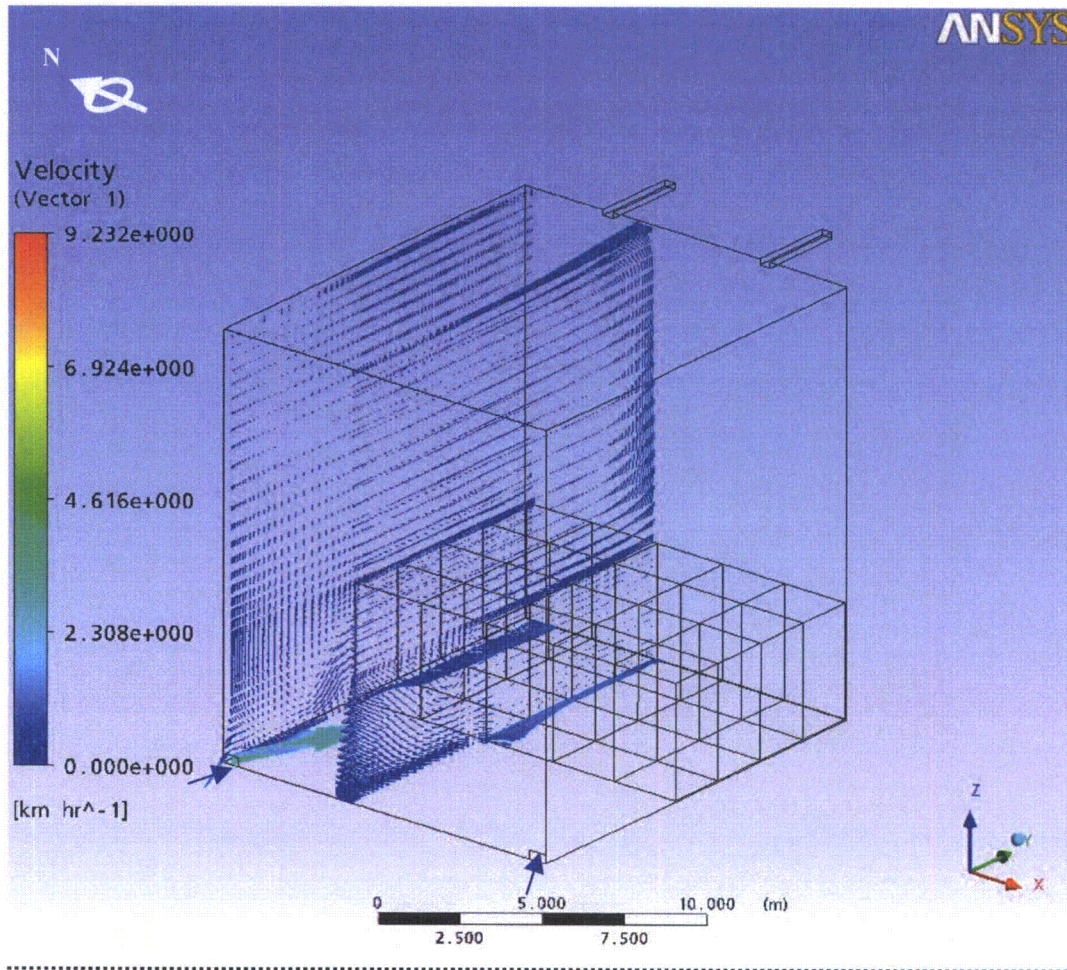
Figure 5-9 shows streamlines from the inlets and streamlines to the outlets in the SFP under the normal conditions case. The color of the streamline represents the temperature for each point. As each rack is modeled as an individual domain, and is independent of the fluid domain that is in the pool, flow through the rack is obscured from view in this streamline diagram. Evidence of water temperature increasing as it flows through the rack, from bottom to top, is seen in Figure 5-4.

**5.3.4 Velocity Distribution Under Abnormal Conditions Case**



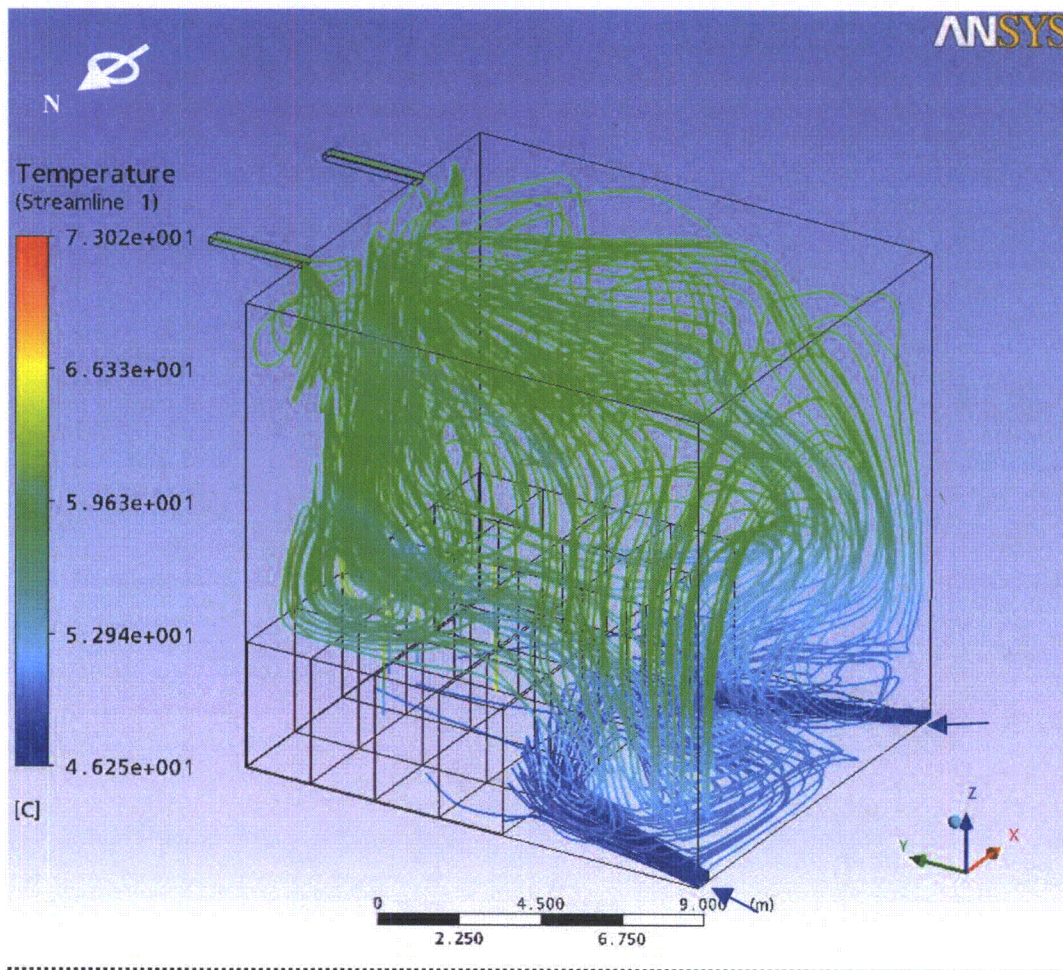
**Figure 5–10. Velocity under the Abnormal Conditions Case (y,z)**

Figure 5-10 shows the velocity distribution in the SFP under the abnormal conditions case. Velocities for horizontal planes at 3, 6, 9, & 12 metres high are shown. Natural convection is forcing a vertical flow from the racks with the highest heat load.



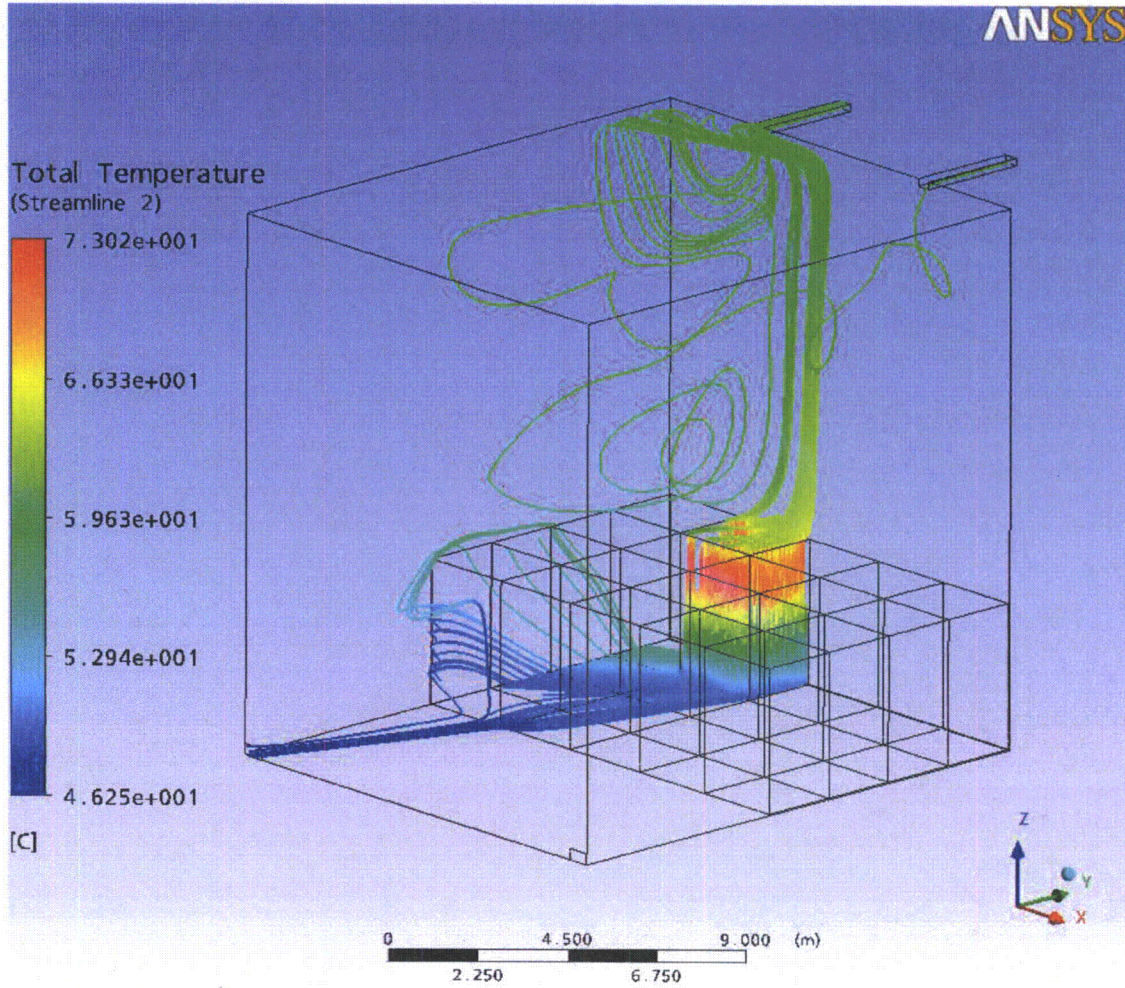
**Figure 5–11. Velocity under the Abnormal Conditions Case (y,z)**

Figure 5-11 shows the velocity distribution in the SFP under the abnormal conditions case. For this figure, vertical planes (y,z) have been selected.



**Figure 5–12. Streamlines from Inlets and to Outlets under the Abnormal Conditions Case**

Figure 5-12 shows streamlines from the inlets and streamlines to the outlets in the SFP under the abnormal conditions case. The color of the streamline represents the temperature for each point. As each rack is modeled as an individual domain, and is independent of the fluid domain that is in the pool, flow through the rack is obscured from view in this streamline diagram. Evidence of water temperature increasing as it flows through the rack, from bottom to top, is seen in Figure 5-6.



**Figure 5-12a. Stream Lines From Inlet #1 Through Rack #5**

Figure 5-12a shows a demonstration of the stream line flow when one of the rack domains is enabled in the model to show flow through the rack.

### 5.3.5 Maximum Cladding Temperature

In order to calculate the maximum fuel cladding temperature in the racks, the following assumptions are made:

- The worst case is assumed to be the case where higher temperatures are reached. This is the abnormal conditions case.
- The fuel rod heat emission rate includes a radial peaking factor value of 1.4.
- The axial power shape is assumed to be a cosine curve, as the axial heat dissipation in the rod is known to reach a maximum in the central region, and taper off at the two extremities.
- A safety factor of 1.2 is considered for the bundle heat load.

Making use of the conservation of energy for a differential piece of rod, an analytical model for the water and cladding temperature is produced. This highly conservative model leads to simple algebraic equations which directly give the maximum local cladding temperature. For added conservatism a foulant layer (crud deposit) is assumed on the cladding surface. Thermal resistance equal to 5673 W/m<sup>2</sup>°C (1000BTU/h ft<sup>2</sup>°F) (Reference 7) is assumed. Input data for this calculation is given in the table below.

Parameter	Value
Bundle generated heat (W)	1.2 x 8545.93W = 10255.12W
Radial peaking factor	1.4
No rods per bundle	92 (*)
Rod length (m)	3.3762m (*)
Water temperature at rod's inlet (°C)	56.38°C (**)
Cladding outside diameter (m)	10.26mm (*)
Pellet diameter (m)	8.76mm (*)
Zr-2 Conductivity (W/m°C)	23W / m°C @ 25°C 19W / m°C @ 300°C
Foulant layer heat transfer coefficient (W/m <sup>2</sup> °C)	5673.4W/m <sup>2</sup> °C
Total flow rate through the rack (15x12 bundle array)	13.87Kg/s (**)

(\*) Data taken from (Reference 6).

(\*\*) The inlet temperature and the total flow rate through the rack are taken from the CFD model solution for the worst case and the worst rack, where the maximum temperature is reached.

The governing equations are derived as follows. The volumetric heat generation in a rod is:

$$\int q^m(z) A_c dz = \frac{q(W)}{N_B}$$

$$q^m(z) = q_c^m \cdot \cos\left(\frac{\pi z}{H_e}\right)$$

$$q_c^m = \frac{\frac{q}{N_B}}{\int_{-H_e/2}^{H_e/2} \cos\left(\frac{\pi z}{H_e}\right) A_c dz} = \frac{\frac{q}{N_B}}{2 A_c \frac{H_e}{\pi}}$$

$$\frac{q_c^m A_c H_e}{\pi} = \frac{1}{2} \frac{q}{N_B}$$

Where:

- $N_B$  : Number of rods in each bundle (FA)
- $q$  : Volumetric heat generation rate per bundle (FA)
- $q_c^m$  : Volumetric heat generation rate per fuel rod
- $A_c = \pi R^2$  : Pellet cross section (m<sup>2</sup>)
- R: Pellet radio (m)
- $H_e$  : Rod length (m)

$$\frac{q_c^m A_c H_e}{\pi} = \frac{1}{2} \frac{q}{N_B} = \frac{1}{2} \frac{10255.1}{92} = 55.73W$$

$$q_c^m = \frac{\pi \cdot 55.73 \cdot 4}{\pi \cdot 0.00876^2 \cdot 3.3762} = 860489.73 \frac{W}{m^3}$$

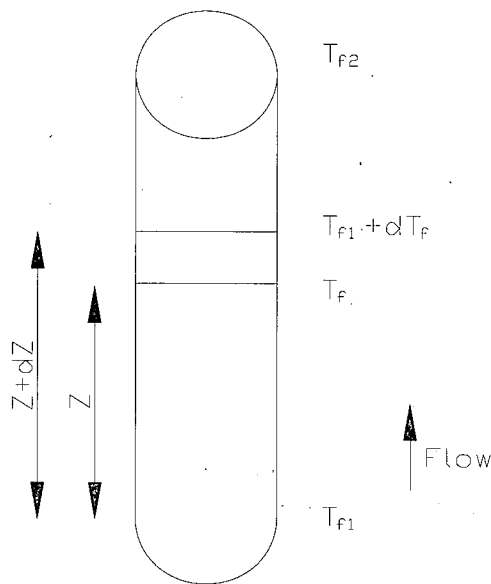


Figure 5-13. Rod Heat Balance

Applying the conservatism of energy between the fuel rod and the coolant, the following equation is obtained for the local fluid temperature.

$$m_{barra} C_p dT = q^m(z) A_c dz$$

$$T_f(z) = T_{f1} + \frac{q_c^m A_c}{m_{barra} C_p} \frac{H_e}{\pi} \left[ \sin \frac{\pi z}{H_e} + \sin \frac{\pi}{2} \right] = T_{f1} + \frac{1}{2} \frac{q}{m_{barra} C_p} \frac{N_B}{N_B} \left[ \sin \frac{\pi z}{H_e} + \sin \frac{\pi}{2} \right]$$

$$T_{c0}(z) = T_{f1} + \frac{q_c^m A_c}{m_{barra} C_p} \frac{H_e}{\pi} \left[ \sin \frac{\pi z}{H_e} + \sin \frac{\pi}{2} \right] + \frac{q_c^m \cos \frac{\pi z}{H_e} A_c}{h \cdot 2\pi(R+c)}$$

For added conservatism a foulant layer (crud deposit) is assumed on the cladding surface. This is equivalent to two thermal resistances in series, so the equation that gives the outside cladding temperature is:

$$T_{c0}(z) = T_{f1} + \frac{q_c^m A_c}{m_{barra} C_p} \frac{H_e}{\pi} \left[ \sin \frac{\pi z}{H_e} + \sin \frac{\pi}{2} \right] + \frac{q_c^m \cos \frac{\pi z}{H_e} A_c}{\left( \frac{h_{dep} h}{h_{dep} + h} \right) 2\pi(R+c)}$$

For the value of the inlet temperature ( $T_{f1}$ ), the maximum temperature of the inlet temperature to the worst rack in the worst case is selected. For the value of the coolant flow per rod, the average flow will be conservatively assumed.

Nomenclature used in preceding equations is:

$$m_{barra} = \frac{m_{rack}}{N_{EC} \cdot N_B} : \text{Coolant (water) flow rate per rod}$$

$m_{rack}$  : Coolant (water) flow rate in the rack

$N_{EC}$  : Number of bundles in the rack

$$C_p = 4182 \frac{J}{KgK} \text{ Coolant (water) specific heat}$$

$T_f(z)$  : Local fluid temperature

$h$ : Heat Transfer coefficient

$h_{dep}$  : Foulant layer heat transfer coefficient

$c$ : cladding thickness

$T_{co}$  : Outside cladding temperature

The minimum heat transfer coefficient from the following table is used (water, heating):

**Table 5-1**  
**Approximate Range of Values hm Ordinarily Encountered**

	Btu/(hr) (Sq ft) (Deg F)	
Steam, dropwise condensation	5,000	20,000
Steam, film-type condensation	1,000	3,000
Water boiling	300	9,000
Organic vapors condensing	200	400
Water, heating	50	3,000
Steam, superheating	5	20
Air, heating or cooling	0.2	10

(\*) Table taken from reference (Reference 7).

$$h = 50 \frac{BTU}{hr \cdot ft^2 \cdot F} = 283.9 \frac{W}{m^2 K}$$

$$T_{e0}(z) = 56.38 + \frac{55.73}{4182 \cdot \frac{13.87}{180 \cdot 92}} \left[ \sin \frac{\pi z}{3.3762} + 1 \right] + \frac{860489.73 \cos \frac{\pi z}{3.3762} \pi \frac{0.00876^2}{4}}{\left( \frac{5673.4 + 283.9}{5673.4 + 283.9} \right) 2\pi \left( \frac{0.01026}{2} \right)}$$

The maximum value calculated from this function is at  $z=1.3m$ , as measured from the center of the rod. The maximum peak temperature is:

$$T_{e0}(z) = 89.2^\circ C$$

### 5.3.6 Maximum Fluid Temperature Under 80% Blockage of Rack Outlet

Due to the different acceptance criteria for the two different cases, a calculation will be performed for each case.

#### 5.3.6.1 Under Normal Conditions Case

For this analysis the assumption is that the rack outlet is 80% blocked. Conservatively, the holes in the rack between bundles are not considered. A bundle in the hottest rack is considered for this case. The maximum temperature at the inlet of the hottest rack will be conservatively assumed. The flow for this bundle will be considered to be the average flow per bundle on this rack:

$$\dot{m}_{FA} = \frac{\dot{m}_{rack}}{N_{FA}} = \frac{27.867}{180} = 0.154816 \frac{Kg}{s}$$

Where:

$\dot{m}_{rack}$  = Total flow at the hottest rack inlet

$N_{FA}$  = Number of bundles in the hottest rack

The loss coefficient increment is given by the following equation:

$$\Delta K = \frac{1}{2} \left( \frac{1.5}{\rho \cdot A_B^2} - \frac{1}{\rho \cdot A_{CEL}^2} \right) = \frac{1}{2} \left( \frac{1.5}{1000 \cdot 0.2^2 \cdot (0.1646^2)} - \frac{1}{1000 \cdot (0.1646^2)^2} \right) = 24.862 Kg^{-1} m^{-1}$$

Where:

$A_B$  = Blocked section Area.

$A_{CEL}$  = Non blocked section Area.

$\rho$  = Fluid density.

Assuming the pressures at the inlet and outlet of the rack will be the same as if unblocked:

$$\Delta P = K_C (\dot{m}_{FA})^2 = K_{TAP} (\dot{m}_{FATAP})^2$$

Where:

$K_C$  = Loss coefficient without blockage

$K_{TAP}$  = Loss coefficient with blockage

$\dot{m}_{FA}$  = Flow through bundle without blockage

$\dot{m}_{FATAP}$  = Flow through bundle with blockage

The loss coefficient without blockage ( $K_C = 269.55 \text{Kg}^{-1} \text{m}^{-1}$ ) is equal to the value calculated in Section 5.2.3.1 of this report. The loss coefficient without blockage will be this value plus the loss coefficient due to the blockage. Therefore:

$$K_{TAP} = K_C + \Delta K = 269.55 + 24.862 = 294.41 \text{Kg}^{-1} \text{m}^{-1}$$

The flow through the blocked bundle can be obtained from the previous equations:

$$\dot{m}_{FABlock} = \dot{m}_{FA} \sqrt{\frac{K}{K + \Delta K}} = \frac{27.867}{15 \cdot 12} \sqrt{\frac{269.55}{294.41}} = 0.14813 \frac{\text{Kg}}{\text{s}}$$

The temperature that will be reached at the outlet of the bundle is:

$$T_{Block} = T_{f1} + \Delta T = T_{f1} + \frac{q}{\dot{m}_{FABlock} \cdot C_p} = 45.91 + \frac{16021 \cdot 1.2}{0.14813 \cdot 4182} = 76.94^\circ \text{C}$$

### 5.3.6.2 Under Abnormal Conditions Case

For this analysis, the assumption is that the rack outlet is 80% blocked. Conservatively, the holes in the rack between bundles are not considered. A bundle in the hottest rack is considered for this case. The maximum temperature at the inlet of the hottest rack will be conservatively assumed. The flow for this bundle will be considered to be the average flow per bundle on this rack:

$$\dot{m}_{FA} = \frac{\dot{m}_{rack}}{N_{FA}} = \frac{13.87}{180} = 0.077055 \frac{\text{Kg}}{\text{s}}$$

Where:

$\dot{m}_{rack}$  = Total flow at the hottest rack inlet

$N_{FA}$  = Number of bundles in the hottest rack

The loss coefficient increment is given by the following equation:

$$\Delta K = \frac{1}{2} \left( \frac{1.5}{\rho \cdot A_B^2} - \frac{1}{\rho \cdot A_{CEL}^2} \right) = \frac{1}{2} \left( \frac{1.5}{1000 \cdot 0.2^2 \cdot (0.1646^2)} - \frac{1}{1000 \cdot (0.1646^2)^2} \right) = 24.862 \text{Kg}^{-1} \text{m}^{-1}$$

Where:

$A_B$  = Blocked section Area.

$A_{CEL}$  = Non blocked section Area.

$\rho$  = Fluid density.

Assuming the pressures at the inlet and outlet of the rack will be the same as if it unblocked:

$$\Delta P = K_C (\dot{m}_{FA})^2 = K_{TAP} (\dot{m}_{FATAP})^2$$

Where:

$K_C$  = Loss coefficient without blockage

$K_{TAP}$  = Loss coefficient with blockage

$\dot{m}_{FA}$  = Flow through bundle without blockage

$\dot{m}_{FATAP}$  = Flow through bundle with blockage

The loss coefficient without blockage ( $K_C = 269.55 \text{Kg}^{-1} \text{m}^{-1}$ ) is equal as the value calculated in Section 5.2.3.1 of this report. The loss coefficient without blockage will be this value plus the loss coefficient due to the blockage. Therefore:

$$K_{TAP} = K_C + \Delta K = 269.55 + 24.862 = 294.41 \text{Kg}^{-1} \text{m}^{-1}$$

The flow through the blocked bundle can be obtained from the previous equations:

$$\dot{m}_{FABlk} = \dot{m}_{FA} \sqrt{\frac{K}{K + \Delta K}} = \frac{13.87}{15 \cdot 12} \sqrt{\frac{269.55}{294.41}} = 0.073730 \frac{\text{Kg}}{\text{s}}$$

The temperature that will be reached at the outlet of the bundle is:

$$T_{Blck} = T_{f1} + \Delta T = T_{f1} + \frac{q}{\dot{m}_{FABlk} \cdot C_p} = 56.38 + \frac{8545.93 \cdot 1.2}{0.07373 \cdot 4182} = 89.63^\circ \text{C}$$

## 5.4 REACTOR BUFFER POOL

The calculation methodology for this analysis is similar to that performed for the SFP.

The only time spent fuel can be stored in the buffer pool is during a refuelling outage. During an outage, one train of the fuel pool cooling system has the capacity to cool the entire SFP and is dedicated to that purpose. The redundant train provides cooling to the buffer pool.

The bulk temperature of the buffer pool is maintained below the same maximum value as the SFP (48.9 C, 120 F). The heat load in the buffer pool is 2.5 MW (Reference 10), compared to a heat load of 7.626 MW in the SFP. Each redundant train of the fuel pool cooling system is capable of removing 8.3 MW (Reference 1), therefore, the system is capable of maintaining buffer pool temperature below the maximum bulk temperature.

Since the inlet pipe is routed to the bottom of the racks in the deep pit of the buffer pool, the general configuration is similar to that in spent fuel pool. Therefore, with the cooling capacities being the same between the pools, the maximum temperature that would be reached at the exit of the spent fuel storage racks in the reactor buffer pool is calculated based on the ratio of the average per bundle heat load in the buffer pool to that of the SFP. The calculation below determines the temperature of fluid exiting the spent fuel storage racks in the buffer pool.

The heat per bundle in this pool would be:

$$\frac{2.5 \cdot 10^6 W}{2 \cdot 11.7 FA} = 16223.8 \frac{W}{FA}$$

That is similar to the heat per bundle in normal conditions case =  $16021 \frac{W}{FA_{new}}$

It is conservatively assumed that the flow for each bundle would be the same as the value used in the normal conditions case. The flow rate will actually be higher because cooling capacity for the racks in the reactor buffer pool is greater. Also, the heat load is higher; therefore, natural convection flow would be greater.

Because the temperature increment is proportional to the heat, the bulk temperature in the SFP and buffer pool is the same (48.9°C), and the coolant flow is the same, the exit temperature can be calculated as follows:

$$\frac{\Delta T_{RBP}}{\Delta T_{NCC}} = \frac{16223.8}{16021} = 1.01266$$

$$Rack\_Exit\_Temp = 65.83C \cdot 1.01266 = 66.7C$$

## 5.5 CONCLUSIONS

The results calculated in the previous sections show that the maximum local coolant temperature reached at the top of the racks in the SFP is 65.03°C under the normal conditions case. This is lower than 121°C, which is the maximum allowable temperature for this case. The maximum peak temperature reached is 73.03°C under the abnormal conditions case. This is lower than 121°C, which is the maximum allowable temperature for this case.

The results also show that the maximum peak cladding temperature that will be reached is 89.2°C.

In the event of 80% blockage at the outlet of the rack, the temperature reached in the normal conditions case would be 76.94°C. This is lower than 121°C, which is the maximum allowable temperature for this case. The temperature reached in the abnormal conditions case would be 89.63°C. This is lower than 121°C, which is the maximum allowable temperature for this case.

The maximum temperature of fluid exiting the spent fuel storage racks in the buffer pool is 66.7°C, which is below the maximum allowable temperature of 121°C.

In the current GE design for the spent fuel pool, the cold inlet water pipe is routed to the bottom of the pool, therefore, the water that cools the fuel elements can easily enter the bottom part of the racks. This inlet pipe design allows that the introduction of cold water at the bottom part of the racks eliminates the dependency of distances between racks or between racks and pool wall.

Based on the results above, there is no condition where water boils within the fuel storage racks, By extension, if convection boiling does not occur within the fuel storage racks, there is no possibility that nucleate boiling can occur.

Considering the variations determined in sensitivity studies, along with the significant margin between analyzed results and acceptance limits, it is concluded that the Spent Fuel Pool Storage Racks in the Spent Fuel Pool and the Reactor Buffer Pool are suitable for the intended duty under the conditions shown previously.

## 5.6 REFERENCES

1. "Fuel Storage Rack Design Specification" Document No 26A7032 Rev 04 GE Nuclear Energy.
2. ANSYS CFX Computer Program Release 11.0, ANSYS Inc., South Point, 275 Technology Dr., Canonsberg, PA 15317.
3. ESBWR Spent Fuel Pool Decay Heat Part II GE-NE-0000-0040-6730-R0-DRAFT Rev 0. GE Proprietary Information.
4. ESBWR Spent Fuel Pool Boil-off, eDRF 0000-0038-9391/neDRFSection 0000-0038-9392 Rev 02.
5. "Rack Layout at Spent Fuel Building" ENSA 5926.D100 Rev 01.
6. Design Study Summary GE14E, ESBWR Fuel Assembly, DRF Section 41-8790, Global Nuclear Fuel (GNF).
7. "Heat Transmission" William H. McAdams. McGraw-Hill Book Company.
8. "Fuel Storage Requirements" Doc. No 22A5866 Rev 08, GE Nuclear Energy.
9. "Rack Layout at Spent Fuel Building" ENSA 5926.D100 Rev 02.
10. ESBWR Buffer Pool Boil-Off and Makeup Capacity, eDRF Section 0000-0076-3483.
11. ESBWR Spent Fuel Pool Boil-off, eDRF Section 0000-0038-9392, Rev. 6.

## APPENDIX G – DISCUSSION OF ABNORMAL CONDITION HEAT LOAD AT 19.0 MW

### 1.0 DETERMINATION OF ABNORMAL CONDITION HEAT LOAD

The abnormal heat load of 17.3 MW, used in Section 5 of this report, represents the decay heat from the following:

- a) spent fuel from 10 years (5 cycles) of reactor operation, 36 days into the sixth cycle of plant operation and 5 days after shutdown, and
- b) offload of all fuel from the core to the spent fuel pool after 36 days of full power operation and 5 days after shutdown.

This heat load was determined not to be bounding, therefore, re-evaluation of the abnormal condition at a higher heat load is necessary.

An abnormal condition heat load of 19.0 MW is bounding, and is based on the following:

- a) spent fuel from 10 years (5 cycles) of reactor operation at the end of the sixth cycle (1.3 MW) and 5 days after shutdown\*,
- b) offload of all fuel from the core to the spent fuel pool at the end of the sixth cycle (16.8 MW) and 5 days after shutdown\*, and
- c) margin (0.9 MW).

\* This is conservative since SRP 9.1.3, Rev.1, specifies 150 hours (6.25 days).

An extremely conservative abnormal heat load case of 29 MW was analyzed with results presented in Appendix H. This analysis was based on the following:

- a) spent fuel from 10 years (5 cycles) of reactor operation at 80000 seconds (0.93 days) after reactor shutdown, and
- b) offload of all fuel from the core to the spent fuel pool at 80000 seconds (0.93 days) after reactor shutdown.

### 2.0 DISCUSSION OF ABNORMAL CONDITION HEAT LOAD OF 19.0 MW

The CFD model has not been modified and analysis has not been performed considering an abnormal condition heat load of 19.0 MW. However, given the results of analyses that have been performed at 17.3 MW and 29 MW, a case can be made that an abnormal condition heat load of 19.0 MW is bounded and fuel rack integrity is maintained. The impact on calculations using 19.0 MW is discussed below.

### 2.1 *Maximum Pool Inlet Temperature*

In section 5.2.2.2 of this report, the maximum pool inlet temperature is calculated to be 46.3°C for the 17.3 MW case. For the 29 MW case, the maximum pool inlet temperature is calculated to be 37.0°C.

Using 19.0 MW as an input with the same methodology used in the previous calculations, the maximum pool inlet temperature is calculated to be 45.0°C. This is an increase of 21.6% as compared to the 29 MW case.

Considering the model sensitivity presented in section 5.2.5 of this report, a 10% decrease in the maximum allowable pool inlet temperature corresponds with no greater than a 6% increase in rack exit temperature. An increase in the maximum allowable pool inlet temperature corresponds with a reduction in the calculated rack exit temperature. As the calculated pool inlet temperature for the 19.0 MW case is an increase over the pool inlet temperature for the 29 MW case, the rack exit temperature for the 19.0 MW case as compared with the 29 MW case will be reduced.

### 2.2 *Rack Exit Temperature*

The rack exit temperature acceptability limit is 121°C. In both the 17.3 MW and 29 MW cases, maximum rack exit temperatures are seen in the 15x12 racks filled with newly discharged fuel from the core; specifically rack R-9. The maximum rack exit temperature determined in the 29 MW case is 80.9°C.

For the 29 MW case, the heat load in each 15x12 rack filled with newly discharged fuel is calculated to be 3398692.58 W. Using 19.0 MW as an input with the same methodology used in the previous calculations, the heat load for each 15x12 rack filled with newly discharged fuel is calculated to be 2814480.0 W. As this heat load is less than the heat load from the 29 MW case, the conclusion can be made that the rack exit temperature for the 19.0 MW case is less than that for the 29 MW case.

### 2.3 *Maximum Cladding Temperature*

Per the summary tables in Section 5.3.5 of Section 5 and Appendix H, the input values for water temperature at rod inlet and rack flow rate used to calculate peak cladding temperature are outputs of the ANSYS analyses. As analysis for the 19.0 MW case was not performed, those values are not available to calculate an actual peak cladding temperature. It is anticipated that an actual peak cladding temperature for the 19.0 MW case will be less than that of the 29 MW case as the heat load per bundle and rod inlet temperature is less. However, in order to evaluate the peak cladding temperature for the 19.0 MW case, the conservative highlighted values in the following table are considered:

Heat Load Case	17.3 MW	29 MW
Rod (Rack) Inlet Temperature (°C)	56.38	<b>60.39</b>
Total Rack Flow Rate (Kg/s)	<b>13.87</b>	20.789
Peak Cladding Temperature (°C)	89.2	97.12

The same methodology was used to calculate the peak cladding temperatures for the 19.0 MW case as was used to calculate the values in the table. To determine a worst-case value for the 19.0 MW case, the 29 MW case rod inlet temperature and 17.3 MW case rack flow rate was used. This evaluation is considered worst-case as the maximum rod inlet temperature is used in combination with the minimum flow rate to produce the result. The resulting peak cladding temperature for the 19.0 MW case was calculated to be 101.0°C. As this value is below the boiling temperature of water at the depth of the top of the fuel racks (119°C), conventional boiling does not occur. Therefore, nucleate boiling is prevented.

### 3.0 CONCLUSIONS

Analyses for the 17.3 MW and 29 MW cases were performed using the same methodology and the same modeling software (ANSYS CFX 11.0). As can be seen in the summary tables in Section 5.2.4 of Section 5 and Appendix H, the inputs are the same, with the exceptions listed below:

- 1) Heat loads – 17.3 MW vs. 29 MW,
- 2) Parameters that were determined using the heat loads – The maximum pool inlet temperatures (Section 5.2.2 of Section 5 and Appendix H) were calculated using the normal and abnormal pool heat loads (see Section 2.1 above). Additionally, the heat load per fuel assembly and per fuel storage rack (Section 5.2.3.2 of Section 5 and Appendix H) was calculated using the normal and abnormal heat loads (see Section 2.2 above), and
- 3) Loss coefficient – The loss coefficient is calculated in Section 5.2.3.1 of Section 5 and Appendix H. For the 29 MW case (Appendix H), the loss coefficient was calculated to be 42.25668/m. For the 17.3 MW case, the loss coefficient was calculated to be 60.13/m.
- 4) Pool inlet locations and orientation – In Section 5.2.3 of Section 5 and Appendix H, the inlet locations are described. For the 17.3 MW case, the inlet locations are modeled at the bottom of each corner of the west wall with a 20° offset towards the middle. For the 29 MW case, the inlet locations are modeled at the bottom of each corner of the west wall with no offset. The explanation is also provided in each section that the actual inlet locations will be inboard from the corners, equally spaced between the pool walls. These modelling differences have negligible impact on analysis results, therefore, neither model was modified to reflect actual inlet locations and no adjustments to results are required in order to compare these cases with the 19.0 MW case.

Using the sensitivity information presented in Section 5.2.5 of this report, the rack exit temperature of 80.9°C for the 29 MW case will be considered for impact of differences in maximum pool inlet temperature and loss coefficient to be consistent with the 17.3 MW case. This adjustment will also be directly comparable to the 19 MW case.

An adjustment is required for the difference in the 29 MW vs. 17.3 MW case loss coefficients. The 29 MW case loss coefficient was calculated using area and length characteristics for fuel other than GE14E. This difference was non-conservative and was corrected for the 17.3 MW case, as the correct fuel length and cross-sectional area values for GE14E fuel were used. Considering loss coefficient sensitivity, an evaluation of the error in the 29 MW case shows that the temperature at the rack outlet would increase by 12.6%, from 80.9°C to 91.1°C. The basis for this value is the sensitivity discussion in Section 5.2.5, where a 20% increase in loss coefficient equates to no more than a 6% increase in rack exit temperature. The change in loss coefficient from 42.25668/m to 60.13/m is an increase of 42%, which represents a total temperature increase of 12.6%, or 10.2°C.

As there is an 8°C difference in the inlet temperatures between the 19.0 MW and 29 MW cases, a conservative and corresponding 8°C increase is considered for the rack exit temperature for the 29 MW case. When added to the adjusted temperature of 91.1°C calculated in the previous paragraph, the adjusted rack exit temperature for the 29 MW case is 99.1°C.

The 17.3 MW and 29 MW analyses are consistent in approach and adjustments were incorporated to reconcile any differences. Therefore, their use in evaluation of the 19.0 MW case is justified and the results are directly comparable.

Based on the results of the previous evaluations, it is concluded that an abnormal condition heat load of 19.0 MW in the spent fuel pool produces a rack exit temperature less than the adjusted rack exit temperature of 99.1°C determined for the 29.0 MW case. Therefore, the rack exit temperature acceptability limit of 121°C will not be exceeded, and significant margin still exists.

As no condition exists within the fuel assembly that causes conventional boiling, nucleate boiling is prevented.

## APPENDIX H – ANALYSIS AT A HEAT LOAD OF 29 MW

For the purpose of comparison with the 19.0 MW heat load evaluation, the analysis at a total spent fuel pool heat load of 29 MW is being included in this report. This information serves as a bounding case for the 19.0 MW evaluation.

The FAPCS will be designed for an abnormal heat load of 20.1 MW, which represents 20 years of spent fuel and a full core offload five days after reactor shutdown. This exceeds the 19.0 MW abnormal heat load for fuel rack evaluation, which represents 10 years of spent fuel and a full core offload five days after reactor shutdown.

### 5. THERMAL-HYDRAULIC ANALYSIS (29 MW CASE)

#### 5.1 INTRODUCTION

The purpose of this analysis is to determine the maximum peak temperatures that will be reached at the exit of the spent fuel racks in the spent fuel pool and the buffer pool in the ESBWR nuclear power station. Also analysis shall demonstrate that these fuel storage racks are designed such that nucleate boiling is prevented.

A Computational Fluid Dynamics (CFD) based method will be used for the spent fuel pool analysis. This will allow analysis of the behavior of the water within the pool and the temperatures that the water will reach.

##### 5.1.1 Inputs/Assumptions

1. There are two postulated scenarios to be evaluated for the spent fuel pool (SFP):
  - a. Normal Conditions
    - Heat Load = 10-year spent fuel accumulation = 7.626 MW (Ref. 1)
    - Maximum Pool Bulk Temperature = 48.9°C (120°F) (Ref.1)
    - Pool Cooling Rated Flow Rate = 545.1 m<sup>3</sup>/hr = 150.96 Kg/s (Ref. 1)
  - b. Abnormal Conditions:
    - Heat Load = 10-year spent fuel accumulation + full core offload  
= 29 MW (Ref. 1)
    - Maximum Pool Bulk Temperature = 60°C (Ref. 1)
    - Pool Cooling Rated Flow Rate = 1090.2 m<sup>3</sup>/hr = 301.92 Kg./s (Ref. 1)

2. For the purpose of this analysis, it is assumed that the FAPCS maintains the pool at a steady bulk temperature and always removes heat at the rate it is produced. This assumption simplifies the model into a steady-state analysis by avoiding bulk temperature transients.

## **5.2 CALCULATION METHODOLOGY**

### ***5.2.1 General Description***

The calculation methodology for this analysis consists of two phases.

#### **5.2.1.1 Pool Inlet Temperature Determination**

In order to model the fluid dynamics of the pool, it is necessary to determine the temperature of the cooled water being returned to the pool from the FAPCS. The pool inlet temperature will be back-calculated from the assumptions described in 5.1.1. Because this analysis assumes a steady-state condition where the pool bulk temperature is “locked in” at its maximum value, the temperature of the pool inlet water does not necessarily reflect the realistic capabilities of the FAPCS. To determine the maximum inlet temperature of the water in each of the cases, the following values are used: the maximum bulk temperature (also equivalent to the pool outlet temperature), the heat generated by the fuel elements, and the flow rate provided by the FAPCS. Although the calculated pool inlet temperature is not a realistic design parameter, it is conservative in the context of this analysis due to the higher-than-normal bulk pool temperature.

#### **5.2.1.2 Calculation of the Velocities and Temperatures within the Spent Fuel Pool (SFP)**

Once the model inputs have been determined, the calculation of the velocities and temperatures are performed using a CFD (Computational Fluid Dynamics) based method, in order to evaluate the bounding temperature profile within the SFP.

### ***5.2.2 Pool Inlet Temperature Determination***

In this section, the maximum pool inlet temperatures are calculated for the normal and abnormal conditions.

The normal condition analyzes the spent fuel from 10 years of plant operation, which is limited by the capacity of the initial configuration of fuel racks in the spent fuel pool. The abnormal condition analyzes the spent fuel from 10 years of plant operation plus a full core offload, which is also limited by the capacity of the initial configuration of fuel racks in the spent fuel pool.

### 5.2.2.1 Normal Conditions Case

The heat generated under normal conditions is 7.626 MW [Reference 3].

In the normal conditions case, the flow rate is 545.1m<sup>3</sup>/h=150.96Kg/s [Reference 1].

$$\Delta T = \frac{\text{Heat}}{C_p \cdot \text{Flow}} = \frac{7.626 \cdot 10^6 \text{ W}}{4182 \frac{\text{J}}{\text{Kg} \cdot \text{K}} \cdot 150.96 \frac{\text{Kg}}{\text{s}}} = 12.08 \text{ K}$$

Maximum Inlet Temperature

$$T_{in} = 48.9 - 12.08 = 36.8^\circ \text{ C}$$

Therefore, the maximum inlet temperature is 36.8°C for the normal conditions case.

### 5.2.2.2 Abnormal Conditions Case

The heat generated under abnormal conditions is 29 MW [Reference 4]. This is a very conservative assumption.

In the abnormal conditions case, the flow rate is 1090.2m<sup>3</sup>/h=301.92Kg/s [Reference 1].

$$\Delta T = \frac{\text{Heat}}{C_p \cdot \text{Flow}} = \frac{29 \cdot 10^6 \text{ W}}{4182 \frac{\text{J}}{\text{Kg} \cdot \text{K}} \cdot 301.92 \frac{\text{Kg}}{\text{s}}} = 22.97 \text{ K}$$

Maximum Inlet Temperature

$$T_{in} = 60 - 22.97 = 37.03^\circ \text{ C}$$

Therefore, the maximum inlet temperature is 37°C for the abnormal conditions case.

## 5.2.3 Calculation of the Velocities and Temperatures within the Spent Fuel Pool (SFP)

The calculation of the velocities and temperatures are performed using a CFD (Computational Fluid Dynamics) based method, ANSYS CFX 11.0 [Reference 2].

The Spent Fuel Pool (SFP) water has been modeled and the racks located in the SFP have been modeled as subdomains. In these subdomains a volumetric heat generation and a directional loss coefficient have been imposed (the heat generation for each rack is calculated in Sections 5.2.3.2 and 5.2.3.3 the directional loss coefficient is calculated in Section 5.2.3.1).

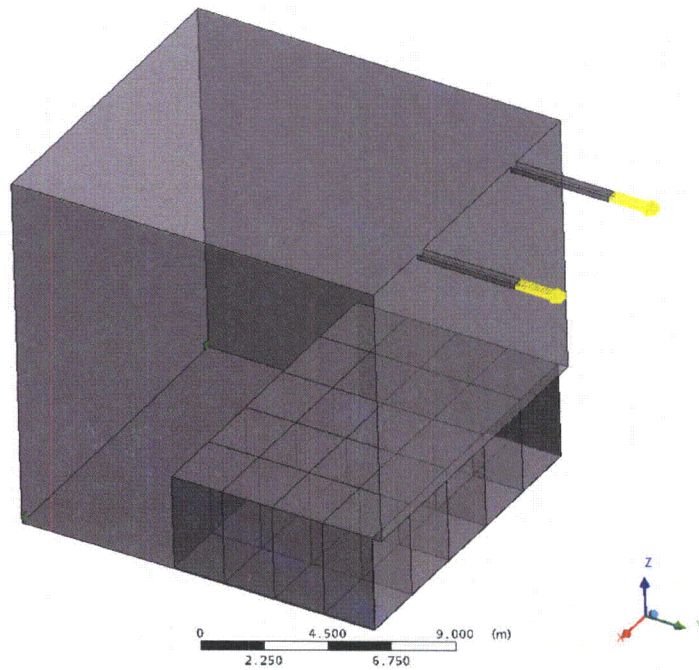


**Figure H5-1. SFP Model**

The rack layout modeled in Figure H5-1 represents the 10-year configuration [Reference 5]. Each of the 20 racks has an array of 15x12, for a total of 3600 storage spaces.

Two outlets have been modeled at the top of the SFP. Two inlet areas have been modeled at the bottom of the SFP in the corners opposite the racks. The actual inlet locations are inboard from the corners, equally spaced between the pool walls. As this difference from the modelled locations is considered to have negligible impact on results, the model was not modified to reflect the actual inlet locations.

A 42 mm gap between the racks and the northern and southern pool walls has been included in the model. No gap has been considered between the racks and the eastern pool wall. Nor was any gap considered between the racks. The gaps used in the model are conservative relative to actual design values.

#### 5.2.3.1 Loss Coefficient Calculation

Figure H5-2 [Reference 8] shows the loss coefficient in the vertical direction inside the racks. This curve is mathematically fit using the following parabolic expression:

$$y = ax^2 + bx + c$$

Where:

$y$  is the pressure drop (psi)

$x$  is the mass flow rate (lbm/hr)

Since there is no pressure drop when the mass flow rate is zero,  $c = 0$ . From the parabolic fitting, the coefficients values are:

$$b = 0$$

$$a = 6.2 \cdot 10^{-10} \text{ PSI} \frac{\text{hr}^2}{\text{LBM}^2} = 269.55 \frac{1}{\text{kg} \cdot \text{m}}$$

Thus, pressure loss can be represented by the following formula:

$$\Delta P = K \cdot (m)^2$$

From this figure loss coefficient K can be obtained:

$$K = 269.55 \text{ Kg}^{-1} \cdot \text{m}^{-1}$$

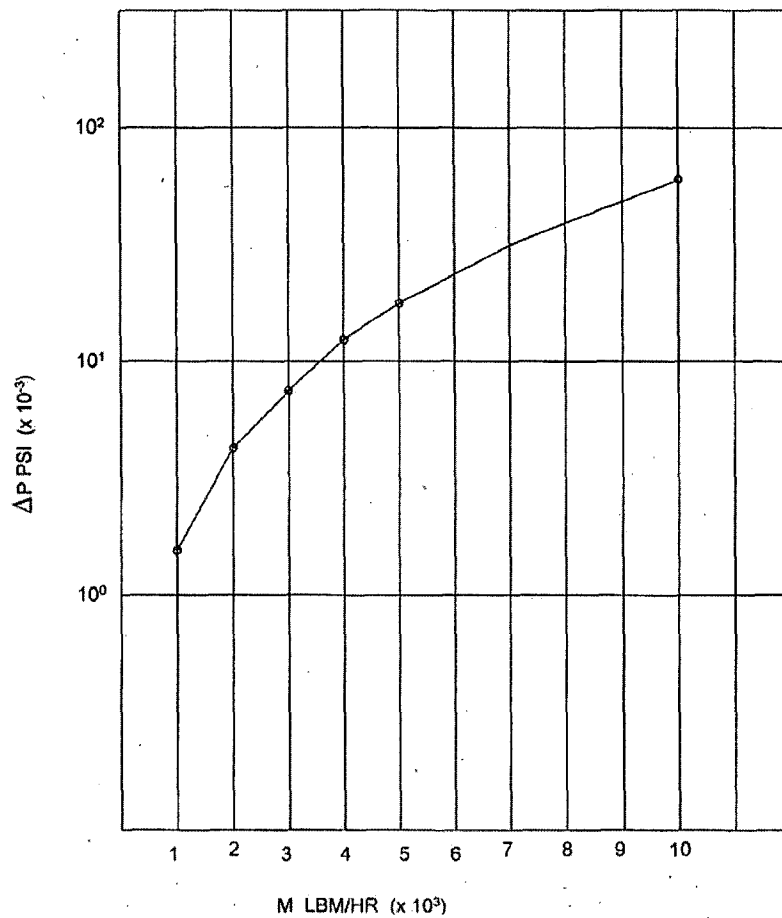


**Figure H5-2. Loss coefficient in Racks**

The CFD code requires that this loss coefficient be input as a function of velocity. Therefore, an additional calculation using the formula must be performed. An 8% safety factor has been applied to the loss coefficient obtained previously ( $K=269.55\text{Kg}^{-1}\cdot\text{m}^{-1}$ ).

$$K_N \cdot \rho \cdot L \cdot V^2 = K \cdot (m)^2$$

$$m = \rho \cdot V \cdot A$$

$$K_N = K \cdot \rho \cdot \frac{A^2}{L} = 269.55 \cdot 1.08 \cdot 1000 \cdot \frac{(0.1606^2)^2}{4.583} = 42.25668\text{m}^{-1}$$

This is the value used for all the racks in the model. To model vertical-only water movement inside the racks, the loss coefficient applied in the two horizontal directions (x, y) is assumed to be  $10^6$  times greater than in the vertical direction.

To simulate the heat generation produced by the Fuel Assemblies (FA) inside the racks, a volumetric heat generation has been applied to the subdomains. For conservatism, it has been assumed that all the new FA (the most active FA) are located together. The temperature reached with this configuration is greater than the temperature that would be reached if the new FA were distributed uniformly between all the racks in the SFP.

Next, the heat generation in each rack will be calculated for each case.

### 5.2.3.2 Heat Generation Calculation in Each Rack Under the Normal Conditions Case

The heat generated by the FA under the normal conditions case is = 7.626MW. For conservatism, it is assumed that all the heat is generated by the new FA.

$$\frac{7.626 \cdot 10^6 W}{476 FA_{new}} = 16021 \frac{W}{FA_{new}}$$

In reference to the FA distribution between the racks, the worst-case configuration has the new FA located in the racks farthest from the SFP inlet. The new FA will be located in the racks 5, 9 and 13.

$$\text{Heat generated in rack 5: } 180 FA_{New} \cdot 16021 \frac{W}{FA_{New}} = 2883780W$$

$$\text{Heat generated in rack 9: } 180 FA_{New} \cdot 16021 \frac{W}{FA_{New}} = 2883780W$$

$$\text{Heat generated in rack 13: } 7.626 \cdot 10^6 W - 2883780W - 2883780W = 1858440W$$

The rest of the racks do not have any heat generation applied.

5.2.3.3 Heat Generation Calculation in Each Rack Under the Abnormal Conditions Case

The heat generated by the FA under the abnormal conditions case is = 29MW. Of the 29MW considered, 7.626MW is attributed to the accumulation of 10-years of spent fuel. The remainder is attributed to a full core offload.

$$\frac{(29 - 7.626) \cdot 10^6 W}{1132FA_{new}} = 18881.6 \frac{W}{FA_{new}}$$

Fuel from a full core offload requires 6 complete racks and 52 storage spaces in a 7th rack. The heat generated by the accumulation of 10 years of spent fuel is divided among the remainder of storage capacity.

The hottest fuel assemblies are conservatively assumed to be located in the area receiving the least amount of cooling. These racks are 5, 6, 9, 10, 13, and 14.

$$\text{Heat generated in racks 5, 6, 9, 10, 13, and 14: } 180FA_{new} \cdot 18881.6 \frac{W}{FA_{new}} = 3398692.58W$$

$$\text{Heat generated in racks not completed by new FA: } \frac{7.626 \cdot 10^6}{14} = 544714.3W$$

$$\text{Heat generated in rack 11: } (29-7.626) \cdot 10^6 W - 6 \cdot 3398692.58W + 544714.3W = 1526558.8W$$

5.2.4 Summary Tables

The following tables show a summary of the model characteristics and the modeled fluid properties used.

**Model Characteristics**

Solver	CFX Serial Standard
Solver Advection Scheme	High Resolution
Simulation Type	Steady State
Bouyancy Option	Bouyant
Gavity direction	<0, 0, -9.81m/s2>
Bouyancy Ref. Temperature	60°C
Heat Transfer Option	Total Energy
Turbulence Option	k-Epsilon
Fluid	Liquid Water
	Density = 997 Kg/m3
	Dynamic Viscosity = 0.0008899 Kg/m s
	Specific Heat Capacity Cp = 4181.7 J/Kg°C
	Thermal Conductivity = 0.6069 W/m K
	Linear Variation of Density with Temperature

**Boundary Conditions**

<b>Normal Conditions</b>	<b>Abnormal Conditions</b>
In Flow Rate = 150.96 Kg/s 75.48 Kg/s (each inlet)	In Flow Rate = 301.92 Kg/s 150.96 Kg/s (each inlet)
Inlet Flow Direction = No offset upon entering the pool	Inlet Flow Direction = No offset upon entering the pool
Turbulence Intensity = 1%	Turbulence Intensity = 1%
Inlet Temperature = 36.8°C	Inlet Temperature = 37°C
Adiabatic Walls	Adiabatic Walls
Outlet Flow Rate 150.96 Kg/s (total of both outlets)	Outlet Flow Rate 301.92 Kg/s (total of both outlets)
Loss coeff = 42.2567/m	Loss coeff = 42.2567/m
Transverse Loss Coeff. Multiplier = 1000000	Transverse Loss Coeff. Multiplier = 1000000
Heat Generation as Section 5.2.3.2	Heat Generation as Section 5.2.3.3

**5.2.5 CFD Model Sensitivity**

CFD analysis methodology has been used in the past for other spent fuel pool thermal-hydraulic studies. The effect of hypothesis and assumptions, and also the modelling methodology (turbulence model selection, buoyancy treatment or mesh density) has been evaluated by sensitivity studies, according to the best practice guidelines for the use of CFD in nuclear reactor safety applications.

The sensitivity studies are presented in two parts: sensitivity to the numerical method and sensitivity to the mesh density.

Considering the numerical method, many parameters have been evaluated as shown below:

- Inlet mass flow rate increased by 10%
- Inlet temperature reduced by 10%
- Loss coefficient increased by 20%
- Turbulence model validated by a different model (k-ε model vs. SST-k-ω model)
- Reference temperature for buoyancy model reduced by 10%
- Turbulence intensity at the inlets increased by 9% (maximum allowed by the code)

The shape of the temperature distribution throughout the pool remains constant, with temperature variations (peak and bulk) of ≈ 1.5%. For variations of inlet mass flow rate, loss coefficient, and inlet temperature, the temperature variations (peak and bulk) are ≈ 4% to 6%. Inlet temperature refers to the maximum allowable pool inlet temperature. This value is dependent on the heat load in the pool, as the abnormal flow rate (301.92 Kg/s) and maximum bulk pool temperature (60°C) are analyzed as constant. As the heat load in the pool is increased, the corresponding rack exit temperature increases and the maximum allowable pool inlet temperature must decrease to maintain the bulk pool temperature. Conversely, as the heat load in the pool is decreased, the corresponding rack exit temperature decreases and the maximum allowable pool inlet temperature can increase to maintain the bulk pool temperature.

With regard to the sensitivity of mesh density, typically three cases are used for comparison: the original mesh density, a 50% increase over the original mesh density, and a 100% increase over the original mesh density. Specific examples from a specific thermal-hydraulic analysis of an operating BWR are presented below.

The temperature profiles and values of horizontal slices through the spent fuel pool are analyzed at various elevations for comparison purposes. In comparing the three models, the temperature distributions within the pools were constant and the bulk temperature variance for different locations was less than 2°C.

For the peak temperature value, the original mesh density model produced a result of 101.1°C. The 50% mesh density increase case produced a maximum peak temperature of 105.9°C. The doubled mesh density case produced a maximum peak temperature of 107.0°C. The maximum variation for peak temperature was 5.9°C.

Also a thermal-hydraulic analysis of a representative spent fuel pool has been modelled and solved by two different CFD codes. The shape of the temperature distribution throughout the pool is similar for both models.

The results of these sensitivity studies show that the hypothesis and numerical model to be valid.

### 5.3 RESULTS

Solving the two cases described previously, the results shown in the following sections are obtained.

#### 5.3.1 Temperature Distribution Under Normal Conditions Case

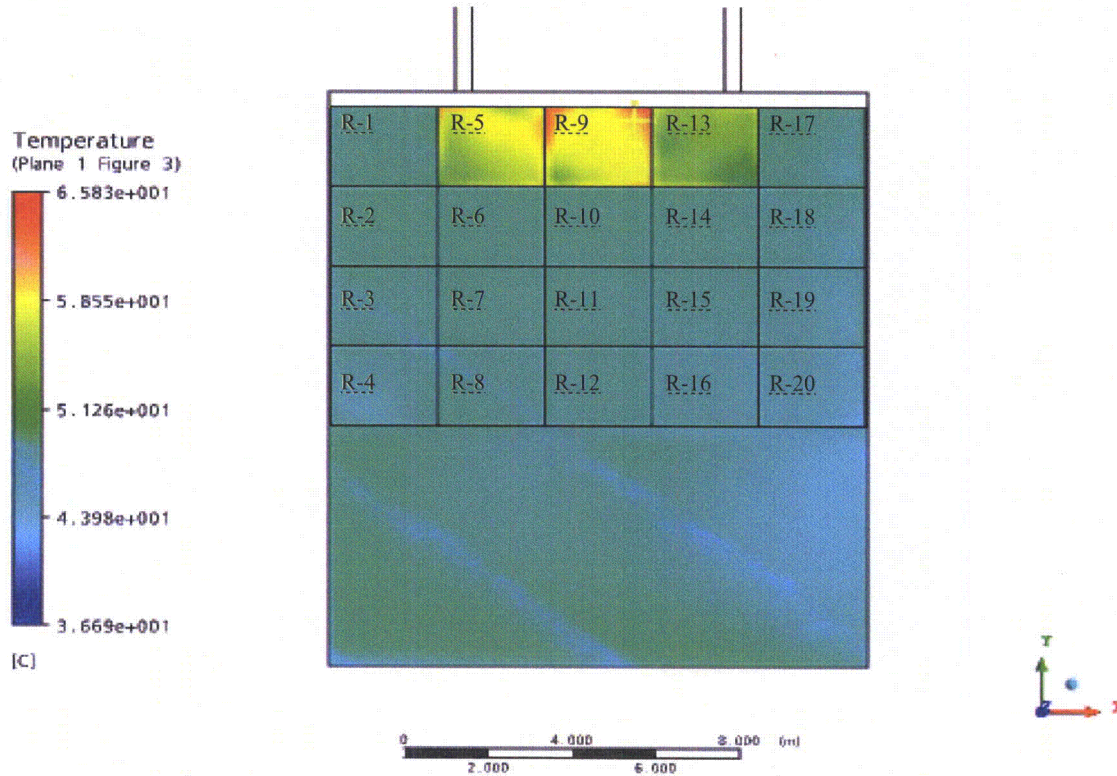
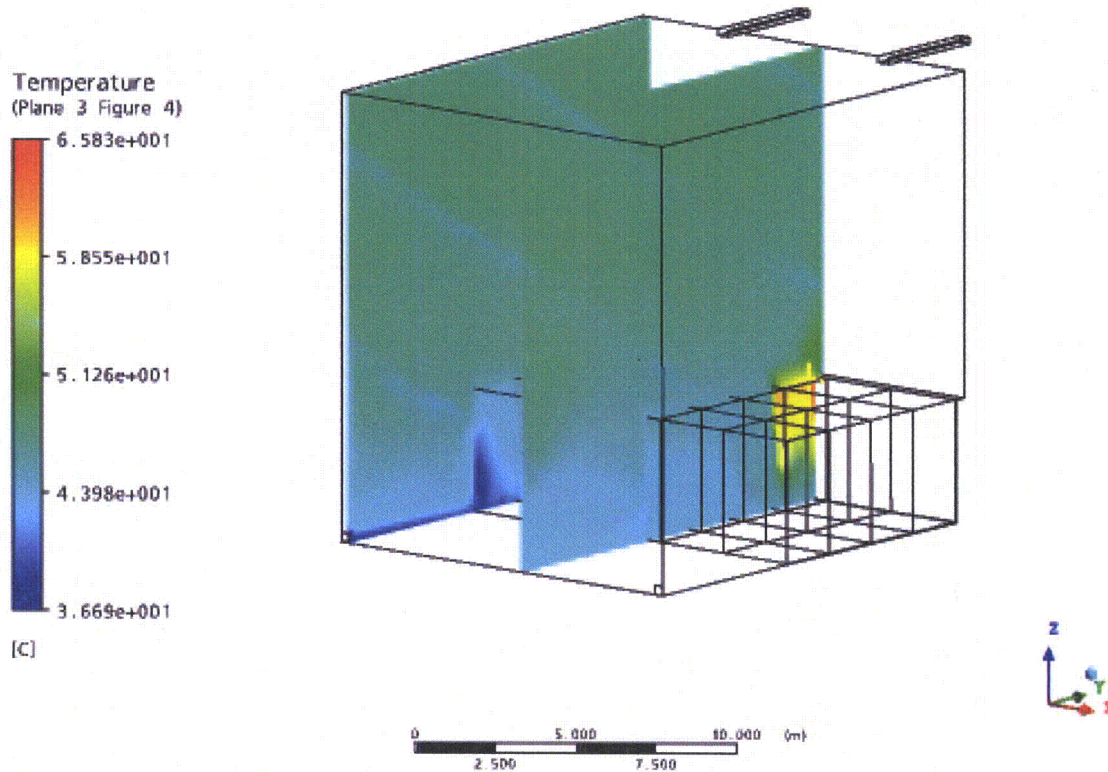


Figure H5-3. Temperature Distribution under the Normal Conditions Case (x,y)

Figure H5-3 shows the temperature distribution in the racks under the normal conditions case. The maximum peak temperature reached in this case is 65.83°C and is reached in the racks where the new FA are located. The maximum is reached at the top of the rack and is significantly less than the maximum allowable temperature of 121°C.



**Figure H5-4. Temperature Distribution under the Normal Conditions Case (y,z)**

Figure H5-4 shows the temperature distribution in the SFP under the normal conditions case. The temperature scale on the left ranges from the minimum to the maximum temperature on the SFP global. The inlet temperature (minimum temperature) is very close to 36.8°C. The outlet temperature is approximately 48.9°C as calculated in Section 5.2.2 of this analysis. The maximum temperatures are reached at the outlet of the racks where the new FA are located and the fluid temperature decreases as the water rises.

5.3.2 Temperature Distribution Under Abnormal Conditions Case

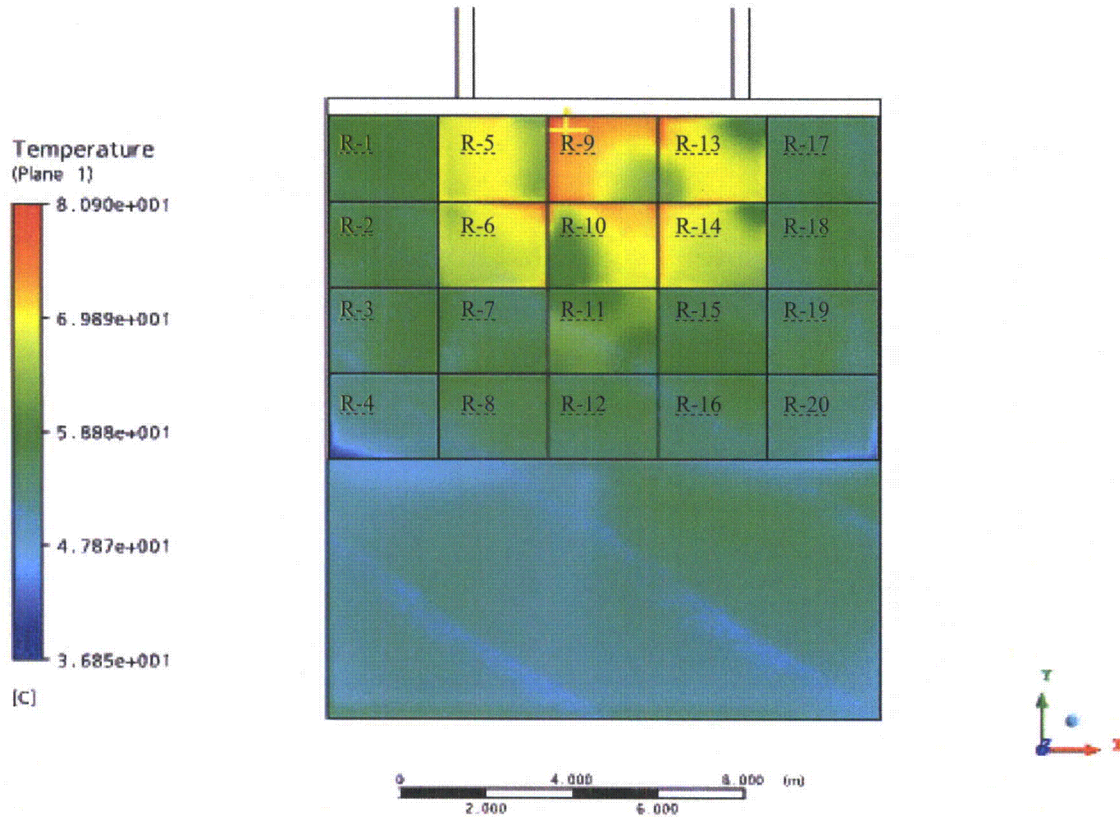
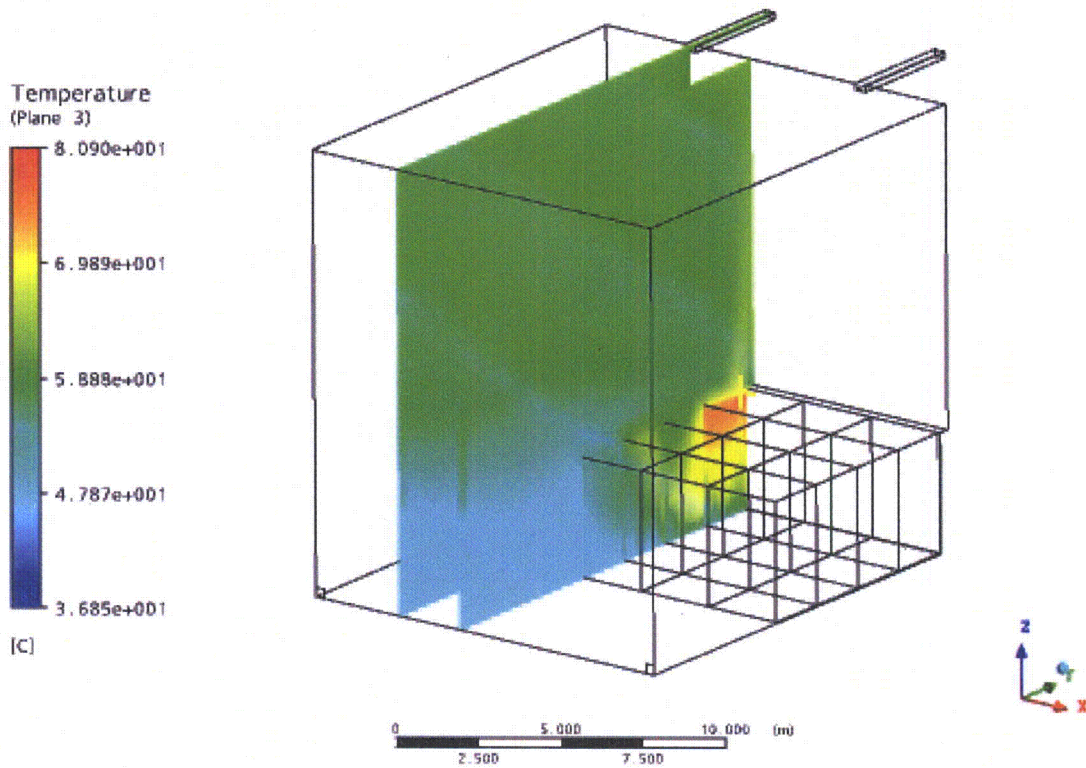


Figure H5-5. Temperature Distribution under the Abnormal Conditions Case (x,y)

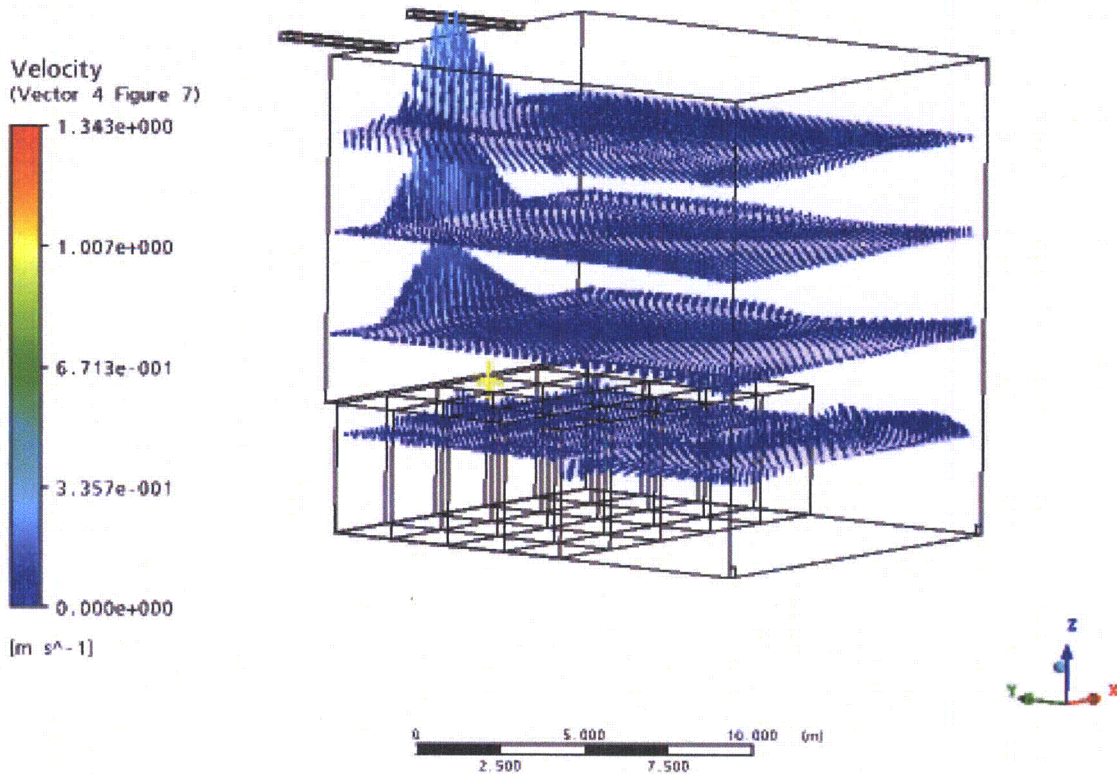
Figure H5-5 shows the temperature distribution in the racks under the abnormal conditions case. The maximum peak temperature reached in this case is 80.9°C and is reached in the racks where the new FA are located. The maximum is reached at the top of the rack and is significantly less than the maximum allowable temperature of 121°C.



**Figure H5-6. Temperature Distribution under the Abnormal Conditions Case (y,z)**

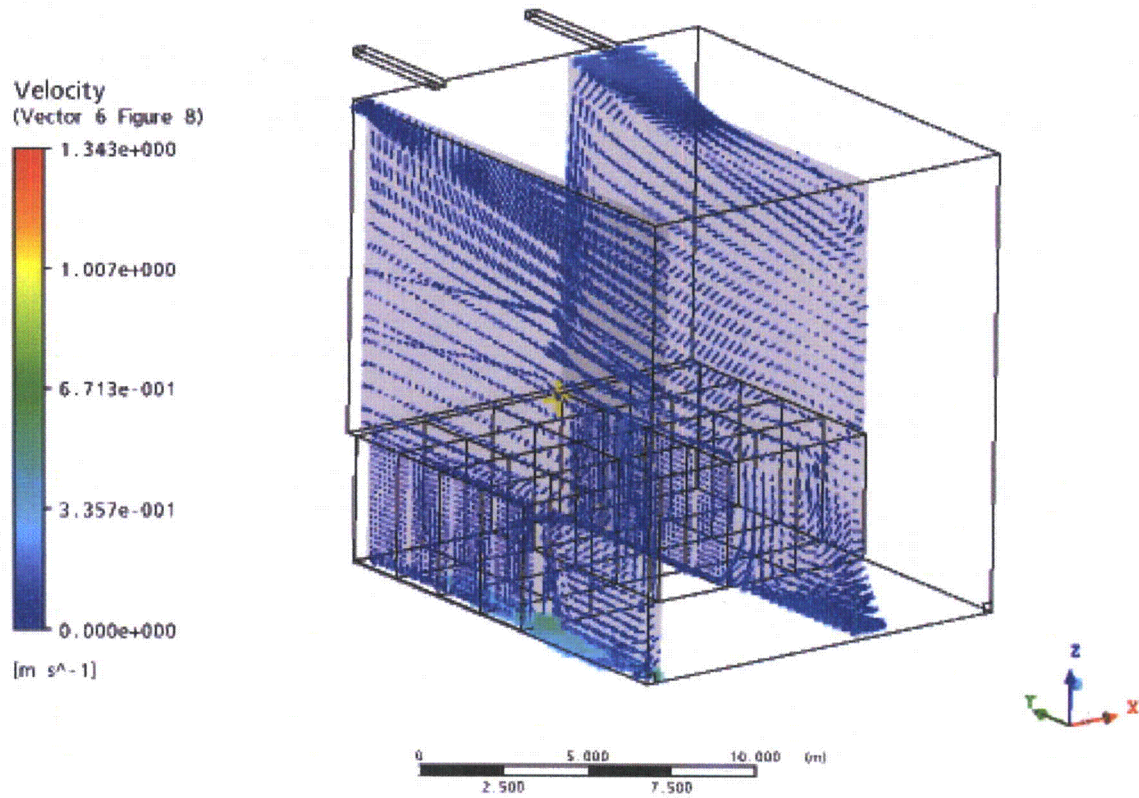
Figure H5-6 shows the temperature distribution in the SFP under the abnormal conditions case. The temperature scale on the left ranges from the minimum to the maximum temperature on the SFP global. The inlet temperature (minimum temperature) is very close to 37°C. The outlet temperature is approximately 60°C as calculated in Section 5.2.2 of this analysis. The maximum temperatures are reached at the outlet of the racks where the new FA are located and the fluid temperature decreases as the water rises.

**5.3.3 Velocity Distribution Under Normal Conditions Case**



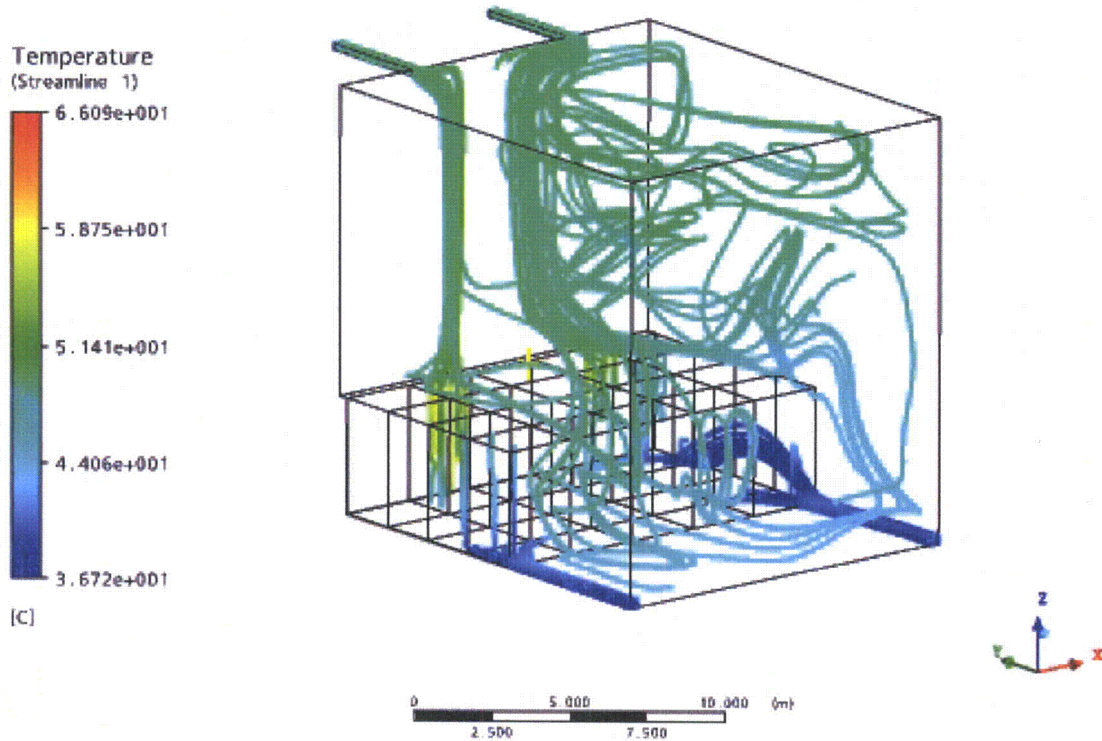
**Figure H5-7. Velocity under the Normal Conditions Case (x,y)**

Figure H5-7 shows the velocity distribution in the SFP under the normal conditions case. Velocities for horizontal planes at 3, 6, 9, 12 & 14 metres high are shown. Natural convection is forcing a vertical flow from the most loaded racks.



**Figure H5-8. Velocity under the Normal Conditions Case (y,z)**

Figure H5-8 shows the velocity distribution in the SFP under the normal conditions case. For this figure vertical planes (y,z) have been selected.



**Figure H5-9. Streamlines from Inlets and to Outlets under the Normal Conditions Case**

Figure H5-9 shows streamlines from the inlets and streamlines to the outlets in the SFP under the normal conditions case. The color of the streamline represents the temperature for each point.

### 5.3.4 Velocity Distribution Under Abnormal Conditions Case

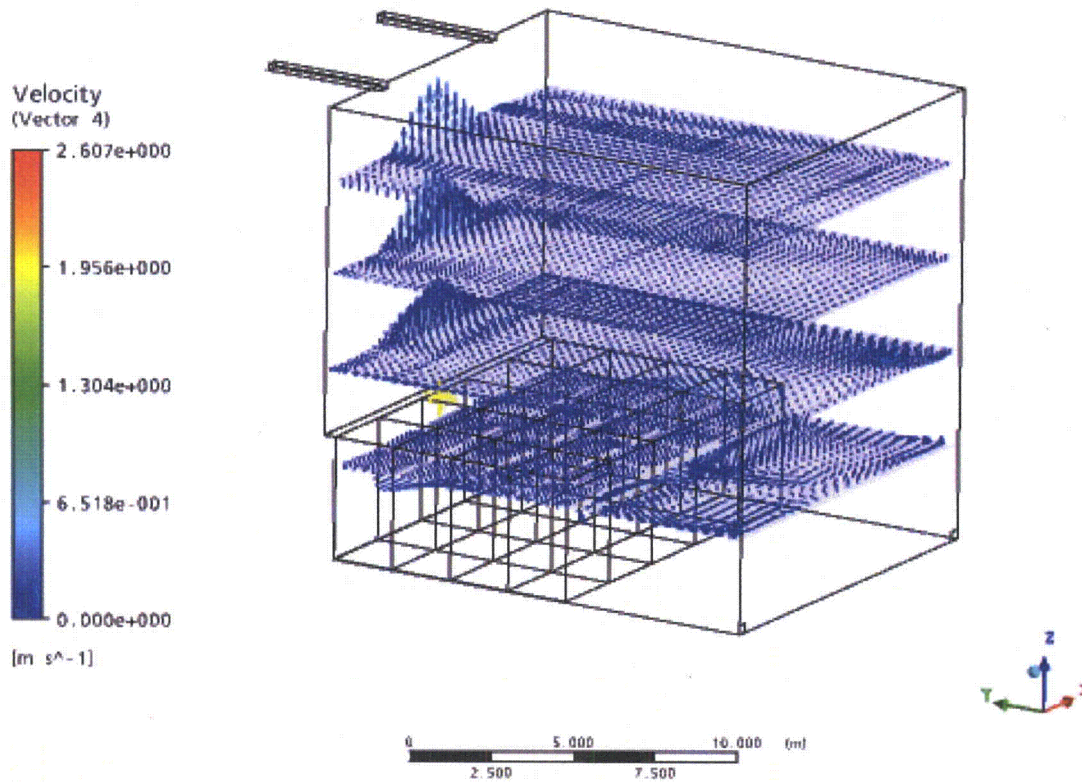
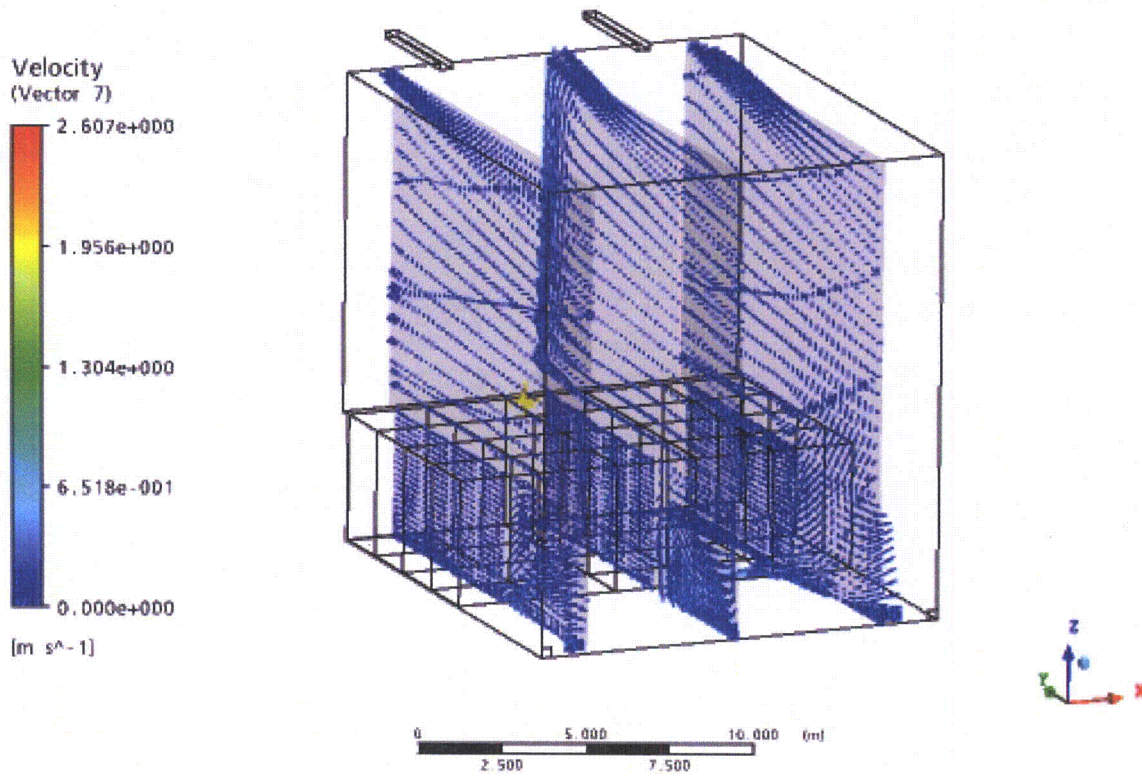


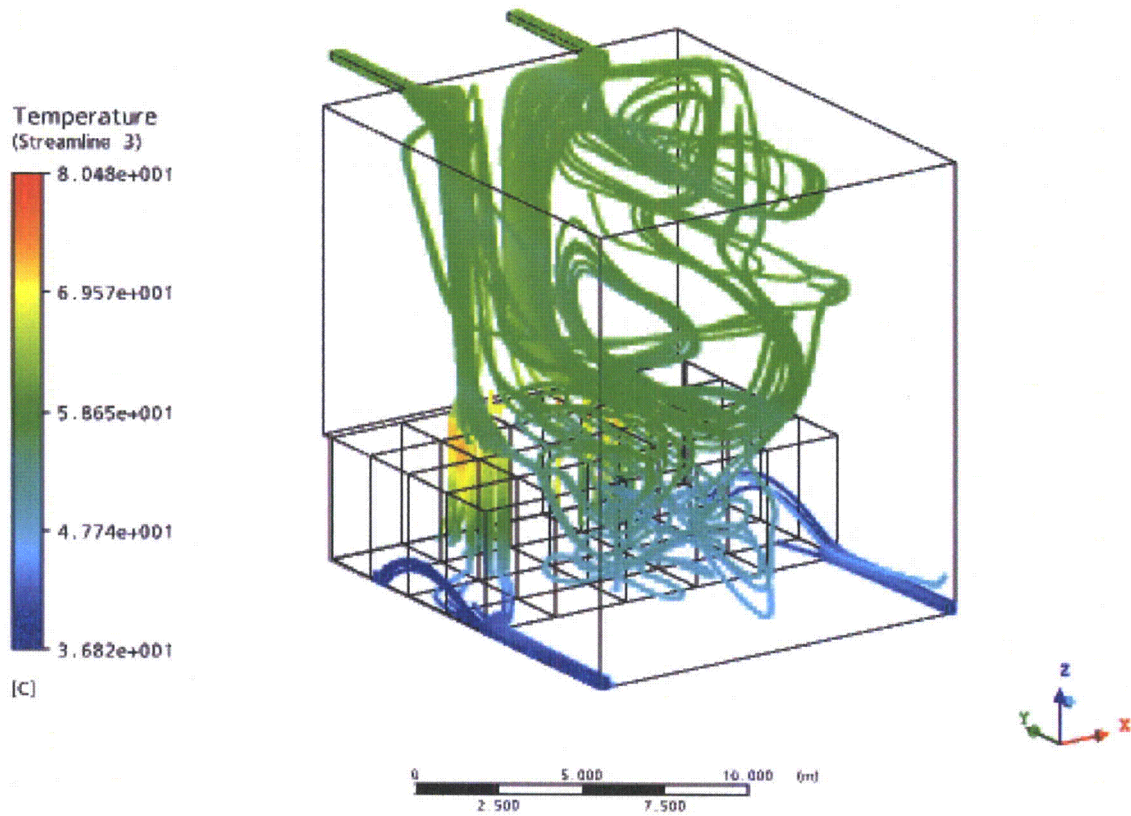
Figure H5-10. Velocity under the Abnormal Conditions Case (x,y)

Figure H5-10 shows the velocity distribution in the SFP under the abnormal conditions case. Velocities for horizontal planes at 3, 6, 9, 12 & 14 metres high are shown. Natural convection is forcing a vertical flow from the most loaded racks.



**Figure H5-11. Velocity under the Abnormal Conditions Case (y,z)**

Figure H5-11 shows the velocity distribution in the SFP under the abnormal conditions case. For this figure, vertical planes (y,z) have been selected.



**Figure H5-12. Streamlines from Inlets and to Outlets under the Abnormal Conditions Case**

Figure H5-12 shows streamlines from the inlets and streamlines to the outlets in the SFP under the abnormal conditions case. The color of the streamline represents the temperature for each point.

### 5.3.5 Maximum Cladding Temperature

In order to calculate the maximum fuel cladding temperature in the racks, the following assumptions are made:

- The worst case is assumed to be the case where higher temperatures are reached. This is the abnormal conditions case.
- The fuel rod heat emission rate includes a radial peaking factor value of 1.4.
- The axial power shape is assumed to be a cosine curve, as the axial heat dissipation in the rod is known to reach a maximum in the central region, and taper off at the two extremities.
- A safety factor of 1.2 is considered for the bundle heat load.

Making use of the conservation of energy for a differential piece of rod, an analytical model for the water and cladding temperature is produced. This highly conservative model leads to simple algebraic equations which directly give the maximum local cladding temperature. For added conservatism a foulant layer (crud deposit) is assumed on the cladding surface. Thermal resistance equal to 5673 W/m<sup>2</sup>°C (1000BTU/h ft<sup>2</sup>°F) [Reference 7] is assumed. Input data for this calculation is given in the table below.

Parameter	Value
Bundle generated heat (W)	1.2 x 18881.6W = 22657.92W
Radial peaking factor	1.4
No rods per bundle	92 (*)
Rod length (m)	3.3762m (*)
Water temperature at rod's inlet (°C)	60.39°C (**)
Cladding outside diameter (m)	10.26mm (*)
Pellet diameter (m)	8.76mm (*)
Zr-2 Conductivity (W/m°C)	23W / m°C a 25°C
	19W / m°C a 300°C
Foulant layer heat transfer coefficient (W/m <sup>2</sup> °C)	5673.4W / m <sup>2</sup> °C
Total flow rate through the rack (15x12 bundle)	20.789Kg/s (**)

(\*) Data taken from [Reference 6].

(\*\*) The inlet temperature and the total flow rate through the rack are taken from the CFD model solution for the worst case and the worst rack, where the maximum temperature is reached.

The governing equations are derived as follows. The volumetric heat generation in a rod is:

$$\int q^m(z) A_c dz = \frac{q(W)}{N_B}$$

$$q^m(z) = q_c^m \cdot \cos\left(\frac{\pi z}{H_e}\right)$$

$$q_c^m = \frac{\frac{q}{N_B}}{\int_{-H_e/2}^{H_e/2} \cos\left(\frac{\pi z}{H_e}\right) A_c dz} = \frac{\frac{q}{N_B}}{2 A_c \frac{H_e}{\pi}}$$

$$\frac{q_c^m A_c H_e}{\pi} = \frac{1}{2} \frac{q}{N_B}$$

Where:

- $N_B$  : Number of rods in each bundle (FA)
- $q$  : Volumetric heat generation rate per bundle (FA)
- $q_c^m$  : Volumetric heat generation rate per fuel rod
- $A_c = \pi R^2$  : Pellet cross section (m<sup>2</sup>)
- $R$  : Pellet radius (m)
- $H_e$  : Rod length (m)

$$\frac{q_c^m A_c H_e}{\pi} = \frac{1}{2} \frac{q}{N_B} = \frac{1}{2} \frac{22657.92}{92} = 123.14W$$

$$q_c^m = \frac{\pi \cdot 123.14 \cdot 4}{\pi \cdot 0.00876^2 \cdot 3.3762} = 1901191.35 \frac{W}{m^3}$$

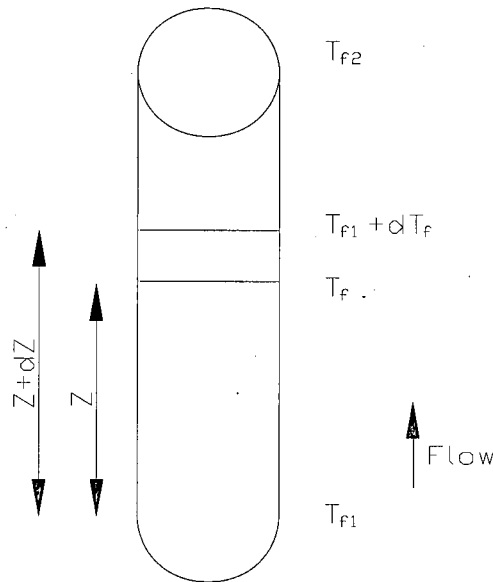


Figure H5-13. Rod Heat Balance

Applying the conservatism of energy between the fuel rod and the coolant, the following equation is obtained for the local fluid temperature.

$$m_{barra} C_p dT = q^m(z) A_c dz$$

$$T_f(z) = T_{f1} + \frac{q_c^m A_c}{m_{barra} C_p} \frac{H_e}{\pi} \left[ \sin \frac{\pi z}{H_e} + \sin \frac{\pi}{2} \right] = T_{f1} + \frac{1}{2} \frac{q}{m_{barra} C_p} \left[ \sin \frac{\pi z}{H_e} + \sin \frac{\pi}{2} \right]$$

$$T_{co}(z) = T_{f1} + \frac{q_c^m A_c}{m_{barra} C_p} \frac{H_e}{\pi} \left[ \sin \frac{\pi z}{H_e} + \sin \frac{\pi}{2} \right] + \frac{q_c^m \cos \frac{\pi z}{H_e} A_c}{h \cdot 2\pi (R+c)}$$

For added conservatism a foulant layer (crud deposit) is assumed on the cladding surface. This is equivalent to two thermal resistances in series, so the equation that gives the outside cladding temperature is:

$$T_{co}(z) = T_{f1} + \frac{q_c^m A_c}{m_{barra} C_p} \frac{H_e}{\pi} \left[ \sin \frac{\pi z}{H_e} + \sin \frac{\pi}{2} \right] + \frac{q_c^m \cos \frac{\pi z}{H_e} A_c}{\left( \frac{h_{dep} h}{h_{dep} + h} \right) 2\pi (R+c)}$$

For the value of the inlet temperature ( $T_{f1}$ ), the maximum temperature of the inlet temperature to the worst rack in the worst case is selected. For the value of the coolant flow per rod, the average flow will be conservatively assumed.

Nomenclature used in preceding equations is:

$$m_{barra} = \frac{m_{rack}}{N_{EC} \cdot N_B} : \text{Coolant (water) flow rate per rod}$$

$m_{rack}$  : Coolant (water) flow rate in the rack

$N_{EC}$  : Number of bundles in the rack

$$C_p = 4182 \frac{J}{KgK} \text{ Coolant (water) specific heat}$$

$T_f(z)$  : Local fluid temperature

$h$  : Heat Transfer coefficient

$h_{dep}$  : Foulant layer heat transfer coefficient

$c$  : cladding thickness

$T_{co}$  : Outside cladding temperature

The minimum heat transfer coefficient from the following table is used (water, heating):

**Table H5-1**  
**Approximate Range of Values hm Ordinarily Encountered**

	[[Btu/(hr) (Sq ft) (Deg F)	
Steam, dropwise condensation	5,000	20,000
Steam, film-type condensation	1,000	3,000
Water boiling	300	9,000
Organic vapors condensing	200	400
Water, heating	50	3,000
Steam, superheating	5	20
Air, heating or cooling	0.2	10

(\*) Table taken from reference [Reference 7].

$$h = 50 \frac{BTU}{hr \cdot ft^2 \cdot F} = 283.9 \frac{W}{m^2 K}$$

$$T_{e0}(z) = 60.3 + \frac{123.14}{4182 \cdot \frac{20.789}{180.92}} \left[ \sin \frac{\pi z}{3.3762} + 1 \right] + \frac{1901191.35 \cos \frac{\pi z}{3.3762} \pi \frac{0.00876^2}{4}}{\left( \frac{5673.4 \cdot 283.9}{5673.4 + 283.9} \right) \cdot 2\pi \left( \frac{0.01026}{2} \right)}$$

The maximum value calculated from this function is at  $z=0.949m$ , as measured from the center of the rod. The maximum peak temperature is:

$$T_{e0}(z) = 97.12^\circ C$$

### 5.3.6 Maximum Fluid Temperature Under 80% Blockage of Rack Outlet

Due to the different acceptance criteria for the two different cases, a calculation will be performed for each case.

#### 5.3.6.1 Under Normal Conditions Case

For this analysis the assumption is that the rack outlet is 80% blocked. Conservatively, the holes in the rack between bundles are not considered. A bundle in the hottest rack is considered for this case. The maximum temperature at the inlet of the hottest rack will be conservatively assumed. The flow for this bundle will be considered to be the average flow per bundle on this rack:

$$\dot{m}_{FA} = \frac{\dot{m}_{rack}}{N_{FA}} = \frac{51.8178}{180} = 0.28787 \frac{Kg}{s}$$

Where:

$\dot{m}_{rack}$  = Total flow at the hottest rack inlet

$N_{FA}$  = Number of bundles in the hottest rack

The loss coefficient increment is given by the following equation:

$$\Delta K = \frac{1}{2} \left( \frac{1.5}{\rho \cdot A_B^2} - \frac{1}{\rho \cdot A_{CEL}^2} \right) = \frac{1}{2} \left( \frac{1.5}{1000 \cdot 0.2^2 \cdot (0.1646^2)} - \frac{1}{1000 \cdot (0.1646^2)^2} \right) = 24.862 Kg^{-1} m^{-1}$$

Where:

$A_B$  = Blocked section Area.

$A_{CEL}$  = Non blocked section Area.

$\rho$  = Fluid density.

Assuming the pressures at the inlet and outlet of the rack will be the same as if unblocked:

$$\Delta P = K_C (\dot{m}_{FA})^2 = K_{TAP} (\dot{m}_{FATAP})^2$$

Where:

$K_C$  = Loss coefficient without blockage

$K_{TAP}$  = Loss coefficient with blockage

$\dot{m}_{FA}$  = Flow through bundle without blockage

$\dot{m}_{FATAP}$  = Flow through bundle with blockage

The loss coefficient without blockage ( $K_C = 269.55 \text{Kg}^{-1} \text{m}^{-1}$ ) is equal to the value calculated in Section 5.2.3.1 of this report. The loss coefficient without blockage will be this value plus the loss coefficient due to the blockage. Therefore:

$$K_{TAP} = K_C + \Delta K = 269.55 + 24.862 = 294.41 \text{Kg}^{-1} \text{m}^{-1}$$

The flow through the blocked bundle can be obtained from the previous equations:

$$\dot{m}_{FABlock} = \dot{m}_{FA} \sqrt{\frac{K}{K + \Delta K}} = \frac{518178}{15 \cdot 12} \sqrt{\frac{269.55}{294.41}} = 0.27545 \frac{\text{Kg}}{\text{s}}$$

The temperature that will be reached at the outlet of the bundle is:

$$T_{Block} = T_{f1} + \Delta T = T_{f1} + \frac{q}{\dot{m}_{FABlock} \cdot C_p} = 48.17 + \frac{16021 \cdot 1.2}{0.27545 \cdot 4182} = 64.86^\circ \text{C}$$

### 5.3.6.2 Under Abnormal Conditions Case

For this analysis, the assumption is that the rack outlet is 80% blocked. Conservatively, the holes in the rack between bundles are not considered. A bundle in the hottest rack is considered for this case. The maximum temperature at the inlet of the hottest rack will be conservatively assumed. The flow for this bundle will be considered to be the average flow per bundle on this rack:

$$\dot{m}_{FA} = \frac{\dot{m}_{rack}}{N_{FA}} = \frac{30.452}{180} = 0.169178 \frac{\text{Kg}}{\text{s}}$$

Where:

$\dot{m}_{rack}$  = Total flow at the hottest rack inlet

$N_{FA}$  = Number of bundles in the hottest rack

The loss coefficient increment is given by the following equation:

$$\Delta K = \frac{1}{2} \left( \frac{1.5}{\rho \cdot A_B^2} - \frac{1}{\rho \cdot A_{CEL}^2} \right) = \frac{1}{2} \left( \frac{1.5}{1000 \cdot 0.2^2 \cdot (0.1646^2)^2} - \frac{1}{1000 \cdot (0.1646^2)^2} \right) = 24.862 \text{Kg}^{-1} \text{m}^{-1}$$

Where:

$A_B$  = Blocked section Area.

$A_{CEL}$  = Non blocked section Area.

$\rho$  = Fluid density.

Assuming the pressures at the inlet and outlet of the rack will be the same as if it unblocked:

$$\Delta P = K_C (\dot{m}_{FA})^2 = K_{TAP} (\dot{m}_{FATAP})^2$$

Where:

$K_C$  = Loss coefficient without blockage

$K_{TAP}$  = Loss coefficient with blockage

$\dot{m}_{FA}$  = Flow through bundle without blockage

$\dot{m}_{FATAP}$  = Flow through bundle with blockage

The loss coefficient without blockage ( $K_C = 269.55 \text{Kg}^{-1} \text{m}^{-1}$ ) is equal as the value calculated in Section 5.2.3.1 of this report. The loss coefficient without blockage will be this value plus the loss coefficient due to the blockage. Therefore:

$$K_{TAP} = K_C + \Delta K = 269.55 + 24.862 = 294.41 \text{Kg}^{-1} \text{m}^{-1}$$

The flow through the blocked bundle can be obtained from the previous equations:

$$\dot{m}_{FABlock} = \dot{m}_{FA} \sqrt{\frac{K}{K + \Delta K}} = \frac{30.452}{15 \cdot 12} \sqrt{\frac{269.55}{294.41}} = 0.1618776 \frac{\text{Kg}}{\text{s}}$$

The temperature that will be reached at the outlet of the bundle is:

$$T_{Block} = T_{f1} + \Delta T = T_{f1} + \frac{q}{\dot{m}_{FABlock} \cdot C_p} = 60.39 + \frac{18881.6 \cdot 1.2}{0.1618776 \cdot 4182} = 93.86^\circ \text{C}$$

#### 5.4 REACTOR BUFFER POOL

The calculation methodology for this analysis is similar to that performed for the SFP.

The only time spent fuel can be stored in the buffer pool is during a refuelling outage. During an outage, one train of the fuel pool cooling system has the capacity to cool the entire SFP and is dedicated to that purpose. The redundant train provides cooling to the buffer pool.

The bulk temperature of the buffer pool is maintained below the same maximum value as the SFP (48.9°C, 120°F). The heat load in the buffer pool is 2.5 MW [Reference 10], compared to a heat load of 7.626 MW in the SFP. Each redundant train of the fuel pool cooling system is capable of removing 8.3 MW [Reference 1], therefore, the system is capable of maintaining buffer pool temperature below the maximum bulk temperature.

Since the inlet pipe is routed to the bottom of the racks in the deep pit of the buffer pool, the general configuration is similar to that in spent fuel pool. Therefore, with the cooling capacities being the same between the pools, the maximum temperature that would be reached at the exit of the spent fuel storage racks in the reactor buffer pool is calculated based on the ratio of the

average per bundle heat load in the buffer pool to that of the SFP. The calculation below determines the temperature of fluid exiting the spent fuel storage racks in the buffer pool.

The heat per bundle in this pool would be:

$$\frac{2.5 \cdot 10^6 W}{2 \cdot 11 \cdot 7 FA} = 16223.8 \frac{W}{FA}$$

That is similar to the heat per bundle in normal conditions case =  $16021 \frac{W}{FA_{new}}$

It is conservatively assumed that the flow for each bundle would be the same as the value used in the normal conditions case. The flow rate will actually be higher because cooling capacity for the racks in the reactor buffer pool is greater. Also, the heat load is higher; therefore, natural convection flow would be greater.

Because the temperature increment is proportional to the heat, the bulk temperature in the SFP and buffer pool is the same (48.9°C), and the coolant flow is the same, the exit temperature can be calculated as follows:

$$\frac{\Delta T_{RBP}}{\Delta T_{NCC}} = \frac{16223.8}{16021} = 1.01266$$

$$Rack\_Exit\_Temp = 65.83C \cdot 1.01266 = 66.7C$$

## 5.5 SUMMARY OF RESULTS

The results calculated in the previous sections show that the maximum local coolant temperature reached at the top of the racks in the SFP is 65.83°C under the normal conditions case using a calculated maximum pool inlet temperature of 36.8°C. The maximum peak temperature reached is 80.9°C under the abnormal conditions case using a calculated maximum pool inlet temperature of 37.0°C.

The results also show that the maximum peak cladding temperature that will be reached is 97.12°C.

In the event of 80% blockage at the outlet of the rack, the temperature reached in the normal conditions case would be 64.86°C. The temperature reached in the abnormal conditions case would be 93.86°C.

The maximum temperature of fluid exiting the spent fuel storage racks in the buffer pool is 66.7°C.

In the current GE design for the spent fuel pool, the cold inlet water pipe is routed to the bottom of the pool, therefore, the water that cools the fuel elements can easily enter the bottom part of the racks. This inlet pipe design allows that the introduction of cold water at the bottom part of the racks eliminates the dependency of distances between racks or between racks and pool wall.

## 5.6 REFERENCES

- 1) "Fuel Storage Rack Design Specification" Document No 26A7032 Rev 02 GE Nuclear Energy.
- 2) ANSYS CFX Computer Program Release 11.0, ANSYS Inc., South Point, 275 Technology Dr., Canonsberg, PA 15317.
- 3) ESBWR Spent Fuel Pool Decay Heat Part II GE-NE-0000-0040-6730-R0-DRAFT Rev 0. GE Proprietary Information.
- 4) ESBWR Spent Fuel Pool Boil-off. NeDRF 0000-0038-9391/neDRFSection 0000-0038-9392 Rev 02.
- 5) "Rack Layout at Spent Fuel Building" ENSA 5926.D100 Rev 01.
- 6) Design Study Summary GE14E, ESBWR Fuel Assembly, DRF Section 41-8790, Global Nuclear Fuel (GNF).
- 7) "Heat Transmission" William H. McAdams. McGraw-Hill Book Company.
- 8) "Fuel Storage Requirements" Doc. No 22A5866 Rev 08, GE Nuclear Energy.
- 9) "Rack Layout at Spent Fuel Building" ENSA 5926.D100 Rev 02.
- 10) ESBWR Buffer Pool Boil-Off and Makeup Capacity, eDRF Section 0000-0076-3483.

End of document